

Predicting collision outcomes of partially-dried droplets in spray drying

Sewalt, E.J.G.

DOI

[10.4233/uuid:8204cf4d-a5fd-4e20-956c-37aba9bf3dd7](https://doi.org/10.4233/uuid:8204cf4d-a5fd-4e20-956c-37aba9bf3dd7)

Publication date

2024

Document Version

Final published version

Citation (APA)

Sewalt, E. J. G. (2024). *Predicting collision outcomes of partially-dried droplets in spray drying*. [Dissertation (TU Delft), Delft University of Technology]. <https://doi.org/10.4233/uuid:8204cf4d-a5fd-4e20-956c-37aba9bf3dd7>

Important note

To cite this publication, please use the final published version (if applicable). Please check the document version above.

Copyright

Other than for strictly personal use, it is not permitted to download, forward or distribute the text or part of it, without the consent of the author(s) and/or copyright holder(s), unless the work is under an open content license such as Creative Commons.

Takedown policy

Please contact us and provide details if you believe this document breaches copyrights. We will remove access to the work immediately and investigate your claim.

Predicting collision outcomes of partially-dried droplets in spray drying

Dissertation

for the purpose of obtaining the degree of doctor
at Delft University of Technology.

by the authority of the Rector Magnificus Prof. dr. ir. T.H.J.J. van der Hagen,
chair of the Board for Doctorates,

to be defended publicly on
Thursday 2 May 2024 at 10:00 o'clock

by

Erik Josef Gerhardus SEWALT

Master of Science in Food Technology, Wageningen University & Research, The Netherlands

Born in Doetinchem, The Netherlands

This dissertation has been approved by the promotor.

Composition of the doctoral committee:

Rector Magnificus,	chairperson
Prof. dr. ir. J.R. van Ommen	Delft University of Technology, promotor
Dr. ir. V. van Steijn	Delft University of Technology, promotor
Dr. ir. G.M.H. Meesters	Delft University of Technology, copromotor

Independent members:

Prof. dr. ir. J.T. Padding	Delft University of Technology
Prof. dr. ir. V. Garbin	Delft University of Technology
Prof. dr. ir. J.D. Litster	The University of Sheffield, United Kingdom
Prof. dr. ir. J.A.M. Kuipers	Eindhoven University of Technology
Prof. dr. ir. C.R. Kleijn	Delft University of Technology, reserve member

The research presented in this thesis was performed within the framework of the Netherlands Organization for Scientific Research (NWO) (grant number 15459 "Multi-scale understanding and control of spray drying processes").

[Print information]

Contents

1	Introduction	1
1.1	Motivation	1
1.2	Research	2
1.3	Thesis outline	3
2	Static and dynamic stickiness tests to measure particle stickiness	7
2.1	Introduction	8
2.2	Glass transition temperature	9
2.3	Static stickiness tests	11
2.3.1	Visual observation	11
2.3.2	Shear test	12
2.3.3	Penetration test	12
2.3.4	Blow test	12
2.3.5	Comparison of tests	13
2.3.6	Application areas of static stickiness tests	13
2.4	Dynamic stickiness tests	14
2.4.1	Sticky-point test	14
2.4.2	Fluidized bed	15
2.4.3	Particle gun	16
2.4.4	Cyclone test	16
2.4.5	Optical test	16
2.4.6	Probe test	17
2.4.7	Comparison of tests	18
2.4.8	Application areas of dynamic stickiness tests	20
2.5	Conclusion	22
3	Revealing how maltodextrin-containing droplets dry using optical coherence tomography	27
3.1	Introduction	28
3.2	Materials and methods	29
3.2.1	Solution preparation	29
3.2.2	Substrate preparation	29
3.2.3	Droplet drying experiment	29
3.2.4	Optical Coherence Tomography measurements	29
3.2.5	OCT signal processing - General	30
3.2.6	OCT signal processing - Determination of the spatio-temporal diffusion coefficient of the TiO ₂ particles	31
3.2.7	Testing of the diffusion coefficient determination method	32
3.2.8	Determination of the spatio-temporal viscosity and concentration of the MD12 solution	32
3.2.9	OCT signal processing - Droplet drying kinetics and internal flow	32
3.3	Results and Discussion	33
3.3.1	Drying kinetics from 2D OCT images	33
3.3.2	Internal flow from 2D OCT images	35
3.3.3	Skin formation from 2D OCT images	35
3.3.4	Measuring the dynamic intra-droplet solute redistribution	36
3.4	Conclusion	39

4	The influence of drying on the collision outcome of partially-dried droplets and particles using maltodextrin systems	43
4.1	Introduction	44
4.2	Experimental	46
4.2.1	Materials	46
4.2.2	Droplet drying setup	46
4.2.3	Particle Ejector	47
4.2.4	Collision image processing	47
4.3	Results & Discussion	47
4.3.1	Collision outcomes	47
4.3.2	Locking point acquisition	48
4.3.3	Collision outcome in relation to the locking point	50
4.3.4	Relating collision outcomes to the intra-droplet concentration gradient	51
4.4	Conclusion	54
4.5	Appendix	55
4.5.1	Calculations.	55
4.5.2	Locking point raw data.	55
5	Experimental characterization of partially-dried droplet collisions for mapping regimes using the glass transition	59
5.1	Introduction	60
5.2	Experimental	61
5.2.1	Solution preparation	61
5.2.2	Falling particles on a stagnant partially-dried droplet - particle ejector	61
5.2.3	Falling partially-dried droplets on a stagnant particle - falling droplet column	62
5.2.4	Evaporation model	63
5.3	Results & Discussion	63
5.3.1	Experimental collisions	63
5.3.2	Comparison of experimental collisions with the surface glass transition as a predictor of collision outcome	64
5.3.3	Comparison of falling droplet column collisions with surface glass transition	69
5.4	Discussion.	70
5.5	Conclusion	71
5.6	Appendix	71
5.6.1	Numerical model for obtaining the time until glass transition at the droplet's surface	71
5.6.2	Assumptions	72
5.6.3	Numerical method	73
5.6.4	Evaporate.	74
5.6.5	Shrink.	81
5.6.6	Diffuse	84
5.6.7	Validation.	93
6	Conclusions and Outlook	99
6.1	Conclusion	99
6.2	Outlook	100
6.2.1	Fundamental analysis of the intra-droplet concentration gradient.	100
6.2.2	Exploring the universality of an alternative mapping approach to include collision dynamics	101
6.2.3	Exploring the limitations of the Péclet number	102
6.2.4	Temperature and humidity ramping for mimicking spray drying	103
6.2.5	Miniaturizing collision experiments with microfluidic approaches	103

Summary

Evaporating solute-containing droplets tend to temporarily become sticky as they transition from wet droplets to dry particles. Stickiness plays a crucial role in promoting beneficial powder properties through agglomeration but also in potential fouling of drying equipment. Spray drying, a processing technology turning a swarm of droplets into powder, is particularly susceptible to stickiness. Therefore, it is desirable to predict when a droplet becomes sticky. However, predicting the drying and collision behavior of droplets in spray drying is challenging due to multiple factors: transient drying dynamics, intra-droplet solute redistribution, morphological changes, and varying impact velocities.

This dissertation unravels the intricate behavior of partially dried droplets in spray drying scenarios. The primary goal is to understand how their collision outcomes vary with varying degrees of drying. A key aspect is developing predictive strategies for these collision outcomes, considering the distinct drying patterns and internal concentration gradients within solute-containing droplets.

Chapter 2 explores the concept of stickiness, pivotal in powder-processing industries, and reveals the challenges in predicting the stickiness of drying droplets. This exploration illustrates two key issues with predicting stickiness of droplets. The first issue is that the sticky condition is approached from the direction of the dry particle towards the wet droplet in nearly all literature studies. In spray drying, the wet droplet dries until a dry particle is obtained, approaching the sticky condition from the reverse direction and, consequently, leading to different outcomes. The second issue is that the conditions under which particles stick together due to stickiness depend on how those particles impact each other. A higher impact velocity makes particles stick together at lower viscosity, while lower impact velocity collisions show sticking at higher viscosity. Ultimately, the influence of key factors like viscosity, glass transition temperature, and impact velocity significantly affects collision outcomes.

Single droplet drying experiments have clearly shown how fast-drying droplets, such as those found in spray drying, develop sharp intra-droplet concentration gradients of solute. This phenomenon arises from two opposing driving forces. Evaporation of the droplet drives surface accumulation of solute due to the shrinking surface, while solute diffusion attempts to homogenize the accumulation to form an evenly distributed concentration. When evaporation is rapid, accumulation dominates and causes an increasingly concentrated layer of solutes at the droplet's surface. This surface accumulation results in the formation of a skin and consequently all manner of morphological deformations. The formation of the intra-droplet concentration gradient and its effect on surface properties is thus crucial to the outcome of a collision between drying droplets.

Chapter 3 presents a methodology using optical coherence tomography (OCT) to measure the spatio-temporal concentration of solute within drying droplets. Whereas most measurements of intra-droplet solute distributions in the literature have occurred post-drying, which troubles insight into the formation of the gradient during drying, the developed method enables quantifying the dynamic redistribution of solute. With OCT, we can obtain the local diffusion coefficient over a single axis in the droplet, which gives insight into the intra-droplet concentration gradient. The findings suggest that OCT has high potential to reveal internal dynamics in drying droplets and validate numerical modeling of the intra-droplet concentration gradient.

Chapter 4 and 5 show the development of two experimental setups that enable studying the collision outcomes of drying droplets over a wide range of drying drying times. The first setup is a modified sessile single droplet dryer with a particle ejection system from which particles are ejected onto the drying droplet, enabling a detailed study on the outcome of the collision and its dependence on the time the solute-containing droplet has dried. Total drying times for these droplets could be controlled from 10 to 60 s. The second setup was a falling droplet column with a continuous droplet disperser from the top, where a hot counter-current airflow induced evaporation. Openings on the side of the column allowed the introduction

of a dry collision object in the path of the drying droplets. This second setup allowed studying much shorter drying times, more comparable to industrial spray drying conditions, ranging from 0.1 to 2 s.

Chapter 4 presents the study of collisions of partially dried droplets containing the excipient maltodextrin, a family of solutes that is widely used in food research. The experiments observed with the particle ejector allowed us to compare the drying-time dependent transitions between the observed three collision outcomes (coalescence, sticking, and bouncing) with the characteristic changes in drying kinetics and droplet morphology that take place during evaporation. The drying time needed to transition between collision outcomes can range over several orders of magnitude, depending on the environmental conditions and droplet properties. In this chapter, we explored different strategies to unify the boundaries between collision outcomes. The morphological changes of a drying droplet have been studied and follow a characteristic process with easily identifiable transitions. We hypothesized these morphological transitions to be related to the transitions between collision outcomes, since they both depend on the rate of solute accumulation at the droplet's surface. In our study of collision outcomes and morphological changes, we were unable to find a sufficient relation between the two that indicated predictive potentiality. Instead, our comparison found that bouncing outcomes, expected for the (almost) dry stage of the droplets, often preceded substantial morphological changes, indicating the dominance of viscous dynamics due to intra-droplet solute concentration gradients. The shape of the intra-droplet solute concentration gradient can be described by the Péclet number, which is a dimensionless number that compares solute accumulation at the surface with the diffusive rate of the solute. With this Péclet number, we were able to define an empirical relation describing the drying time overlapping with a high probability of sticking and, hence, agglomeration, for the conditions of the particle ejector.

Chapter 5 compares the influence of drying conditions on collision outcomes by directly comparing the collision experiments between the particle ejector and falling droplet column. Since stickiness is commonly considered to be a surface phenomenon, we set out to test whether stickiness occurred at similar surface conditions for the partially dried droplets, irrespective of the drying timescale. To relate the drying time to the surface conditions, we used the time needed to reach the glass transition at the surface as a reference point. While the OCT could provide experimental insight into this gradient, it remains challenging to apply this technology to drying timescales shorter than 10 seconds. Instead, we opted to numerically simulate the formation of the intra-droplet concentration gradient to calculate the time needed for the surface to reach the glass transition temperature. Our experiments demonstrated substantial differences related to drying timescales, suggesting that surface conditions alone insufficiently explained collision outcomes for partially dried droplets. Consequently, we attribute significance to the shape of intra-droplet concentration gradients in predicting collision behavior.

Overall, this dissertation contributes significant insights into the complex collision behaviors of partially dried droplets in spray drying processes. It underscores the multifaceted nature of drying dynamics and concentration gradients within solute-containing droplets. The key contribution of this work is the finding that the stickiness of droplets, while rooted in the same principles as stickiness of powders, behaves differently due to the influence of the intra-droplet solute concentration gradients. The recommendations for future work are central to this insight and propose to continue from the predictive foundation using the Péclet number, coupled with impact velocity.

Samenvatting

Verdampende druppels met opgeloste stoffen hebben de neiging om tijdelijk plakkerig te worden terwijl ze van natte druppels naar droge deeltjes overgaan. Plakkerigheid speelt een cruciale rol bij het bevorderen van gunstige poedereigenschappen door agglomeratie, maar ook bij mogelijke vervuiling van droogapparatuur. Sproeidrogen, een procestechnologie die een zwerm druppels omzet in poeder, is bijzonder gevoelig voor plakkerigheid. Daarom is het wenselijk om te kunnen voorspellen wanneer een druppel plakkerig wordt. Echter, het voorspellen van het droog- en botsingsgedrag van druppels in een sproeidroger is uitdagend vanwege meerdere factoren: de droogdynamiek, herverdeling van opgeloste stoffen binnenin de druppels, morfologische veranderingen en variërende botsingssnelheden.

Dit proefschrift richt zich op het ontrafelen van het complexe gedrag van drognede druppels in sproeidrogen. Het primaire doel is het begrijpen van hoe de uitkomst van druppelbotsingen varieert bij verschillende gradaties van droging. Een belangrijk aspect is het ontwikkelen van voorspellende strategieën voor deze botsingsresultaten, rekening houdend met de invloed van het drogen en de interne concentratiegradiënten binnenin druppels met opgeloste stoffen.

Hoofdstuk 2 verkent het concept van plakkerigheid, die cruciaal is voor poederverwerkingsindustrieën, en onthult de uitdagingen bij het voorspellen van de plakkerigheid van drogende druppels. Deze verkenning illustreert twee belangrijke uitdagingen bij het voorspellen van de plakkerigheid van druppels. Het eerste probleem is dat in bijna alle literaire studies de plakkerige toestand vanuit het droge deeltje richting de natte druppel wordt benaderd. Bij sproeidrogen droogt de natte druppel totdat een droog deeltje wordt verkregen, waarbij de plakkerige toestand juist vanuit de omgekeerde richting wordt benaderd, wat tot verschillende resultaten leidt. De tweede uitdaging is dat de omstandigheden waaronder deeltjes aan elkaar plakken afhankelijk zijn van hoe die deeltjes elkaar raken. Een hogere botsingssnelheid zorgt ervoor dat deeltjes bij lagere viscositeiten aan elkaar plakken, terwijl bij lagere botsingssnelheden plakken bij hogere viscositeiten plaatsvindt. Uiteindelijk beïnvloeden belangrijke factoren zoals viscositeit, glasovergangstemperatuur en botsingssnelheid de botsingsresultaten aanzienlijk.

Experimenten met het drogen van enkele druppels hebben duidelijk laten zien hoe snel drogende druppels, zoals te vinden tijdens het sproeidrogen, interne concentratiegradiënten van de opgeloste stoffen ontwikkelen. Dit fenomeen ontstaat door twee tegenwerkende krachten. Verdamping van de druppel zorgt voor ophoping van opgeloste stof aan het oppervlak, terwijl diffusie van deze opgeloste stof ervoor zorgt dat de ophoping juist weer gelijkmatig wordt verdeeld over de druppel. Bij snelle verdamping domineert de ophoping en veroorzaakt het een steeds geconcentreerdere laag opgeloste stof aan het oppervlak van de druppel. Deze oppervlakte-ophoping resulteert in de vorming van een 'huid' en veroorzaakt vervolgens morfologische vervormingen. De vorming van de interne concentratiegradiënt en het effect ervan op oppervlakte-eigenschappen is daarmee van hoogst belang voor de uitkomst van een botsing tussen drogende druppels.

Hoofdstuk 3 presenteert een methodologie die gebruikmaakt van optische coherentietomografie (OCT) om de spatio-temporele concentratie van opgeloste stof binnen drogende druppels te meten. Terwijl de meeste metingen van de interne concentratiegradiënt in de literatuur na het drogen plaatsvinden, wat inzicht in de vorming van de concentratiegradiënt tijdens het drogen bemoeilijkt, maakt de nieuw ontwikkelde methode het mogelijk om de dynamische herverdeling van opgeloste stof in situ te kwantificeren. Met OCT kunnen we de lokale diffusiecoëfficiënt over één as in de druppel verkrijgen, wat inzicht geeft in de interne concentratiegradiënt. De bevindingen suggereren dat OCT veel potentie heeft om de interne dynamica in drogende druppels te bestuderen en ook om te dienen als een validatiemethode voor numerieke modellering van interne concentratiegradiënten.

Hoofdstuk 4 en 5 beschrijven de ontwikkeling van twee experimentele opstellingen die het bestuderen van botsingsresultaten van drogende druppels over een breed scala aan droogtijden mogelijk maken. De

eerste opstelling is een aangepaste druppeldroger met een deeltjesuitwerpsysteem. Hiermee konden we onderzoeken hoe de botsingsuitkomst van de droogtijd van de druppel afhing. De totale droogtijden voor druppels in deze opstelling konden van 10 tot 60 s worden geregeld. De tweede opstelling was een vallende druppelkolom waarin continu druppels van bovenaf werden gedoseerd terwijl een hete tegenstroomlucht verdamping veroorzaakte. Door een droog object in openingen aan de zijkant van de kolom te steken vonden botsingen plaats over de hoogte van de kolom. Deze tweede opstelling maakte het mogelijk om veel kortere droogtijden te bestuderen die vergelijkbaar waren met sproeidroogcondities. Deze droogtijden varieerden van 0.1 tot 2 s.

Hoofdstuk 4 presenteert het onderzoek naar botsingen van gedeeltelijk gedroogde druppels met gebruik van maltodextrine, een familie van hulpstoffen die veel wordt gebruikt in voedselonderzoek. De experimenten met de deeltjesuitwerper stelden ons in staat om de droogtijd-afhankelijke overgangen tussen de waargenomen drie botsingsresultaten (coalescentie, plakken en stuiteren) te vergelijken met de karakteristieke veranderingen in droogkinetica en druppelmorfologie die plaatsvinden tijdens verdamping. De droogtijd die nodig is om de verschillende botsingsuitkomsten te doorlopen varieert over meerdere orde-groottes, wat afhangt van de eigenschappen van de omgeving en de druppel. In dit hoofdstuk hebben we verschillende strategieën onderzocht om de grenzen tussen botsingsresultaten te verenigen. Omdat de morfologische veranderingen van een drogende druppel een karakteristiek proces met eenvoudig identificeerbare overgangen ondergaan, vermoedden we dat deze morfologische overgangen gerelateerd waren aan de overgangen tussen botsingsuitkomsten. Ze zijn immers allebei afhankelijk van de snelheid waarmee de opgeloste stof zich ophoopt aan het oppervlak van de druppel. In onze studie naar botsingsresultaten en morfologische veranderingen hebben we onvoldoende een relatie tussen beide kunnen vinden die wijst op voldoende voorspellend potentieel. In plaats daarvan ontdekten we dat de uitkomst stuiteren, die we verwachtten voor het droogste stadium van de druppel, vaak voorafgaat aan het verwachte vergrendelpunt, wat wijst op de dominantie van viskeuze dynamica als gevolg van interne concentratiegradiënten in opgeloste stoffen. Deze interne concentratiegradiënt kan worden beschreven met het Péclet getal, een dimensieloos getal dat de ophoping van opgeloste stof aan het oppervlak vergelijkt met de diffusiesnelheid van deze stof. Met dit Pécletgetal waren we in staat, voor de omstandigheden van de deeltjesuitwerper, een empirische relatie te definiëren voor de droogtijd die overeenkomt met een hoge waarschijnlijkheid van plakken en daarmee agglomeratie.

Hoofdstuk 5 vergelijkt de invloed van droogcondities op de botsingsresultaten door rechtstreeks de botsingsexperimenten tussen de deeltjesuitwerper en de vallende druppelkolom te vergelijken. Aangezien plakkerigheid doorgaans wordt beschouwd als een oppervlaktefenomeen, gingen we na of plakkerigheid optrad onder vergelijkbare oppervlakteomstandigheden, ongeacht de tijdschaal van het drogen. Om de droogtijd te relateren aan de oppervlakteomstandigheden, namen we de tijd die nodig was om de glasovergang aan het druppeloppervlak te bereiken als referentiepunt. Hoewel de OCT experimenteel inzicht kon bieden in deze gradiënt, blijft het uitdagend om deze technologie toe te passen op droogtijden korter dan 10 s. In plaats daarvan kozen we ervoor om numeriek de vorming van de interne concentratiegradiënten te simuleren. Onze experimenten toonden aanzienlijke verschillen bij het vergelijken van de oppervlaktecondities over de verschillende droogtijden, wat suggereerde dat de oppervlaktecondities alleen onvoldoende de botsingsresultaten verklaarden. Hieruit volgt onze conclusie dat de interne concentratiegradiënt en niet alleen de oppervlakconditie het botsingsgedrag bepaalt.

Al met al levert dit proefschrift aanzienlijke inzichten op in hoe het drogen van druppels met opgeloste stof invloed uitoefent op de uitkomst van botsingen voor het sproeidroogproces. Het benadrukt de veelzijdige aard van de droogdynamica en concentratiegradiënten binnen druppels met opgeloste stof. De belangrijkste bijdrage van dit werk is de bevinding dat de plakkerigheid van druppels, hoewel geworteld in dezelfde principes als de plakkerigheid van poeders, zich anders gedraagt door de invloed van de interne concentratiegradiënt van de opgeloste stoffen. De aanbevelingen voor toekomstig werk bouwen voort op dit inzicht en met name de voorspellende basis die met behulp van het Péclet-getal in combinatie met de impactsnelheid is gelegd.

Introduction

1.1. Motivation

Powder agglomeration is a common phenomenon in powder technology and is particularly relevant to spray-drying, whereby droplets of a liquid are dispersed into a gaseous environment in which they quickly solidify, forming agglomerates through collisions. This process is used to produce dry powders with agglomerates of various sizes and shapes, with applications in many industries, including the food, pharmaceutical, and chemical industries. One of the main challenges with powder production is to achieve a desired level of powder uniformity in terms of size and shape, on which the formation of agglomerates has a substantial impact. This thesis explores how the evaporation of droplets in spray drying affects the collision behavior and agglomeration of partially-dried droplets.

The spray-drying process begins with the introduction of a liquid containing dissolved solids into a spray-drying chamber. The liquid is then atomized into small droplets, which are exposed to hot air, causing the liquid to rapidly evaporate. As the droplets evaporate, the dissolved solids in the liquid may form a solid shell, forming particles of a desired size and shape. Once the particles are formed, they collect at the bottom of the chamber. Subsequently, the particles go through a cyclone collector to separate dust from the powder. This can lead to a variety of particle morphologies with descriptive names such as "blistered", "hollow", "exploded" or "buckled" (Sadek et al., 2015). Several illustrative examples of particle morphology for spray dried skim milk and whole milk, which are common in spray drying, are shown in Figure 1.1. Note the structural differences such as the degree of porosity, presence of internal vacuoles and varying thickness of the shell.

Figure 1.1 also shows particles that have clustered together to form an agglomerate. The formation of agglomerates can have a substantial impact on the final powder product, affecting flowability and solubility characteristics (Rumpf, 1962; Santos et al., 2018; Schutyser et al., 2019). Agglomeration is a result of droplet collisions where the particles end up sticking together.

Due to the high velocities and turbulent motion of the droplets, droplet collisions are a common phenomenon in spray drying. Droplets can collide with each other or the wall of the drying chamber, but often collisions are induced through targeting the in-going streams of droplets and particles at each other. When a droplet collides another droplet, they can either coalesce, forming a larger droplet, they can stick together to form an agglomerate, or they can bounce away from each other. Examples of these collision outcomes are shown in Figure 1.2. This figure shows coalescence, sticking and bouncing for a particle impacting on a single partially-dried droplet. To control the size and shape of the agglomerates, it is important to control both the collision properties and the properties of the colliding droplets, which is strongly dependent on the degree of drying.

Computational Fluid Dynamics (CFD) is a simulation tool with a wide range of applications, including simulating processes, in the food processing sector. It is often used for simulating spray drying processes

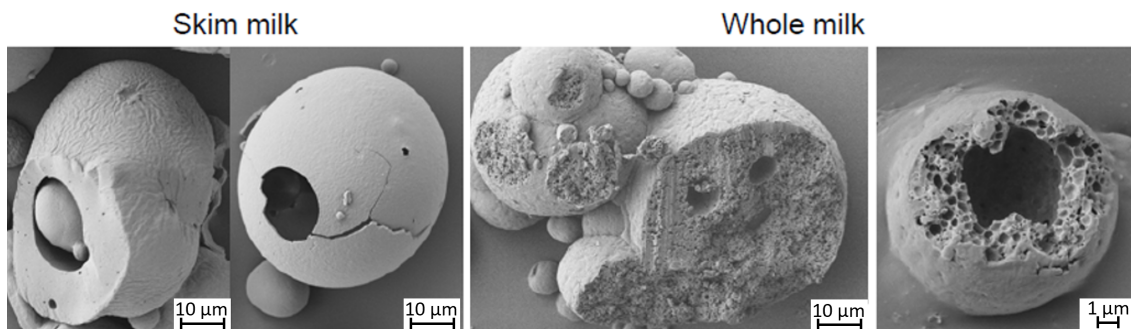


Figure 1.1: SEM images of spray dried skim milk and whole milk. Internal vacuoles, agglomerated particles and varying thickness of particle walls are clearly visible. Pictures courtesy of TetraPak (Sweden).

due to the challenge of measuring air flow, temperature, humidity and particle size distributions in large-scale spray drying (Kuriakose & Anandharamakrishnan, 2010).

CFD models enable engineers to simulate the behavior of the fluid and particles in the drying chamber, providing insight into the flow patterns, particle size distributions, and residence times of the droplets and particles. This information can be used to optimize the design of the spray dryer, improving its performance and efficiency.

Despite its advantages, CFD has several limitations when applied to the spray drying process. CFD models are limited in their ability to accurately predict the collision behavior of the partially dried droplets in the drying chamber and need another approach of resolving collision outcomes (Verdurmen et al., 2006; Verdurmen et al., 2004). It has remained challenging to sufficiently understand the mechanisms behind partially-dried droplet collisions to accurately resolve droplet collisions for simulation purposes.

1.2. Research

The main subject of this thesis is the collision behavior of partially-dried solute-containing droplets in spray drying scenarios. The objective is to develop a predictive approach for resolving collision outcomes of partially-dried solute-containing droplets. Predicting collision outcomes requires both an investigation into how collision parameters affect the collision outcome and into how the partially-dried droplet's properties affect the collision outcome. This, in turn, requires furthering the understanding of how the morphology and stickiness of solute-containing droplets develops during drying. The drying of solute-containing droplets is challenging on its own because partially-dried droplet properties are not homogeneous. The rate of drying is typically so rapid that the solute accumulates near the liquid-gas interface (Vehring et al., 2007). This accumulation results in the formation of a skin layer at the droplet surface, which, depending on the physico-chemical properties of the components, can undergo a sol-gel transition and become akin to a viscoelastic membrane (Bansal et al., 2015; Bansal et al., 2018). Exploring the influence of non-homogeneous drying on partially-dried droplet properties will be fundamental to developing predictive relations.

Due to the many facets of this problem, this project was part of a consortium that addresses the need of developing a better understanding of the drying kinetics and agglomeration behavior in spray drying processes. The aim is to come to a multi-scale understanding of these processes and model them for the implementation into a CFD spray drying model. The implementation into a CFD model is, however, not part of this consortium. For this purpose, three academic groups in collaboration with four industrial partners, DSM, Nutricia Research, Tetrapak and General Electric, have integrated their efforts. The academic efforts are undertaken by:

- Isabel Siemons (Wageningen, Food Process Engineering), under supervision of Maarten Schutyser and Ruud van der Sman, experimentally studied drying of small sessile single droplets to understand the physical and thermodynamic changes and how these influence morphological development, which specific focus on the rheological changes in the droplet. This information aided the interpretation

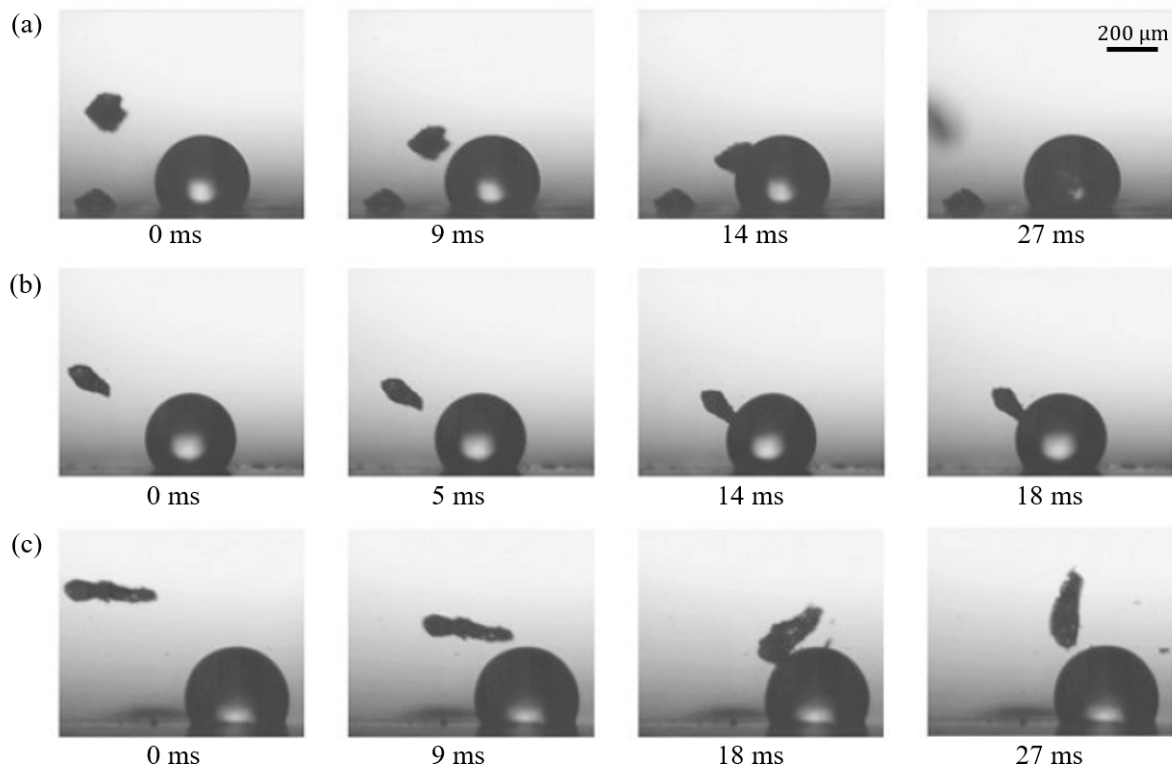


Figure 1.2: Image series of typical collision outcomes in spray drying. a) Minimal drying - Coalescence, b) Medium amount of drying - sticking (agglomeration) and c) Almost fully-dried - bouncing. Collision are between maltodextrin particles and partially-dried droplets of maltodextrin solution.

of agglomeration results by Erik Sewalt and serves as input for the model developed by Stephan Sneijders.

- Erik Sewalt (Delft, Product & Process Engineering), under supervision of Volkert van Steijn, Gabriele Meesters and Ruud van Ommen, experimentally studied how the extent of drying influences the agglomeration probability and particle stickiness. A free-falling dryer and a sessile dryer are used to study droplet-particle collisions. Studying collisions of partially-dried droplets provides sticking probabilities, which can validate the model developed by Stephan Sneijders.
- Stephan Sneijders (Delft, Process & Energy), under supervision of Johan Padding, developed a numerical model that predicts collision outcomes of partially-dried droplets. This model integrates generated knowledge from the other groups. The model is validated by single droplet drying experiments by Isabel Siemons and Erik Sewalt and sticking probabilities from droplet collisions by Erik Sewalt. Finally, the aim is to implement this model into a full-scale spray drying model.

1.3. Thesis outline

This thesis is an experimental study of how drying influences agglomeration probability and particle stickiness. This is studied by trying to understand how sticking probabilities depend on the dynamics of droplet drying and subsequent collisions between partially dried droplets. In the chapters described below, various aspects of the study are highlighted.

Chapter 2 addresses the concept of stickiness, a phenomenon of merging two contacting surfaces due to adhesive or cohesive forces. It highlights the glass transition temperature T_g , which is a key concept to understand stickiness. It also delves into the various methods used to measure the stickiness of dry or wet material, beginning with static measurement methods and then dynamic measuring methods. It is emphasized that stickiness is dependent on the viscosity and contact time of the surfaces, both of which

are essential for the understanding of agglomeration. This chapter illustrates the important role played by the impact velocity of droplet collisions on the outcome of the collisions.

Chapter 3 examines how evaporation of solute-containing droplets affects the internal concentration gradients of the solute. To measure the intra-droplet concentration gradient, a novel application of optical coherence tomography was used. Optical coherence tomography is an imaging technique which uses light to produce high-resolution, three-dimensional images of internal structures. It works by measuring the interference of light of different wavelengths which have been reflected from within the sample. The novel method involved scanning the droplet in situ, rather than post situ, and it is the first time that it has been used to measure the concentration gradient of a maltodextrin droplet. The optical coherence tomography method allowed for the visualization of skin formation in the drying droplet, as it evaporates at room temperature, until structural deformation occurs. The ability to measure the concentration gradient in situ provides researchers with experimental data for validating numerical evaporation models that model the internal concentration gradient.

Chapter 4 addresses the question of how solute concentrations gradients affect the collision outcome of partially-dried droplets and how the collision parameters (i.e. kinetic energy, impact angle, etc.) influence the collision outcome of partially-dried droplets. It discusses the effect of partial-drying on the collision outcomes in relation to the typical drying curve of a drying droplet. A solute-containing droplet has a specific drying pattern with three characteristic regimes. The first regime is one of external mass transfer limitation for the evaporation, in which the evaporation rate, expressed in m^2s^{-1} , remains constant. The second regime begins when the mass transfer limitation for evaporation transitions to an internal limitation due to the accumulation of solute at the interface, which reduces the transfer rate of water through this concentrating surface layer. Finally, a third regime can be identified when the surface layer reaches a critical 'locking' point, where the droplet shape starts to deviate from the spherical shape. To understand the different collision outcomes, collisions of maltodextrin particles with partially-dried droplets of maltodextrin solutions have been studied. This chapter aims to identify if the transition between different collision outcomes are related to the critical moments in the typical drying curve of a drying droplet.

Chapter 5 addresses the question of how the collision outcome of partially-dried droplets compare for droplets drying at different timescales, such as $< 1\text{ s}$ for industrially sized droplets ($10\ \mu\text{m}$ to $100\ \mu\text{m}$) (Adhikari et al., 2003; Wu et al., 2007) and around a minute for droplet sizes commonly used in single droplet studies ($200\ \mu\text{m}$ to $2000\ \mu\text{m}$) (Fu et al., 2012). It describes the comparison of how collision outcomes change when the timescales of drying change by order of magnitudes. In this chapter, the comparison is made between two drying setups, a free-falling dryer where droplets dry in the order of 1 s and the sessile droplet dryer introduced in Chapter 4, where droplets dry in the order of 10 s to 100 s . A numerical model for predicting the intra-droplet concentration gradient was used to compare the collision outcomes of droplets drying at different timescales with a critical surface concentration, chosen to be T_g . Droplets drying in the free-falling dryer at short timescales needed to reach much greater ratio of drying time compared to the critical drying time compared to the droplets drying at longer timescales, indicating that the difference in timescale did have an effect on the collision outcome. This results indicate that a droplet's surface properties alone are not sufficient to predict droplet collision outcome with a high degree of accuracy.

Bibliography

- Adhikari, B., Howes, T., Bhandari, B. R., & Troung, V. (2003). Surface stickiness of drops of carbohydrate and organic acid solutions during convective drying: Experiments and modeling. *Drying Technology*, *21*(5), 839–873. <https://doi.org/10.1081/drt-120021689>
- Bansal, L., Miglani, A., & Basu, S. (2015). Universal buckling kinetics in drying nanoparticle-laden droplets on a hydrophobic substrate. *Physical Review E*, *92*(4), 042304. <https://doi.org/10.1103/physreve.92.042304>
- Bansal, L., Sanyal, A., Kabi, P., Pathak, B., & Basu, S. (2018). Engineering interfacial processes at mini-micro-nano scales using sessile droplet architecture. *Langmuir*, *34*(29), 8423–8442. <https://doi.org/10.1021/acs.langmuir.7b04295>

- Fu, N., Woo, M. W., & Chen, X. D. (2012). Single droplet drying technique to study drying kinetics measurement and particle functionality: A review. *Drying Technology*, *30*(15), 1771–1785. <https://doi.org/10.1080/07373937.2012.708002>
- Kuriakose, R., & Anandharamakrishnan, C. (2010). Computational fluid dynamics (cfd) applications in spray drying of food products. *Trends in Food Science & Technology*, *21*(8), 383–398. <https://doi.org/10.1016/j.tifs.2010.04.009>
- Rumpf, H. (1962). The strength of granules and agglomerates, In *Agglomeration-proceedings of the first international symposium on agglomeration*, Philadelphia.
- Sadek, C., Schuck, P., Fallourd, Y., Pradeau, N., Le Floch-Fouéré, C., & Jeantet, R. (2015). Drying of a single droplet to investigate processstructurefunction relationships: a review. *Dairy Science and Technology*, *95*(6), 771–794.
- Santos, D., Mauricio, A. C., Sencadas, V., Santos, J. D., Fernandes, M. H., & Gomes, P. S. (2018). Spray drying: An overview. *Pignatello, R.(Comp.). Biomaterials-Physics and Chemistry-New Edition. InTech. UK*, 9–35. <https://doi.org/10.5772/intechopen.72247>
- Schutysen, M. A. I., Both, E. M., Siemons, I., Vaessen, E. M. J., & Zhang, L. (2019). Gaining insight on spray drying behavior of foods via single droplet drying analyses. *Drying Technology*, *37*(5), 525–534.
- Vehring, R., Foss, W. R., & Lechuga-Ballesteros, D. (2007). Particle formation in spray drying. *Journal of Aerosol Science*, *38*(7), 728–746. <https://doi.org/10.1016/j.jaerosci.2007.04.005>
- Verdurmen, R. E. M., Houwelingen, G. v., Gunging, M., Verschueren, M., & Straatsma, J. (2006). Agglomeration in spray drying installations (the edecad project): Stickiness measurements and simulation results. *Drying Technology*, *24*(6), 721–726. <https://doi.org/10.1080/07373930600684973>
- Verdurmen, R. E. M., Menn, P., Ritzert, J., Blei, S., Nhumaio, G. C. S., Sonne Sørensen, T., Gunging, M., Straatsma, J., Verschueren, M., Sibeijn, M., et al. (2004). Simulation of agglomeration in spray drying installations: The edecad project. *Drying technology*, *22*(6), 1403–1461. <https://doi.org/10.1081/drt-120038735>
- Wu, W. D., Patel, K. C., Rogers, S., & Chen, X. D. (2007). Monodisperse droplet generators as potential atomizers for spray drying technology. *Drying Technology*, *25*(12), 1907–1916. <https://doi.org/10.1080/07373930701727176>

2

Static and dynamic stickiness tests to measure particle stickiness

Sticking of particles has a tremendous impact on powder-processing industries, especially for hygroscopic amorphous powders. A wide variety of experimental methods has been developed to measure stickiness. These methods generally aim to identify at what combinations of temperature and moisture content material becomes sticky. This review describes, for each method, how so-called stickiness curves are determined. As particle velocity also plays a key role, we classify the methods into static- and dynamic stickiness tests. Static stickiness tests have limited particle motion during the conditioning step prior to the measurement. Thus, the obtained information is particularly useful in predicting the long-term behavior of powder during storage or in packaging. Dynamic stickiness tests involve significant particle motion during conditioning and measurement. Stickiness curves strongly depend on particle velocity, and the obtained information is highly relevant to the design and operation of powder production and processing equipment. Virtually all methods determine the onset of stickiness using powder as a starting point. Given the many industrial processes like spray drying that start from a liquid that may become sticky upon drying, future effort should focus on developing test methods that determine the onset of stickiness using a liquid droplet as a starting point.

Published as: Erik J.G. Sewalt, Fuweng Zhang, Volkert van Steijn, J. Ruud van Ommen, Gabrie M.H. Meesters (2020). Static and dynamic stickiness tests to measure particle stickiness. *KONA Powder and Particle Journal*, 2021017. <https://doi.org/10.14356/kona.2021017>

2.1. Introduction

Sticking of particles has a tremendous impact on numerous industries that process powders. Sticking can cause several issues, such as fouling and blockage of equipment, or caking of stored powder. It can also be used advantageously to produce agglomerates with beneficial properties. Why, how, and when particles stick together are critically important questions. In this review, we focus on the ‘when’ question by reviewing the experimental methods commonly used to determine the conditions under which sticking occurs. We hereby focus on the stickiness of hygroscopic amorphous powders, which play a major role in the food industry (Boonyai et al., 2004). Crystalline materials, which may also stick, but through a different mechanism (Kamyabi et al., 2017), are beyond this review’s scope.

Whether two particles stick depends on their material and a wide variety of parameters, including their temperature, and moisture content. A common way to characterize the stickiness of a material is to map the stickiness based on the environmental temperature and the moisture content. The moisture content can be described in terms of the particle’s water mass fraction (x_w), or the equilibrium environmental relative humidity (RH). The part of the parameter space for which the material is sticky is called the sticky region, which is bounded by the so-called sticky-point curve, $T_1(x_w)$, and the so-called tack boundary, $T_2(x_w)$, as illustrated in Table 2.1. Besides the environmental parameters, this map also illustrates the particle’s material properties in the form of a boundary between the glassy state and the rubbery state, known as the glass transition temperature, $T_g(x_w)$. The rubbery state has some overlap with the sticky region, and with further hydration becomes the liquid state (Roos, 2002). While particles are non-sticky in the glassy state, material properties, especially viscosity, drastically change upon transitioning to the rubbery state. Hence, the curves represented by the differences $T_1(x_w) - T_g(x_w)$ and $T_2(x_w) - T_g(x_w)$ are two meaningful measurements of the sticky-region that include the influence of temperature, moisture content, as well as the material. The distance between the sticky-point curve $T_1(x_w)$ and the glass transition curve $T_g(x_w)$ often slightly depends on x_w (Palzer, 2005). Therefore, the onset of stickiness is commonly reported as a constant critical deviation from $T_g(x_w)$, denoted as $(T - T_g)_c$.

Experimental stickiness tests generally aim to determine the sticky-point curve or the tack boundary by measuring stickiness for different temperatures and moisture contents. While most methods approach the sticky region from the glassy state to find $T_1(x_w) - T_g(x_w)$, a limited number of methods approach the sticky region from the liquid state to find $T_2(x_w) - T_g(x_w)$. Although the tack boundary is less well understood, it is known that the change in behavior is less sharp than near the sticky-point curve (Kudra, 2003). While the direct observable may differ between the experimental methods, what all methods have in common is that they follow two steps: (1) a conditioning step, where the material is subjected to a specified temperature T and humidity RH for a certain time window and (2) a measurement step where the stickiness of the powder is measured (Boonyai et al., 2004). Whereas these steps are separated for some methods, they are intertwined for others. Hence, not only the duration of conditioning influences the sticky region’s boundaries but also the used measurement method. While the influence of conditioning time is well understood (Kamyabi et al., 2017), the influence of particle motion in the conditioning and/or measurement step on the boundaries of the sticky region is still unclear. For skim milk powder, one of the most abundantly tested materials, a wide range for $T_1(x_w) - T_g(x_w)$ has been reported. For particles that are static during the conditioning step, values as small as 8 °C were reported for $T_1 - T_g$ (Verdurmen et al., 2006). By contrast, values as high as $T_1 - T_g = 63$ °C were reported for particles moving at tens of meters per second (Walmsley et al., 2014).

Following Verdurmen et al. (2006), we therefore distinguish between two classes of methods in this review. The first class is where the particles can be considered static during conditioning (not set in continuous motion through external means). The second class is where the particles are moving during conditioning. We refer to the first class of methods as *static stickiness tests* and to the second class as *dynamic stickiness tests*.

This review aims to provide an overview of the available methods to measure stickiness. As static stickiness tests, we describe various visual observation tests, the shear test, the penetration test, and the blow test. As dynamic stickiness tests, we describe the sticky-point test, the fluidized bed test, the particle gun, the cyclone test, the optical test, and the probe test. For each method we describe how it can be

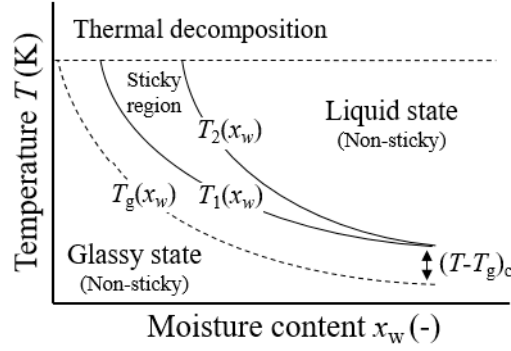


Figure 2.1: Map of temperature and moisture content showing the region in which a material is considered sticky. This region is enveloped by the sticky-point curve ($T_1(x_w)$), the tack boundary ($T_2(x_w)$), and the temperature above which the material decomposes. The sticky-point curve and tack boundary are often reported with respect to the glass transition temperature of the material (dashed line), which separates its glassy state from its liquid state. The difference $T_1(x_w) - T_g(x_w)$ is in literature more commonly referred to as $(T - T_g)_c$. Figure is modified from Lockemann (1999) and Kudra (2003).

used to determine either the sticky-point curve $T_1(x_w)$ or the tack boundary $T_2(x_w)$ of the sticky region. Additionally, we describe what we view to be the method's best application in industry. The overview of methods shows that particle velocity plays a significant role in the measured boundaries of the sticky region, illustrating the importance of choosing the most appropriate method for the application in mind.

2.2. Glass transition temperature

The glass transition temperature T_g marks the temperature where an amorphous material transitions from a glassy state to a rubbery state upon increasing temperature. While both states are fundamentally a liquid, the behavior of the glassy state is solid-like, being hard and brittle, and the rubbery state behaves like a highly-viscous liquid. The nature of the glass transition is the molecular freedom of movement, which is restricted in the glassy state (Roos, 2002).

The most common method to experimentally determine T_g is using differential scanning calorimetry (DSC), although several other methods are available (Li et al., 2019). In DSC, the T_g is found by subjecting the material in the glassy state to a temperature ramp and measuring the specific heat capacity. The specific heat capacity shows a characteristic change during the glass transition (Hogan et al., 2010; Roos, 2010). By repeating the experiment at different x_w , the curve for $T_g(x_w)$ shown in Table 2.1 can be experimentally constructed. Similarly, dynamic vapor sorption (DVS) can be used to measure the vapor sorption characteristics by applying a ramp in relative humidity at a fixed T while measuring the sample's mass. In the glassy state, water sorption only occurs at the surface, while the rubbery state also allows for bulk sorption, such that a characteristic change in the water sorption rate is observed at T_g (Burnett et al., 2004).

The glass transition temperature can also be estimated theoretically, for example using the Gordon-Taylor or Couchman-Karasz equation. The Gordon-Taylor equation can be used to determine the influence of water on the glass transition temperature $T_g(x_w)$ of a dry powder, based on the glass transition temperature of the anhydrous powder ($T_{g,s}$) and pure water ($T_{g,w}$), and the weight fraction of moisture, x_w , as

$$T_g = \frac{(1 - x_w)T_{g,s} + kx_wT_{g,w}}{(1 - x_w) + kx_w} \quad (2.1)$$

with $T_{g,w} = -135^\circ\text{C}$ (Roos, 2002). The constant k is often calculated from the densities ρ , $T_{g,s}$, and $T_{g,w}$ as $k = (\rho_s T_{g,s}) / (\rho_w T_{w,s})$ (Katkov & Levine, 2004; Simha & Boyer, 1962). The Couchman-Karasz equation, while similar to Equation (2.1), is based on thermodynamic additivity of specific heat capacity. Although different versions are reported, the so-called 'modified' version is found when using $k = \Delta C_{p,w} / \Delta C_{p,s}$ in Equation (2.1). The changes in heat capacity ΔC_p at T_g can be found using DSC

(Sochava, 1997). For $\Delta C_{p,w}$, $1.94 \text{ J K}^{-1} \text{ g}^{-1}$ is often used (Katkov & Levine, 2004; Roos, 2002). Katkov and Levine 2004 showed that the modified version of the Couchman-Karas equation overestimated the T_g of mixtures and underestimated the plasticizing effect of water while they obtained a better fit using the so-called 'original' Couchman-Karas equation

$$\ln(T_g) = \frac{(1 - x_w) \ln(T_{g,s}) + kx_w \ln(T_{g,w})}{(1 - x_w) + kx_w} \quad (2.2)$$

While the Gordon-Taylor and Couchman-Karas equations are suitable for most simple systems and can be used to construct the curve for $T_g(x_w)$ in Table 2.1, they should be used with caution when considering complex mixtures (Katkov & Levine, 2004).

The glass transition temperature serves as a natural reference in the stickiness map and allows one to compare the stickiness of different type of materials. Similarly, the T_g serves as a reference in an attempt to come to a universal predictive equation of the dynamic viscosity in the rubbery state. The Williams-Landel-Ferry (WLF) equation relates the viscosity of a material to the distance from the T_g -curve ($T - T_g$) as

$$\log_{10} \frac{\eta}{\eta_g} = \frac{C_1(T - T_g)}{C_2 + (T - T_g)} \quad (2.3)$$

with C_1 and C_2 two constants and η_g the viscosity at the glass transition temperature. While the WLF equation is often considered to be valid for temperatures up to $T_g + 100 \text{ }^\circ\text{C}$ (Lomellini, 1992; Williams et al., 1955), it is only valid if correct values for the constants and η_g are chosen. Values of η_g are typically in a range between 10^{11} Pa s to 10^{14} Pa s (Downton et al., 1982; Katkov & Levine, 2004; Murti et al., 2010; Palzer, 2005; Paterson et al., 2015; Wallack & King, 1988). Recently, the glass viscosity of freeze dried amorphous lactose was measured to be $1.1 \times 10^{14} \text{ Pa s}$, although the authors suggest that further confirmation is required (Paterson et al., 2015). The wide variety of reported constants suggests that there is no universal set valid for different types of materials and different temperatures. Nevertheless, $(C_1, C_2) = (-17.44, 51.6 \text{ K})$ as originally reported by Williams et al. (1955), are often considered to be universal (Aguilera et al., 1993; Murti et al., 2010; Palzer, 2005; Schulnies & Kleinschmidt, 2018; Wallack & King, 1988). Peleg (1992) found that these constants give large deviations when $T - T_g > 20 \text{ }^\circ\text{C}$, and suggested $(C_1, C_2) = (-10.5, 85.6 \text{ K})$, which better matched the experimental trend for the η_g of amorphous lactose measured by Paterson et al. (2015). However, $(C_1, C_2) = (-8.86, 101.6 \text{ K})$ also provided a good fit to other experimental data (Dagdug & Garca-Coln, 1998; Ferry, 1980). Others use material-specific constants, such as $(C_1, C_2) = (-14.5, 36.4 \text{ K})$, which were fitted for skim milk powder (Walmsley et al., 2014). Since the WLF equation is exponential, care should be taken in the choice of the constants when using the WLF equation to predict the dynamic viscosity. To illustrate the importance of this choice for a prototypical case ($T - T_g = 20 \text{ }^\circ\text{C}$ and $\eta_g = 10^{12} \text{ Pa s}$), the constants by Williams et al. (1955) give $\eta = 1.3 \times 10^7 \text{ Pa s}$, while the constants by Peleg (1992) give $\eta = 1.0 \times 10^{10} \text{ Pa s}$ - a difference of three orders of magnitude. As there are currently no clear rules of thumb on the selection of constants, we suggest that best practice would be to fit C_1 and C_2 to experimentally measured viscosity data.

The direct relation between viscosity and $T - T_g$ through the WLF equation leads to the natural question whether viscosity can be used as a predictor for stickiness. The success of viscosity as a predictor is expected to depend on the dominant mechanism of adhesion. For hygroscopic amorphous powders close to T_g , sticking is expected to occur primarily through immobile liquid bridging or viscoelastic deformation (Palzer, 2005). In case immobile liquid bridging primarily causes sticking, we generally expect viscosity to be more meaningful than when viscoelastic deformation primarily causes sticking. More specifically, using sintering theory by Frenkel (1945) and classic viscoelastic contact models, Palzer (2005) could predict the critical $T - T_g$ needed for sticking. However, this model did not successfully predict sticking of high velocity particle gun experiments (Murti et al., 2010). A contact model for adhesive elastic particles showed better results when predicting the critical $T - T_g$ for high velocity collisions (Walmsley et al., 2014). The mentioned works strongly suggest that viscoelasticity should be accounted for when predicting $(T - T_g)_c$ for collisions of particles in motion, and that the observed $(T - T_g)_c$ is a result of the colliding material's rheological behavior and the collisions kinetics.

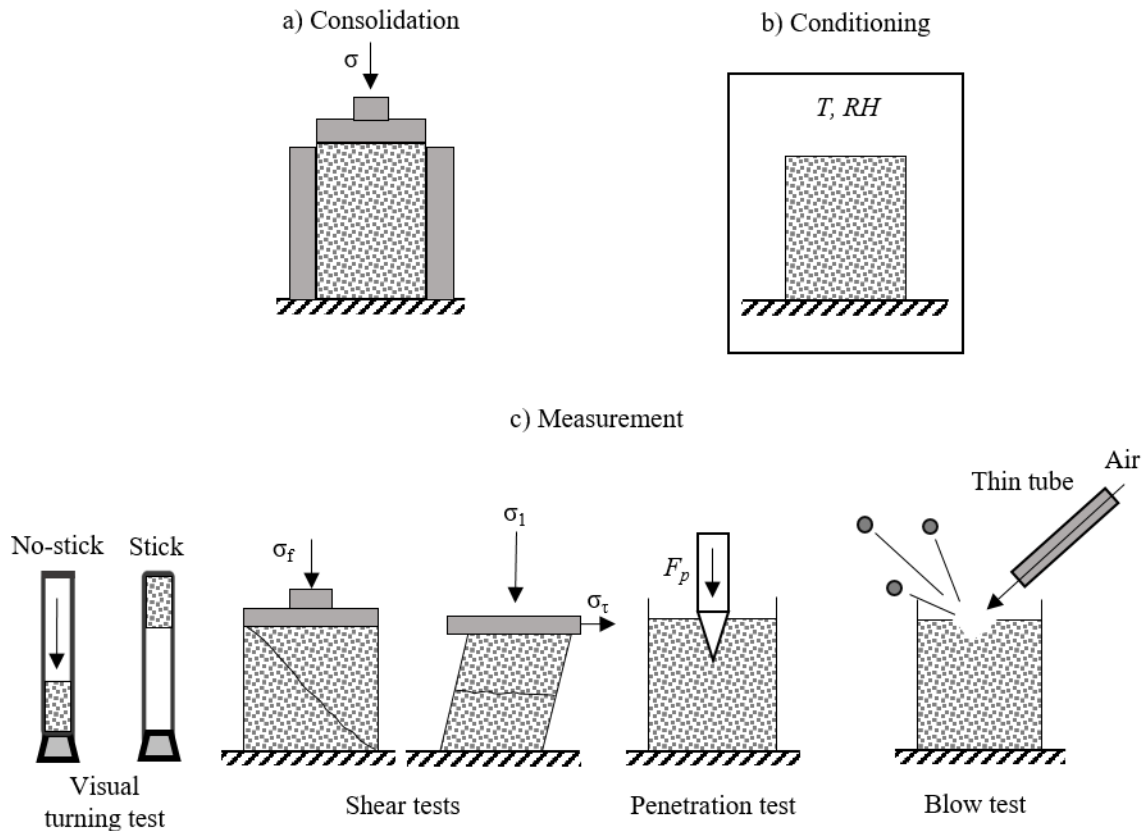


Figure 2.2: An overview of the static stickiness tests. a) In the consolidation step, the powder is compressed under a stress σ . b) In the conditioning step, the powder is subjected to temperature T and relative humidity RH for a specified duration. c) The measurement of stickiness proceeds differently per test.

2.3. Static stickiness tests

Testing stickiness of powders using static stickiness tests follows a general protocol. First, a powder bed is compressed under a stress σ to cause a certain amount of consolidation (Figure 2.2a). Second, the powder is conditioned by exposing it to an environment of controlled temperature and relative humidity Figure 2.2b. The duration of this conditioning step can be adjusted. When sufficiently long, the powder's moisture content is in thermodynamic equilibrium with the moisture in the environment such that x_w and RH are related through a vapor sorption isotherm. Third, a measurement is performed on the conditioned powder Figure 2.2c. Prior to the measurement, the powder can be considered static with little movement of the particles. Therefore, we refer to this class of tests as static stickiness tests, which are deliberately different from the dynamic stickiness tests in which the particles are actively set in continuous motion during the conditioning and measurement step. Next, we describe the different static stickiness tests.

2.3.1. Visual observation

The most straightforward form of analysis is through visual observation. Typically, a sample with a specified dry matter content is placed in a closed container. After conditioning it at a given temperature, the container is turned upside down to see whether any particles are stuck to the bottom. This procedure is repeated at different temperatures until particles noticeably stick to the bottom, which is identified as the sticky-point temperature (Palzer, 2005). By repeating this procedure for different moisture contents, the sticky-point curve $T_1(x_w)$ in Figure 2.1 can be constructed. An alternative visual observation test is one in which the powder's temperature is increased stepwise while observing changes in the appearance of the powder bed (Tsourouflis et al., 1976; Verdurmen et al., 2006).

2.3.2. Shear test

Shear tests are used to characterize powder stickiness by measuring the powder's response to shear stress. Two common approaches are uniaxial compression and shearing in shear cells. The uniaxial compression approach consolidates a powder bed with normal stress σ and then compresses along one axis until failure. The failure stress σ_f for different values of σ gives a yield locus that can be used to find the unconfined yield strength σ_c by drawing a Mohr circle starting at $\sigma = 0$ Pa (Schulze, 2008). The unconfined yield strength σ_c is used as the parameter for bed strength and can be determined for different environmental T and RH (Fitzpatrick, Hodnett, et al., 2007; Hartmann & Palzer, 2011). In order to find a sticky-point curve $T_1(x_w)$, a critical bed strength, which is characteristic for a sticky powder, must be determined first. It can be empirically determined before testing using the same or comparable materials (Palzer & Zürcher, 2004).

Similarly to uniaxial compression, shear cells can be used to determine σ_c and acquire $T_1(x_w)$ by defining a critical σ_c for the bed strength of a sticky powder (Hartmann & Palzer, 2011; Schulnies & Kleinschmidt, 2018). However, shear cells improve on result consistency by preshearing before measuring the failure stress. Preshearing to steady-state at normal stress σ_1 eliminates any stress history, for example, due to filling (Schulnies & Kleinschmidt, 2018). After preshearing, the shear stress is reversed to reduce the shear stress to zero. Subsequently, the sample is sheared to failure while measuring shear stress σ_τ under normal stress σ_2 so that $\sigma_1 < \sigma_2$ (overconsolidation), which ensures a peak is observed for the failure stress (Schulze, 2008). By shearing to failure at different σ_2 while preshearing at identical σ_1 a yield locus can be found. From this point on, the acquisition of σ_c and $T_1(x_w)$ is similar to uniaxial compression.

Besides acquiring the sticky-point curve, shear tests have other commonly used applications related to stickiness and powder cohesion. Shear tests are commonly used to quantify the powder flowability. The flowability is described in terms of the flow function, which is the inverse slope in a plot of σ_c versus σ . (Fitzpatrick, Hodnett, et al., 2007; Jenike, 1964; Papadakis & Bahu, 1992; Schulze, 2008). Shear cells can also be used to measure wall friction. This is done by replacing the bottom ring of a shear cell with the wall material. When choosing the wall material similar to industrial surfaces or packaging materials, the adhesion of powder to these substrates can be measured (Papadakis & Bahu, 1992; Schulze, 2008).

Commonly used examples of shear cells are the manual Jenike shear cell (Jenike, 1964), the automated Schulze ring shear test (Schulnies & Kleinschmidt, 2018), or the more recent Freeman FT4 Powder Rheometer (Freeman, 2007) and Anton Paar MCR rheometers (Anton Paar GmbH, 2020; Groen et al., 2020). Conveniently, both the Freeman and Anton Paar powder rheometers can quickly change environmental T and RH independently through powder bed aeration with conditioned airflow (Freeman, 2007; Groen et al., 2020; Mitra et al., 2017). Besides uniaxial compression and shear cells, other types of shear tests for measuring flowability have been reported (e.g., Warren Spring cohesion tester, Peschl shear cell). These were not described as their application to find $T_1(x_w)$ was not found in literature (Pasley et al., 1995).

2.3.3. Penetration test

Penetration tests are similar to the uniaxial compression tests, but use a puncher with a diameter of 1 mm to 2 mm to penetrate the powder bed to a preset depth (Knight & Johnson, 1988). Measurement of the required penetration force F_p , which is a measure for bed strength (Özkan et al., 2002; Özkan et al., 2003), is done after conditioning at a fixed T and RH for a given time. Through repetition, while varying these conditions, the sticky-point curve $T_1(x_w)$ is found for the combinations of T and RH , where the measured F_p equals a predetermined critical value for which the powder is considered sticky (Özkan et al., 2003).

2.3.4. Blow test

The blow test uses a small thin tube to blow air at a powder bed surface. The tube is placed millimeters above the surface at an angle of 45°. The airflow through the tube is increased until particles dislodge from the surface of the conditioned powder bed, which is the endpoint of the blow test. The flow rate of air

at which particles start dislodging is a measure for bed strength (Paterson et al., 2001). The sticky-point curve $T_1(x_w)$ is found at the T and RH where the airflow to dislodge particles reaches a predetermined critical value for which the powder is considered sticky (Foster et al., 2005; Paterson et al., 2005).

A benefit of the blow test is the ability to test multiple times without needing to repeat the consolidation and conditioning step. The powder bed sits on a distributor plate, which sections the powder into multiple parts with an equal amount of powder. Each section of powder is conditioned with the same T and RH and can be measured separately by rotating the thin tube. Therefore, the blow test is convenient when interested in temporal measurements, such as determining the rate of bed strength increase (Paterson et al., 2005).

2.3.5. Comparison of tests

While simplicity is a strength of the visual observation tests, it is also their greatest weakness. The accurate detection of the sticky-point temperature relies on the observer's experience. Based on caking theory, we expect that visible changes in powder properties occur after a high degree of agglomeration has taken place (Kamyabi et al., 2017). Hence, human observers can miss the onset of stickiness, which would cause an over-prediction of the sticky-point temperature. The onset of stickiness can be more precisely quantified with the other tests. Based on the literature, we find that shear tests are more accurate than penetration tests, with less scatter of data and time consolidation effects that are easier to detect (Knight & Johnson, 1988; Schwedes, 2003). Based on these findings, we recommend using uniaxial compression or shear cells instead of penetration tests, in line with Knight and Johnson (1988), who recommended to only use penetrometry in support of shear cell experiments. While shear tests are applied to the bulk of the powder, the blow test is applied to the powder's surface, suggesting that the blow test mostly tests the surface conditions. Blow tests nevertheless create channels in the powder bed (Billings et al., 2006; Paterson et al., 2005), indicating that the bulk is strongly affected by blow test. Hence, we expect that blow tests can be used to determine (bulk) stickiness, similarly to the shear tests. An advantage of the shear tests over the blow test is that the compression during consolidation can be maintained during conditioning, while an advantage of the blow test over the shear tests is that multiple measurements can be performed without having to repeat the consolidation and conditioning steps.

The shear, penetration, and blow tests can be used to quantify bed strength for different T and RH based on the measured parameter (yield strength, penetration force, flow rate). To, in turn, relate bed strength to stickiness, a predetermined value of the critical bed strength is required at which the powder of interest is considered sticky. A way to overcome having to predetermine a critical bed strength is by considering the temporal behavior. Experiments with the blow test, for example, show an initial linear increase of bed strength with time (Foster et al., 2006; Paterson et al., 2005). Similar experiments with shear cells are time-consuming since each test requires repetition of consolidation and conditioning, but suggest a similar linear increase of bed strength with time (Fitzpatrick, Barry, et al., 2007; Fitzpatrick, Hodnett, et al., 2007; Fitzpatrick et al., 2008). By measuring the rate (i.e., slope) of increase for a range of $T - T_g$, one can infer the sticky-point curve $T_1(x_w)$ by plotting the rate versus $T - T_g$ and extrapolating to a rate of zero. In case the critical bed strength is not available a priori, studying the temporal behavior to determine the rate of bed strength increase as a function of $T - T_g$ provides a means to construct the sticky-point curve $T_1(x_w)$.

2.3.6. Application areas of static stickiness tests

Generally, the static stickiness methods are useful in predicting the long-term behavior of powder during storage, transport, or in packaging. In these situations, particles may stick together under the influence of humidity in a process known as caking. This process comprises multiple steps. First, environmental conditions cause particle surfaces to become viscous. Contacting liquid particle surfaces become connected through liquid bridges. Second, the liquid bridges that formed grow in size, increasing powder cohesion. Third, the pores that existed between particles disappear as the liquid fills up the pores (Kamyabi et al., 2017). During the caking process, the bed strength initially increases with time until a maximum value is achieved. As the process continues, the bed strength starts to decrease, attributed to partial

crystallization of material to non-sticky crystals (Fitzpatrick, Hodnett, et al., 2007), as well as a decreased liquid bridge viscosity due to increased liquid adsorption (Hartmann & Palzer, 2011). Static stickiness tests are particularly suitable for assessing the progress of caking by monitoring bed strength as a function of time. Shear tests are particularly useful because they can emulate storage environment conditions in a warehouse or transport vehicle by maintaining a certain level of compression during conditioning and measurement. Using shear cells where the powder can be sheared against a wall material is also applicable to measure powder stickiness in food packaging.

2.4. Dynamic stickiness tests

The class of dynamic stickiness tests covers the tests where particles are not static during conditioning, but set in continuous motion through external means. This introduces particle velocity or contact time between particles as an additional relevant parameter. An overview of dynamic stickiness tests is listed in Table 2.1, showing the measured parameter and the most suitable application. Most dynamic stickiness tests approach the sticky region from the glassy state, while just a few approach it from the liquid state.

Table 2.1: List of methods to measure dynamic stickiness

Method	Measured parameter	Application
Sticky-point test	Torque	Powder mixing
Fluidized bed	Bed collapse/Pressure drop	Fluidized beds: Preventing bed collapse Granulation
Particle gun	Deposited mass	Pneumatic transport Cyclones
Cyclone test	Visual change	Pneumatic transport Cyclones Fluidized beds
Optical test	Scatter intensity	Versatile - opaque powder
Probe test	Tensile force	Droplet evaporation

2.4.1. Sticky-point test

The sticky-point test is the earliest reported method to measure stickiness, hence the name (Lazar et al., 1956). This test has also been referred to as a propeller-driven test (Boonyai et al., 2004). As shown in Figure 2.3, the device uses a container in which a powder with known moisture content x_w is placed. The sample container is submerged in a heating medium to control the powder's temperature. The sample is continuously stirred at fixed angular velocity with a stirring device, and the required torque τ is measured. Typically, a temperature ramp is imposed where the temperature is slowly increased until the

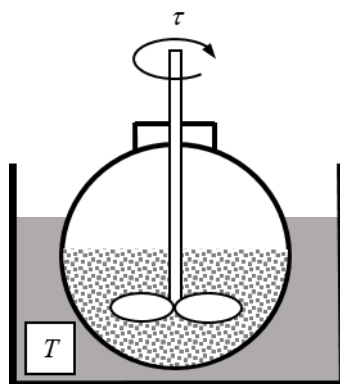


Figure 2.3: A sticky-point test. A powder with known moisture content is placed in a temperature-programmable water bath. The powder is stirred at a fixed angular velocity, and the required torque τ is measured.

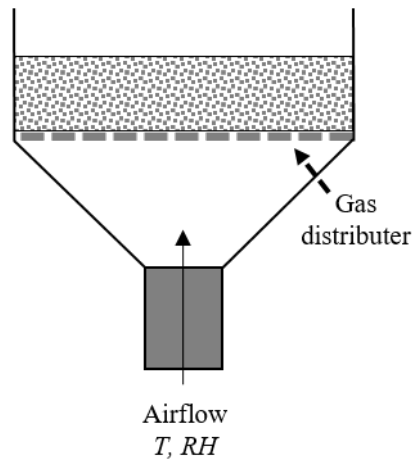


Figure 2.4: A fluidized bed test. The humidity or temperature of the conditioned airflow is increased stepwise until the powder bed collapses.

powder transitions from the glassy to the rubbery state. Above T_g , the cohesive forces increase. Further increase of the temperature leads to particles sticking together, leading to a sharp increase in the required τ . The temperature where this sharp increase is observed is identified as the sticky-point temperature. By repeating the test with different x_w , the sticky-point curve $T_1(x_w)$ can be found.

Detection of the sticky-point in the earliest versions relied on manual stirring. When the stirring had become noticeably more demanding, the sticky-point was reached (Downton et al., 1982; Lazar et al., 1956). More accurate detection methods use automatic stirrers or shear cells equipped with stirrers, which record the τ required for stirring (Özkan et al., 2002; Wallack & King, 1988). Recently, the method has been further improved by utilizing aeration in an Anton Paar rheometer equipped with a propeller (Groen et al., 2020). The option to aerate the powder is used to fluidize the powder, which occurs at a sufficiently high airflow velocity. The powder conditions are controlled by changing the T and RH of the airflow, instead of using a heating medium surrounding the container. The propeller stirs the fluidized powder and measures the required τ . The required τ is substantially smaller than without fluidization, although the rheometers are sufficiently sensitive (Groen et al., 2020). The benefit of aeration or fluidizing is that environmental conditioning occurs rapidly by changing the air's temperature and humidity. In our view, this makes the sticky-point test combined with fluidizing the powder a promising method for measuring dynamic stickiness, both in terms of accuracy and a shorter experimental time.

Besides applying the sticky-point test to free-flowing powder, it has also been used to measure the stickiness of drying liquids. Hence, instead of determining the sticky-point curve $T_1(x_w)$, the tack boundary $T_2(x_w)$ is determined. Kudra (2003) used a laboratory batch dryer equipped with a stirrer to measure the stickiness of drying sludge. They found that the temperature where the torque substantially increased was different from the $T_1(x_w)$ that is found when approaching from the glassy state. The conclusion was that most materials have a sticky-region in which they are sticky, instead of only a sticky-point (Kudra, 2003).

2.4.2. Fluidized bed

As discussed for the sticky-point test, the fluidization of powder reduces the required conditioning time. However, because powder fluidization is highly sensitive to powder cohesiveness, the fluidized bed in isolation is also suitable to measure stickiness. In a fluidized bed, which is shown in Figure 2.4, a powder bed sits in a column while airflow is applied at the bottom. Fluidization causes expansion of the powder bed so that the powder displays fluid-like behavior with a high degree of mixing. The sticky-point curve's acquisition goes as follows: The T or RH of the fluidizing air is increased stepwise. Most commonly, a RH ramp is used at a fixed T by increasing the airflow's humidity. As the cohesiveness increases, there is a point where the fluidized bed collapses (defluidization). The conditions where the collapse of the powder bed is observed, visually, or using pressure drop measurements, is the sticky-point T_1 (Palzer, 2005; Verdurmen

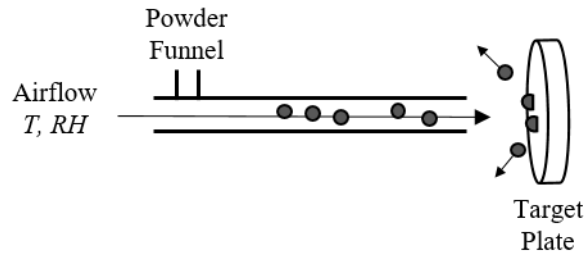


Figure 2.5: The particle gun. Conditioned air flows with high velocity through an air duct. The powder is introduced through a funnel, and the entrained particles hit the target plate. Particles either bounce off or deposit on the plate.

et al., 2006). By repeating the RH ramp at different temperatures, the sticky-point curve $T_1(x_w)$ can be drawn.

In many cases, fluidized bed collapse is detrimental when it occurs. Hence, much research has been done on the detection and prevention of bed collapse (Bartels et al., 2008). Methods such as the attractor comparison method can be used to detect early changes in the bed that indicate an upcoming collapse (Van Ommen, 2001) and have been used to determine the sticky-point curve $T_1(x_w)$ (van der Knaap, 2006; Verschueren et al., 2007). When such detection methods are implemented, the sensitivity of the fluidized bed as a stickiness test is expected to be high.

2.4.3. Particle gun

The particle gun has been designed to measure the sticking of high-velocity particles to a wall and is shown in Figure 2.5. It is a duct through which conditioned air is flowing at high velocity with a target plate at the far end of the duct. For each experiment, a sample of ≈ 25 g powder is introduced into the duct. The particles become entrained in the conditioned air-jet shortly until eventually impacting the target plate. Due to the short exposure of particles to the air, the particle gun relies heavily on the rapid acclimation of the powder surface to environmental conditions. The short acclimation time has consequences for liquid bridge formation as the thin surface region that has adsorbed vapor limits their potential width (Murti et al., 2010). The measured parameter is the percentage of injected powder deposited on the target plate. Plotting this parameter versus $T - T_g$ shows $\approx 0\%$ deposition until a critical value of $T - T_g$ is reached. Above this temperature, deposition is observed and increases linearly with $T - T_g$. The temperature where deposition starts increasing is taken as $T_1(x_w)$ (Zuo et al., 2007).

2.4.4. Cyclone test

The cyclone test, shown in Figure 2.6, uses a cyclone in which conditioned air is circling (Boonyai et al., 2002). When the air is at a steady-state, approximately 1 g of powder is injected at the top of the cyclone. When conditions are such that the powder becomes sticky, particle lumps and powder deposition on the cyclone are observed within minutes. Longer experimental times lead to full immobilization of the powder. The experiment starts at a low RH of the air and is increased stepwise until lumping and deposition are observed visually, which marks a point on the sticky-point curve $T_1(x_w)$.

2.4.5. Optical test

Lockemann (1999) proposed an optical test, shown in Figure 2.7, which uses changes in reflectivity to determine the sticky-point curve. The proposed optical test consists of a rotating test tube containing the free-flowing powder with known (x_w) . The tube is inserted into an oil bath with a programmable temperature. A near-infrared source emits light to the sample while a fiber-optical sensor records the back-scattered signal. The sensor is also immersed in the oil-bath to prevent any refraction of the signal. When particles in the tube stick together, the powder flowability changes, which is observed as a sudden

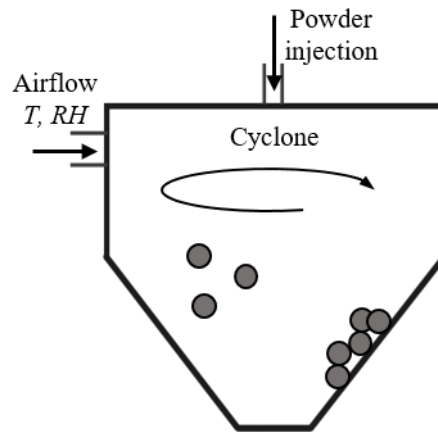


Figure 2.6: A cyclone stickiness test. Conditioned airflow is used to circulate a powder sample through the cyclone. Non-sticky particles remain entrained in the cyclone, while sticky particles can agglomerate or stick to the cyclone wall.

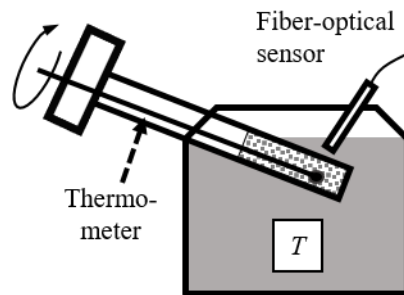


Figure 2.7: The optical test. A rotating sample tube is placed in a heated water bath. A fiber-optical sensor illuminates the sample and receives scattered light. Redrawn from Lockemann (1999).

change in reflectivity. This marks the sticky-point temperature T_1 (Lockemann, 1999). The experiment has to be repeated for different x_w to determine $T_1(x_w)$.

2.4.6. Probe test

The probe test is the only method that is solely applicable to measure stickiness when starting from the liquid state. Hence, instead of the sticky-point curve $T_1(x_w)$, the tack boundary $T_2(x_w)$ is found. The probe test can be applied to liquid films or droplets (J. Chen et al., 2008; Werner et al., 2007b). The approach for either is similar. The droplet probe test is shown in Figure 2.8 and goes as follows: Droplet evaporation is monitored gravimetrically by placing the droplet on a scale (Werner et al., 2007a, 2007b). At some point during evaporation, a probe is lowered with a fixed speed to touch the droplet's surface and then retracted, also with a fixed speed, while the required force for retraction is measured. Hence, this approach is similar to a force measurement with Atomic Force Microscopy (Fabre et al., 2016). The peak tensile force F_{TU} is then determined, which is a measure of the tack, or stickiness, of the sample (Hammond, 1965; Kambe & Kamagata, 1969). By plotting F_{TU} versus drying time, a point is found where F_{TU} increases substantially, marking the tack boundary $T_2(x_w)$ with x_w determined gravimetrically based on the initial solids concentration and the measured weight loss. It should be noted that the measured F_{TU} is influenced by the probe speed and material (Adhikari et al., 2007; Green, 1942). Besides x_w , the sample's temperature T also changes during evaporation, which should be accounted for when determining $T_2(x_w)$ (Schutyser et al., 2019).

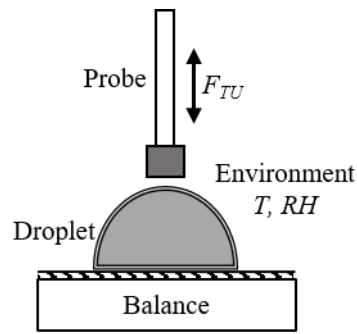


Figure 2.8: The probe test. A probe is lowered until it touches the evaporating droplet. The probe retracts, and the required tensile force F_{TU} is measured. The droplet evaporation is monitored gravimetrically. Redrawn from Boonyai et al. 2004.

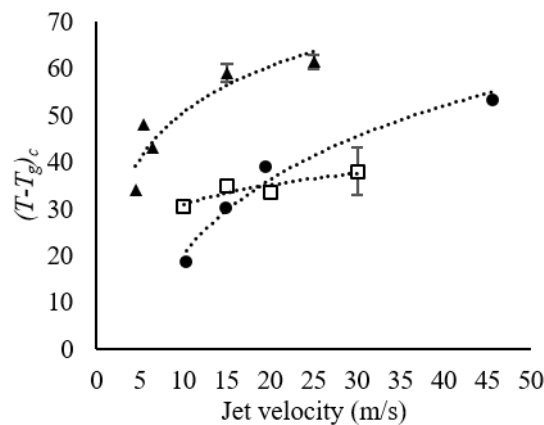


Figure 2.9: Velocity-dependence of $(T - T_g)_c$ using skim milk powder and the particle gun. Triangles ▲ are data by Walmsley et al. (2015); circles ● are data by Zhao (2009), and squares □ are data by Murti et al. (2010). Note that the data cannot be directly compared between authors as different experimental settings were used. Error bars indicate the experimental range for $(T - T_g)_c$ that was reported by the respective authors. The dashed trendlines are to guide the eye.

2.4.7. Comparison of tests

The particle gun, fluidized bed, cyclone test, and optical test use a powder as a starting point, approaching the sticky region from the glassy state to find the sticky-point curve $T_1(x_w)$. The probe test starts from the liquid state and hence can be used to determine the tack boundary $T_2(x_w)$. The sticky-point test can be used starting from the glassy or liquid state and is hence suited for determining both boundaries. The influence of inter-particle contact time was already observed for the static stickiness tests investigating caking. The longer the powder bed is subjected to environmental conditions where the powder will cake, the stronger the powder bed becomes. Control over particle motion and contact time in the dynamic stickiness tests provides a means to investigate the influence of motion within a sample on the boundaries of the sticky region.

Particle motion depends on the angular velocity of the stirrer or the container in the sticky-point and optical tests, on the air velocity in the fluidized bed, cyclone test, and particle gun, and the probe speed in the probe test. A key challenge, in comparing these tests or studying the influence of particle motion on the boundaries of the sticky region, is that particle motion largely differs in all these tests. Even for a single test at a single condition, particle motion may be heterogeneous. In a sticky-point test, for example, stirring can cause the powder to distribute inhomogeneously in the stirring vessel, e.g., due to the stirrer digging channels in the powder. Similarly, in a fluidized bed, the particle velocities are inhomogeneous, mostly due to the common occurrence of bubbling (Seville et al., 2000). Hence, quantification of the relative velocity between the particles, and the resulting inter-particle contact time, presents a challenge,

apart from the particle gun where the particle impact velocity may be controlled and quantified (Murti et al., 2010; Walmsley et al., 2015; Zhao, 2009),

The clearest influence of particle motion has been observed with the particle gun, as shown in Figure 2.9. The data by Murti et al. (2010) shows a minimal increase for $(T - T_g)_c$ with increasing v_i . The data by Walmsley et al. (2015) shows a sharp increase of $(T - T_g)_c$ with increasing v_i , although, at $v_i > 20 \text{ m s}^{-1}$, the effect appears to level off. A similar trend was observed by Zhao (2009) where v_i ranged from 10 m s^{-1} to 45 m s^{-1} . These particle gun experiments show that a larger v_i shifts $T_1(x_w)$ to higher temperatures so that $(T - T_g)_c$ is increased.

The influence of particle motion also becomes apparent when different methods are compared with each other. A static method where the visual change of an SMP bed was used to find $(T - T_g)_c$ was compared with a dynamic fluidized bed method where the pressure change was used to find $(T - T_g)_c$ (Verdurmen et al., 2006). Over an experimental range of $RH = 12\%$ to 30% , the average offset of the sticky-point curve to the T_g was determined. The static test resulted in an average offset of $T - T_g = 13^\circ\text{C}$ and the dynamic stickiness test resulted in an average offset of $T - T_g = 18^\circ\text{C}$. Another example is a comparison between the dynamic fluidized bed- and particle gun tests. The $(T - T_g)_c$ was obtained for both methods using various types of skim- and whole milk powder. While the results varied, for 6 out of 8 samples, the $(T - T_g)_c$ was lower for the fluidized bed by $\approx 10^\circ\text{C}$ to 15°C . For the other two samples, the two methods provided similar results (Murti et al., 2010; Zuo, 2004). Based on these results, we strongly recommend matching the velocity of the particles in the dynamic stickiness test to the application in mind to achieve the most accurate $T_1(x_w)$.

In an attempt to further clarify the influence of particle motion on $(T - T_g)_c$, data from dynamic stickiness tests was gathered in Table 2.2. No data was found for the optical test and data for the probe test could not be used to find $(T - T_g)_c$. For each experiment, the impact velocity v_i of particle collisions was estimated. For the particle gun, the v_i was chosen as the air jet velocity. For the sticky-point test, v_i was estimated as the maximum angular velocity of the stirrer. For the fluidized bed, an average particle velocity \hat{v}_p was estimated using Equation (2.4), with U the superficial velocity and U_{mf} the minimum fluidization velocity (Ennis et al., 1991). The constant α was estimated from Seville et al. (2000) to be $\alpha = 0.53$.

$$\hat{v}_p = \alpha(U - U_{mf}) \quad (2.4)$$

For the data where v_i could be estimated, no clear trend with $(T - T_g)_c$ could be found. Nonetheless, a wide range of $(T - T_g)_c = -5^\circ\text{C}$ to 90°C has been reported. Further analysis indicated that, besides v_i , material and experimental differences can also play a substantial role in determining $(T - T_g)_c$, some of which is highlighted below.

Some outliers can be explained by material differences, e.g. the $(T - T_g)_c = 90^\circ\text{C}$ is for a skim milk powder (SMP) with 80% protein, which is known to decrease stickiness (Hogan & O'Callaghan, 2010). Another example is the low value of -5°C for a fluidized bed experiment using amorphous lactose. Using a range of $RH = 7\%$ to 32% , the results were $(T - T_g)_c = -5^\circ\text{C}$ to 3.8°C with a single outlier of $(T - T_g)_c = 21^\circ\text{C}$ for $RH = 53\%$, the highest humidity tested. Amorphous lactose is known for its early onset of stickiness (Zuo et al., 2007) and crystallization (Schulnies & Kleinschmidt, 2018). We expect the latter could have played a role in the outlier as crystallization reportedly reduces liquid bridge strength (Fitzpatrick, Hodnett, et al., 2007).

However, even for similar materials, the deviation can be quite large. Using SMP in a particle gun with a velocity of 15 m s^{-1} the $(T - T_g)_c$ was found to be 34°C to 36°C by Murti et al. (2010) and 57°C to 61°C by Walmsley et al. (2014). Two experimental differences explained this deviation. In the experiment of Walmsley et al. (2014), the deposition was only measured for the air jet's impingement location, not for the entire target plate. Particles that stray from the jet direction move through the air with undefined T and RH . Hence, the surface conditions of stray particles cannot be accurately determined. Additionally, the target plate was heated to match the temperature of the air jet. The wall- or plate temperature T_p can play an important role and is often a relevant industrial parameter, e.g., in dryers, pneumatic ducts, fluidized beds, and cyclones (Walmsley et al., 2014). A higher T_p is known to reduce the amount of wall deposition (X. D. Chen et al., 1993). Walmsley et al. (2014) found reduced deposition for higher T_p ,

which was consistent regardless of the used v_i . Such wall temperature effects are also found outside of food processing, such as cold spray deposition (Khalkhali & Rothstein, 2020). The improvements of the particle gun made by Walmsley et al. (2014) show that the experimental conditions influence the resulting $T_1(x_w)$. Hence, the experimental conditions need to be accurately chosen when stickiness tests are used for predicting powder processing parameters.

2.4.8. Application areas of dynamic stickiness tests

The moving nature of the particles in dynamic stickiness tests makes these tests useful for predicting the behavior of powder in most of powder production and processing equipment. However, it makes them unsuitable for measuring powder caking. The application of the dynamic tests will depend on the impact velocity v_i of collisions and whether particle-particle or particle-wall collisions are tested.

The particle gun can measure the highest impact velocity of all the reviewed methods and involves particle-wall collisions. Initially, an impact velocity of 20 m s^{-1} was chosen for its similarity to industrial cyclones (Zuo et al., 2007). The high impact velocity makes it a useful method to predict stickiness for high-velocity pneumatic handling, dried material colliding with spray dryer walls, or industrial cyclones. Additionally, by changing the target plate's material or dimensions, the influence of wall material or impact angle can also be investigated (Murti et al., 2010; Walmsley et al., 2015).

The sticky-point test and fluidized bed have continuously moving powder, making these tests useful for various industrial applications involving moving powders such as powder mixing, blending, and milling. Since many industrial processes incorporate a fluidized bed, a stickiness test using fluidized powder will be most applicable to the fluidized bed itself. Limitations of the stirrer's angular velocity and the velocity of fluidization airflow make the sticky-point test and fluidized bed ill-suited for high-velocity processes such as spray drying or pneumatic handling. Further work on the influence of the intensity of continuous mixing on the sticky-point is required to choose experimental conditions for specific applications when using the sticky-point test and the fluidized bed. Using the sticky-point test with a fluidized powder solves some of the issues of the individual methods. However, sensitive equipment is necessary to measure the smaller increase of torque at the sticky-point, compared to without fluidization, which is possible with advanced rheometers (Groen et al., 2020).

The cyclone test was proposed as an alternative for the fluidized bed test, while we expect it to achieve sufficient particle motion to be an alternative for the particle gun as well. Boonyai et al. (2004) suggested that the cyclone test's primary advantage over the fluidized bed is that the cyclone test measures both adhesion and cohesion while the fluidized bed measures only cohesion. Therefore, the cyclone test would be more suitable to predict stickiness in spray drying, fluidized beds, and pneumatic handling of powders (Boonyai et al., 2004). However, it is difficult to judge this statement since, besides the original paper by Boonyai et al. (2002), we only found one application of the cyclone test in literature (Intipunya et al., 2009).

The optical test can be used if the tested material scatters near-infrared light (Boonyai et al., 2004). Since it was proposed, no further experiments using this method have been reported to our knowledge. Hence, no judgment of its applicability can be made momentarily. Still, commonly tested powders such as amorphous lactose and various milk powders are all opaque, indicating that this method could apply to these powders.

The most prominent application for the probe test is the droplet evaporation phase of spray drying. However, the use of a bulk moisture content severely limits this application. Werner et al. (2007b) measured the stickiness of an evaporating droplet with the probe test. The onset of stickiness occurred much earlier than expected based on the droplet's bulk moisture content, which indicated solute had accumulated at the droplet surface. Hence, the gravimetrically determined droplet water content is an unhelpful parameter for determining $T_2(x_w)$, causing the probe test not to apply to industrial processes involving rapid evaporation. Crucially, this includes spray drying, for which there is no adequate method to predict droplet stickiness in the initial evaporation phase. Future methods should focus on the drying droplet's surface conditions for finding the tack point $T_2(x_w)$, either through direct measurement or by modeling the gradient formation under the influence of evaporation (Adhikari et al., 2005).

Table 2.2: A selection of the reviewed literature for dynamic stickiness tests. ^a The $(T - T_g)_c$ was not directly obtainable from the paper, instead, it was calculated using Equation (2.1) and Equation (2.2). ^b A range for fluidization velocity was reported, authors did not test the influence of velocity. SMP15: Skim milk powder with 15 % protein, similar for SMP25, SMP55, and SMP80. Ranges for $(T - T_g)_c$ are mostly due to experimental scatter.

Material	Method	$(T - T_g)_c$ (°C)	v_i (m s ⁻¹)	Ref.
Sucrose & fructose	Sticky-point test	9 to 26 ^a	-	Downton et al., 1982
Amorphous lactose	Fluidized bed	-5 to 21	0.055±0.055 ^b	Zuo et al., 2007
Amorphous lactose	Particle gun	19 to 37	20	Zuo et al., 2007
Amorphous lactose	Particle gun	36 to 40 ^a	20	Paterson, Bronlund, Zuo, et al., 2007
Coffee creamer (maltose)	Fluidized bed	10 to 20 ^a	0.05±0.025 ^b	Groen et al., 2020
High fat cream powder	Particle gun	38	20	Paterson, Zuo, et al., 2007
Low fat cream powder	Particle gun	26	20	Paterson, Zuo, et al., 2007
SMP15	Fluidized bed	10	-	Hogan and O'Callaghan, 2010
SMP25	Fluidized bed	22	-	Hogan and O'Callaghan, 2010
Maltodextrin DE21	Fluidized bed	47 to 62	-	Palzer, 2005
SMP55	Fluidized bed	45	-	Hogan and O'Callaghan, 2010
SMP80	Fluidized bed	90	-	Hogan and O'Callaghan, 2010
Orange juice powder	Sticky-point test	17 to 25 ^a	-	Brennan et al., 1971
SMP	Fluidized bed	14 to 23	-	Verdurmen et al., 2006
SMP	Fluidized bed	29	-	Hogan and O'Callaghan, 2010
SMP	Fluidized bed	25 to 34	0.01	Murti et al., 2010
SMP	Sticky-point test	23	0.3	Hennigs et al., 2001
SMP	Cyclone test	11.4	-	Intipunya et al., 2009
SMP $d < 45 \mu\text{m}$	Particle gun	8.2	10.3	Zhao, 2009
SMP $d < 45 \mu\text{m}$	Particle gun	14.8	19.4	Zhao, 2009
SMP $d = 45 \mu\text{m}$ to $65 \mu\text{m}$	Particle gun	11.6	10.3	Zhao, 2009
SMP $d = 45 \mu\text{m}$ to $65 \mu\text{m}$	Particle gun	23.5	19.4	Zhao, 2009
SMP	Particle gun	18.6	10.3	Zhao, 2009
SMP	Particle gun	30.1	14.8	Zhao, 2009
SMP	Particle gun	39	19.4	Zhao, 2009
SMP	Particle gun	53.4	45.6	Zhao, 2009
SMP	Particle gun	34	4.5	Walmsley et al., 2015
SMP	Particle gun	48	5.4	Walmsley et al., 2014
SMP	Particle gun	43	6.5	Walmsley et al., 2015
SMP	Particle gun	30 to 31	10	Murti et al., 2010
SMP	Particle gun	34 to 36	15	Murti et al., 2010
SMP	Particle gun	57 to 61	15	Walmsley et al., 2014
SMP	Particle gun	32 to 35	20	Murti et al., 2010
SMP	Particle gun	60 to 63	25	Walmsley et al., 2014
SMP	Particle gun	33 to 43	30	Murti et al., 2010
Tomato powder	Sticky-point test	36 to 41 ^a	-	Lazar et al., 1956
White cheese powder	Particle gun	28	20	Paterson, Zuo, et al., 2007
Whole milk powder	Fluidized bed	23 to 38	0.09	Zuo et al., 2007
Whole milk powder	Particle gun	38 to 61	20	Zuo et al., 2007
Whole milk powder	Sticky-point test	36 to 41 ^a	1.0	Özkan et al., 2002

2.5. Conclusion

In this review, we provided an overview of methods that measure the stickiness of amorphous powders relevant in the food industry. The reviewed methods included visual observation tests, shear tests, the penetration test, the blow test, the sticky-point test, the fluidized bed, the particle gun, the cyclone test, the optical test, and the probe test. For each method, we described how either the sticky-point temperature $T_1(x_w)$ or the tack boundary $T_2(x_w)$ can be determined. We have classified the methods based on the particle mobility during the conditioning and measurement steps into *static stickiness tests* and *dynamic stickiness tests*.

Static stickiness tests have limited particle motion during the conditioning step, which can be as long as desired. Therefore, these tests are particularly suitable to measure the caking rate of powder beds. Hence, industrial applicability is predominantly in predicting the long-term behavior of powder during storage or in packaging. Static stickiness tests have shown that the caking rate can be related to $T - T_g$ when $T - T_g > (T - T_g)_c$, although the nature of the relation is dependent on the used method. Nonetheless, this approach gives much insight into the stability of stored powders.

Dynamic stickiness tests involve particles with significant particle motion during the conditioning and measurement step. The particle gun is a good method to measure stickiness during particle-wall impacts, while the combination of the sticky-point test and fluidized bed measure stickiness for particle-particle collisions and continuously mixed systems. A wide range of testing conditions can be achieved by varying the impact velocity or contact time between particles. Hence, information from dynamic stickiness tests is highly relevant to the design and operation of powder production and processing equipment. Dynamic stickiness tests have shown that velocity plays an important role in the location of the sticky region, with larger velocity shifting the sticky-point curve $T_1(x_w)$ to higher temperatures so that a larger $(T - T_g)_c$ is obtained.

An essential type of stickiness test that is lacking is a dynamic test that measures particle stickiness when moving from the liquid state to the sticky-region, hence, finding the tack boundary $T_2(x_w)$. Much unclarity exists for when evaporating solute-containing droplets are sticky, while this is hugely relevant for one of the most used processes in the food processing industry - spray drying. The probe method does approach the sticky-region from the liquid state, but the reliance on the droplet's bulk properties makes it unable to determine values for $T_2(x_w)$. Further work in predicting the surface stickiness, either through direct measurement or by modeling the gradient formation under the influence of evaporation, is required to predict droplet stickiness.

Bibliography

- Adhikari, B., Howes, T., Shrestha, A. K., & Bhandari, B. R. (2007). Development of stickiness of whey protein isolate and lactose droplets during convective drying. *Chemical Engineering and Processing: Process Intensification*, 46(5), 420–428. <https://doi.org/10.1016/j.cep.2006.07.014>
- Adhikari, B., Howes, T., Lecomte, D., & Bhandari, B. R. (2005). A glass transition temperature approach for the prediction of the surface stickiness of a drying droplet during spray drying. *Powder Technology*, 149(2-3), 168–179. <https://doi.org/10.1016/j.powtec.2004.11.007>
- Aguilera, J. M., Levi, G., & Karel, M. (1993). Effect of water content on the glass transition and caking of fish protein hydrolyzates. *Biotechnology Progress*, 9(6), 651–654. <https://doi.org/10.1021/bp00024a013>
- Anton Paar GmbH. (2020, May 21). *Modular compact rheometer: MCR 102/302/502*. <https://www.anton-paar.com/us-en/products/details/rheometer-mcr-102-302-502/>
- Bartels, M., Lin, W., Nijenhuis, J., Kapteijn, F., & Van Ommen, J. R. (2008). Agglomeration in fluidized beds at high temperatures: Mechanisms, detection and prevention. *Progress in Energy and Combustion Science*, 34(5), 633–666. <https://doi.org/10.1016/j.peccs.2008.04.002>
- Billings, S. W., Bronlund, J. E., & Paterson, A. H. J. (2006). Effects of capillary condensation on the caking of bulk sucrose. *Journal of food engineering*, 77(4), 887–895. <https://doi.org/10.1016/j.jfoodeng.2005.08.031>

- Boonyai, P., Bhandari, B. R., & Howes, T. (2002). Development of a novel testing device to characterize the sticky behavior of food powders—a preliminary study (V. K. Jindal, Ed.). In V. K. Jindal (Ed.), *Intl conf on innovations in food processing tech & eng*, AIT, Bangkok.
- Boonyai, P., Bhandari, B., & Howes, T. (2004). Stickiness measurement techniques for food powders: A review. *Powder Technology*, *145*(1), 34–46. <https://doi.org/10.1016/j.powtec.2004.04.039>
- Brennan, J. G., Herrera, J., & Jowitt, R. (1971). A study of some of the factors affecting the spray drying of concentrated orange juice, on a laboratory scale. *International Journal of Food Science & Technology*, *6*(3), 295–307. <https://doi.org/10.1111/j.1365-2621.1971.tb01618.x>
- Burnett, D. J., Thielmann, F., & Booth, J. (2004). Determining the critical relative humidity for moisture-induced phase transitions. *International journal of pharmaceuticals*, *287*(1-2), 123–133. <https://doi.org/10.1016/j.ijpharm.2004.09.009>
- Chen, J., Feng, M., Gonzalez, Y., & Pugaloni, L. A. (2008). Application of probe tensile method for quantitative characterisation of the stickiness of fluid foods. *Journal of food engineering*, *87*(2), 281–290. <https://doi.org/10.1016/j.jfoodeng.2007.12.004>
- Chen, X. D., Lake, R., & Jebson, S. (1993). Study of milk powder deposition on a large industrial dryer. *Food and Bioproducts processing*, *71*, 180–186.
- Dagdug, L., & Garca-Coln, L. S. (1998). Generalization of the williams–landel–ferry equation. *Physica A: Statistical Mechanics and its Applications*, *250*(1-4), 133–141. [https://doi.org/10.1016/s0378-4371\(97\)00542-6](https://doi.org/10.1016/s0378-4371(97)00542-6)
- Downton, G. E., Flores-Luna, J. L., & King, C. J. (1982). Mechanism of stickiness in hygroscopic, amorphous powders. *Industrial & Engineering Chemistry Fundamentals*, *21*(4), 447–451. <https://doi.org/10.1021/i100008a023>
- Ennis, B. J., Tardos, G., & Pfeffer, R. (1991). A microlevel-based characterization of granulation phenomena. *Powder Technology*, *65*(1-3), 257–272. [https://doi.org/10.1016/0032-5910\(91\)80189-p](https://doi.org/10.1016/0032-5910(91)80189-p)
- Fabre, A., Salameh, S., Ciacchi, L. C., Kreutzer, M. T., & van Ommen, J. R. (2016). Contact mechanics of highly porous oxide nanoparticle agglomerates. *Journal of Nanoparticle Research*, *18*(7), 200. <https://doi.org/10.1007/s11051-016-3500-4>
- Ferry, J. D. (1980). *Viscoelastic properties of polymers*. John Wiley & Sons.
- Fitzpatrick, J. J., Barry, K., Cerqueira, P. S. M., Iqbal, T., Oneill, J., & Roos, Y. H. (2007). Effect of composition and storage conditions on the flowability of dairy powders. *International Dairy Journal*, *17*(4), 383–392. <https://doi.org/10.1016/j.idairyj.2006.04.010>
- Fitzpatrick, J. J., Hodnett, M., Twomey, M., Cerqueira, P. S. M., O'flynn, J., & Roos, Y. H. (2007). Glass transition and the flowability and caking of powders containing amorphous lactose. *Powder Technology*, *178*(2), 119–128. <https://doi.org/10.1016/j.powtec.2007.04.017>
- Fitzpatrick, J. J., O'Callaghan, E., & O'Flynn, J. (2008). Application of a novel cake strength tester for investigating caking of skim milk powder. *Food and Bioproducts Processing*, *86*(3), 198–203. <https://doi.org/10.1016/j.fbp.2007.10.009>
- Foster, K. D., Bronlund, J. E., & Paterson, A. H. J. T. (2006). Glass transition related cohesion of amorphous sugar powders. *Journal of Food Engineering*, *77*(4), 997–1006. <https://doi.org/10.1016/j.jfoodeng.2005.08.028>
- Foster, K. D., Bronlund, J. E., & Paterson, A. T. (2005). The contribution of milk fat towards the caking of dairy powders. *International Dairy Journal*, *15*(1), 85–91. <https://doi.org/10.1016/j.idairyj.2004.05.005>
- Freeman, R. (2007). Measuring the flow properties of consolidated, conditioned and aerated powders—a comparative study using a powder rheometer and a rotational shear cell. *Powder Technology*, *174*(1-2), 25–33. <https://doi.org/10.1016/j.powtec.2006.10.016>
- Frenkel, J. J. (1945). Viscous flow of crystalline bodies under the action of surface tension. *J. phys.*, *9*, 385.
- Green, H. (1942). What is tack? *Paper Trade Journal*, *114*, 39–42.
- Groen, J. C., Kooijman, W., van Belzen, D., Meesters, G. M. H., Schütz, D., Aschl, T., & Verolme, P. (2020). Real-time in-situ rheological assessment of sticky point temperature and humidity of powdered products. *KONA Powder and Particle Journal*, 2020006. <https://doi.org/10.14356/kona.2020006>

- Hammond, J. F. H. (1965, November). *Tack testing apparatus* (US3214971A) [US Patent 3,214,971]. Google Patents. US Patent 3,214,971.
- Hartmann, M., & Palzer, S. (2011). Caking of amorphous powders: material aspects, modelling and applications. *Powder Technology*, *206*(1-2), 112–121. <https://doi.org/10.1016/j.powtec.2010.04.014>
- Hennigs, C., Kockel, T. K., & Langrish, T. A. G. (2001). New measurements of the sticky behavior of skim milk powder. *Drying technology*, *19*(3-4), 471–484. <https://doi.org/10.1081/drt-100103929>
- Hogan, S. A., Famelart, M. H., O'Callaghan, D. J., & Schuck, P. (2010). A novel technique for determining glass–rubber transition in dairy powders. *Journal of food engineering*, *99*(1), 76–82. <https://doi.org/10.1016/j.jfoodeng.2010.01.040>
- Hogan, S. A., & O'Callaghan, D. J. (2010). Influence of milk proteins on the development of lactose-induced stickiness in dairy powders. *International dairy journal*, *20*(3), 212–221. <https://doi.org/10.1016/j.idairyj.2009.11.002>
- Intipunya, P., Shrestha, A., Howes, T., & Bhandari, B. (2009). A modified cyclone stickiness test for characterizing food powders. *Journal of food engineering*, *94*(3-4), 300–306. <https://doi.org/10.1016/j.jfoodeng.2009.03.024>
- Jenike, A. W. (1964). Storage and flow of solids. *Bulletin No. 123, Utah State University*.
- Kambe, H., & Kamagata, K. (1969). A method of measuring tackiness. *Journal of Applied Polymer Science*, *13*(3), 493–504. <https://doi.org/10.1002/app.1969.070130310>
- Kamyabi, M., Sotudeh-Gharebagh, R., Zarghami, R., & Saleh, K. (2017). Principles of viscous sintering in amorphous powders: A critical review. *Chemical Engineering Research and Design*, *125*, 328–347. <https://doi.org/10.1016/j.cherd.2017.06.009>
- Katkov, I. I., & Levine, F. (2004). Prediction of the glass transition temperature of water solutions: Comparison of different models. *Cryobiology*, *49*(1), 62–82. <https://doi.org/10.1016/j.cryobiol.2004.05.004>
- Khalkhali, Z., & Rothstein, J. P. (2020). Characterization of the cold spray deposition of a wide variety of polymeric powders. *Surface and Coatings Technology*, *383*, 125251. <https://doi.org/10.1016/j.surfcoat.2019.125251>
- Knight, P. C., & Johnson, S. H. (1988). Measurement of powder cohesive strength with a penetration test. *Powder technology*, *54*(4), 279–283. [https://doi.org/10.1016/0032-5910\(88\)80058-5](https://doi.org/10.1016/0032-5910(88)80058-5)
- Kudra, T. (2003). Sticky region in drying: definition and identification. *Drying Technology*, *21*(8), 1457–1469. <https://doi.org/10.1081/DRT-120024678>
- Lazar, M. E., Brown, A. H., Smith, G. S., Wong, F. F., & Lindquist, F. E. (1956). Experimental production of tomato powder by spray drying. *Food Technology*, *10*(3), 129–134.
- Li, R., Lin, D., Roos, Y. H., & Miao, S. (2019). Glass transition, structural relaxation and stability of spray-dried amorphous food solids: A review. *Drying Technology*, *37*(3), 287–300. <https://doi.org/10.1080/07373937.2018.1459680>
- Lockemann, C. A. (1999). A new laboratory method to characterize the sticking properties of free-flowing solids. *Chemical Engineering and Processing: Process Intensification*, *38*(4-6), 301–306. [https://doi.org/10.1016/s0255-2701\(99\)00021-5](https://doi.org/10.1016/s0255-2701(99)00021-5)
- Lomellini, P. (1992). Williams-landel-ferry versus arrhenius behaviour: Polystyrene melt viscoelasticity revisited. *Polymer*, *33*(23), 4983–4989. [https://doi.org/10.1016/0032-3861\(92\)90049-3](https://doi.org/10.1016/0032-3861(92)90049-3)
- Mitra, H., Pushpadass, H. A., Franklin, M. E. E., Ambrose, R. P. K., Ghoroi, C., & Battula, S. N. (2017). Influence of moisture content on the flow properties of basundi mix. *Powder technology*, *312*, 133–143. <https://doi.org/10.1016/j.powtec.2017.02.039>
- Murti, R. A., Paterson, A. T. H. J., Pearce, D., & Bronlund, J. E. (2010). The influence of particle velocity on the stickiness of milk powder. *International Dairy Journal*, *20*(2), 121–127. <https://doi.org/10.1016/j.idairyj.2009.08.005>
- Özkan, N., Walisinghe, N., & Chen, X. D. (2002). Characterization of stickiness and cake formation in whole and skim milk powders. *Journal of Food Engineering*, *55*(4), 293–303. [https://doi.org/10.1016/s0260-8774\(02\)00104-8](https://doi.org/10.1016/s0260-8774(02)00104-8)
- Özkan, N., Withy, B., & Chen, X. D. (2003). Effects of time, temperature, and pressure on the cake formation of milk powders. *Journal of food engineering*, *58*(4), 355–361. [https://doi.org/10.1016/s0260-8774\(02\)00419-3](https://doi.org/10.1016/s0260-8774(02)00419-3)

- Palzer, S. (2005). The effect of glass transition on the desired and undesired agglomeration of amorphous food powders. *Chemical Engineering Science*, *60*(14), 3959–3968. <https://doi.org/10.1016/j.ces.2005.02.015>
- Palzer, S., & Zürcher, U. (2004). Kinetik unerwünschter agglomerationsprozesse bei der lagerung und verarbeitung amorpher lebensmittelpulver. *Chemie Ingenieur Technik*, *76*(10), 1594–1599. <https://doi.org/10.1002/cite.200407009>
- Papadakis, S. E., & Bahu, R. E. (1992). The sticky issues of drying. *Drying Technology*, *10*(4), 817–837. <https://doi.org/10.1080/07373939208916484>
- Pasley, H., Haloulos, P., & Ledig, S. (1995). Stickiness—a comparison of test methods and characterisation parameters. *Drying Technology*, *13*(5-7), 1587–1601. <https://doi.org/10.1080/07373939508917041>
- Paterson, A. H. J., Bronlund, J. E., & Brooks, G. F. (2001). The blow test for measuring the stickiness of powders, In *Conference of food engineering*.
- Paterson, A. H. J., Bronlund, J. E., Zuo, J. Y., & Chatterjee, R. (2007). Analysis of particle-gun-derived dairy powder stickiness curves. *International dairy journal*, *17*(7), 860–865. <https://doi.org/10.1016/j.idairyj.2006.08.013>
- Paterson, A. H. J., Brooks, G. F., Bronlund, J. E., & Foster, K. D. (2005). Development of stickiness in amorphous lactose at constant t- tg levels. *International Dairy Journal*, *15*(5), 513–519. <https://doi.org/10.1016/j.idairyj.2004.08.012>
- Paterson, A. H. J., Ripberger, G. D., & Bridges, R. P. (2015). Measurement of the viscosity of freeze dried amorphous lactose near the glass transition temperature. *International Dairy Journal*, *43*, 27–32. <https://doi.org/10.1016/j.idairyj.2014.11.005>
- Paterson, A. H. J., Zuo, J. Y., Bronlund, J. E., & Chatterjee, R. (2007). Stickiness curves of high fat dairy powders using the particle gun. *International dairy journal*, *17*(8), 998–1005. <https://doi.org/10.1016/j.idairyj.2006.11.001>
- Peleg, M. (1992). On the use of the wlf model in polymers and foods. *Critical Reviews in Food Science & Nutrition*, *32*(1), 59–66. <https://doi.org/10.1080/10408399209527580>
- Roos, Y. H. (2002). Importance of glass transition and water activity to spray drying and stability of dairy powders. *Le Lait*, *82*(4), 475–484. <https://doi.org/10.1051/lait:2002025>
- Roos, Y. H. (2010). Glass transition temperature and its relevance in food processing. *Annual Review of Food Science and Technology*, *1*, 469–496. <https://doi.org/10.1146/annurev.food.102308.124139>
- Schulnies, F., & Kleinschmidt, T. (2018). Time consolidation of skim milk powder near the glass transition temperature. *International Dairy Journal*, *85*, 105–111. <https://doi.org/10.1016/j.idairyj.2018.05.005>
- Schulze, D. (2008). *Powders and bulk solids* (Vol. 22). Springer.
- Schutysen, M. A. I., Both, E. M., Siemons, I., Vaessen, E. M. J., & Zhang, L. (2019). Gaining insight on spray drying behavior of foods via single droplet drying analyses. *Drying Technology*, *37*(5), 525–534.
- Schwedes, J. (2003). Review on testers for measuring flow properties of bulk solids. *Granular matter*, *5*(1), 1–43. <https://doi.org/10.1007/s10035-002-0124-4>
- Seville, J. P. K., Willett, C. D., & Knight, P. C. (2000). Interparticle forces in fluidisation: A review. *Powder Technology*, *113*(3), 261–268. [https://doi.org/10.1016/s0032-5910\(00\)00309-0](https://doi.org/10.1016/s0032-5910(00)00309-0)
- Simha, R., & Boyer, R. F. (1962). On a general relation involving the glass temperature and coefficients of expansion of polymers. *The Journal of Chemical Physics*, *37*(5), 1003–1007. <https://doi.org/10.1063/1.1733201>
- Sochava, I. V. (1997). Heat capacity and thermodynamic characteristics of denaturation and glass transition of hydrated and anhydrous proteins. *Biophysical chemistry*, *69*(1), 31–41. [https://doi.org/10.1016/s0301-4622\(97\)00072-0](https://doi.org/10.1016/s0301-4622(97)00072-0)
- Tsourouflis, S., Flink, J. M., & Karel, M. (1976). Loss of structure in freeze-dried carbohydrates solutions: Effect of temperature, moisture content and composition. *Journal of the Science of Food and Agriculture*, *27*(6), 509–519. <https://doi.org/10.1002/jsfa.2740270604>
- van der Knaap, J. (2006). *On-line monitoring of dynamic stickiness and particle size distribution in a fluidized bed dryer by attractor comparison* (MSc Thesis). Delft University of Technology.

- Van Ommen, J. R. (2001). *Monitoring fluidized bed hydrodynamics* (Doctoral dissertation). Delft University of Technology. Delft University Press.
- Verdurmen, R. E. M., Houwelingen, G. v., Gusing, M., Verschuere, M., & Straatsma, J. (2006). Agglomeration in spray drying installations (the edecad project): Stickiness measurements and simulation results. *Drying Technology*, *24*(6), 721–726. <https://doi.org/10.1080/07373930600684973>
- Verschuere, M., Verdurmen, R. E. M., van Houwelingen, G., Backx, A. C. P. M., van der Knaap, J. E. A., Bartels, M., Nijenhuis, J., & van Ommen, J. R. (2007). Dynamic stickiness measurements by attractor comparison: A feasibility study, In *Proc. int. conf. liquid atomisation and spray systems (iclass), aug 27–sept 1, 2007, kyoto, japan*.
- Wallack, D. A., & King, C. J. (1988). Sticking and agglomeration of hygroscopic, amorphous carbohydrate and food powders. *Biotechnology Progress*, *4*(1), 31–35. <https://doi.org/10.1002/btpr.5420040106>
- Walmsley, T. G., Walmsley, M. R. W., Atkins, M. J., & Neale, J. R. (2015). Analysis of skim milk powder deposition on stainless steel tubes in cross-flow. *Applied Thermal Engineering*, *75*, 941–949. <https://doi.org/10.1016/j.applthermaleng.2014.10.066>
- Walmsley, T. G., Walmsley, M. R. W., Atkins, M. J., Neale, J. R., & Sellers, C. M. (2014). An experimentally validated criterion for skim milk powder deposition on stainless steel surfaces. *Journal of food engineering*, *127*, 111–119. <https://doi.org/10.1016/j.jfoodeng.2013.11.025>
- Werner, S. R. L., Jones, J. R., & Paterson, A. H. J. (2007a). Stickiness during drying of amorphous skin-forming solutions using a probe tack test. *Journal of food engineering*, *81*(4), 647–656. <https://doi.org/10.1016/j.jfoodeng.2006.12.008>
- Werner, S. R. L., Jones, J. R., & Paterson, A. H. J. (2007b). Stickiness of maltodextrins using probe tack test during in-situ drying. *Journal of food engineering*, *80*(3), 859–868. <https://doi.org/10.1016/j.jfoodeng.2006.08.008>
- Williams, M. L., Landel, R. F., & Ferry, J. D. (1955). The temperature dependence of relaxation mechanisms in amorphous polymers and other glass-forming liquids. *Journal of the American Chemical Society*, *77*(14), 3701–3707. <https://doi.org/10.1021/ja01619a008>
- Zhao, S. (2009). *Experimental and numerical investigations of skim milk powder stickiness and deposition mechanisms* (Masters Degree Thesis). University of Waikato.
- Zuo, J. Y. (2004). *The stickiness curve of dairy powders* ((M. Tech. thesis)). Massey University. Palmerston North, New Zealand. <https://hdl.handle.net/10289/4318>
- Zuo, J. Y., Paterson, A. H. J., Bronlund, J. E., & Chatterjee, R. (2007). Using a particle-gun to measure initiation of stickiness of dairy powders. *International Dairy Journal*, *17*(3), 268–273. <https://doi.org/10.1016/j.idairyj.2006.02.010>

3

Revealing how maltodextrin-containing droplets dry using optical coherence tomography

Properties of powders produced from drying solute-containing droplets arise from the dynamic redistribution of solute during drying. While insights on the dynamic redistribution are instrumental for the rational design of powders and for the optimized operation of equipment such as spray dryers, experimental techniques that allow measuring the spatio-temporal concentration of solute in drying droplets are scarce. In this work, we explore and demonstrate the use of optical coherence tomography (OCT) to measure the spatio-temporal concentration of solute in drying droplets and the development of a solidifying shell at the liquid-air interface, using aqueous droplets of maltodextrin as a model system. This work provides a solid foundation for the use of OCT to quantify the dynamic redistribution of solute and link it to the development of the morphology of the produced particles and agglomerates.

Published as: Erik J.G. Sewalt, Jeroen Kalkman, J. Ruud van Ommen, Gabrie M.H. Meesters, Volkert van Steijn (2022). Revealing how maltodextrin-containing droplets dry using optical coherence tomography. *Food Research International*, 111049. <https://doi.org/10.1016/j.foodres.2022.111049>.

3.1. Introduction

Production of powders from solute-containing microdroplets is fundamental to various processing technologies in the food and pharmaceutical sector (Santos et al., 2018). Bulk properties of powders, such as flowability and dispersibility, are dictated by the morphology of the produced agglomerates. Inspection of powders from processes such as spray drying shows that agglomerates consist of particles with a wide range of morphologies, including solid and hollow particles, with smooth, crumbled, or broken shells (Walton, 2000). The morphology of individual particles stems from the dynamic interplay between the evaporation of solvent from the droplets and the redistribution of solute such as carbohydrates, fibers, or proteins inside them (Sadek et al., 2015). Solute can continuously redistribute in the interior of slow-drying droplets by diffusion, leading to solid particles without shells. Conversely, solute accumulates at the surface of fast-drying droplets, leading to particles with shells that may buckle depending on their morphology and composition (Bansal et al., 2015; Vehring et al., 2007). The distribution of solute also governs the dynamic properties of the droplets' surfaces that can temporarily become sticky, which promotes the formation of agglomerates through collisions with other semi-wet particles (Sewalt et al., 2020; van der Hoeven, 2008). A deep understanding of the dynamic redistribution of solute in drying droplets is instrumental for two main reasons: First, from a particle engineering perspective, it allows for the engineering of the final powder structure. Second, from a process engineering perspective, it helps to determine processing boundaries, enabling a more cost-efficient design of equipment such as spray dryers.

Experimental techniques to study the drying of solute-containing droplets allow immobilization of the droplet by deposition on a flat solid surface, levitation in air, or suspension from a needle. While brightfield imaging of such droplets elucidates the drying kinetics and morphological changes (Fu et al., 2012; Sadek et al., 2015), measuring the dynamic redistribution of solute inside drying droplets presents a significant challenge (Schutyser et al., 2019). A fully dried particle's surface can be characterized *ex situ* with x-ray photoelectron spectroscopy (XPS) and confocal Raman spectroscopy, showing the influence of solute component properties on phase segregation (Both et al., 2018; Munoz-Ibanez et al., 2016; Nuzzo et al., 2017; Nuzzo et al., 2015). Arresting the state of the droplet at different instants during the drying process by flash-freezing with liquid nitrogen provides a means to construct the dynamics through *ex situ* characterization of the chemical surface composition with XPS and the internal distribution with confocal microscopy (Foerster et al., 2016). Techniques for *in situ* probing the redistribution of solute in drying micro-droplets are scarce (de Souza Lima et al., 2020; Lemoine and Castanet, 2013; Schutyser et al., 2019). Examples include rainbow refractometry (Lemoine and Castanet, 2013), which becomes inaccurate upon introduction of gradients in the refractive index, nuclear magnetic resonance spectroscopy (Griffith et al., 2008), which is limited in spatial and temporal resolution, and Raman spectroscopy (Quiño et al., 2015; Tuckermann et al., 2009). Quiño et al. (2015) successfully used *in situ* Raman microscopy to measure the component distribution of a large acetone-water droplet ($d \approx 2$ mm) evaporating in an acoustic levitator. However, improving the resolution below $120 \mu\text{m}$ was difficult due to light distortion near the liquid-air interface (de Souza Lima et al., 2020). A promising *in situ* method is laser speckle imaging (LSI), as it can non-invasively probe inside turbid droplets at high spatial and temporal resolution. LSI was used to visualize colloid particle mobility and the 'coffee ring' effect in a drying paint droplet with a spatial resolution up to $5 \mu\text{m}$ (Van Der Kooij et al., 2016). Another promising technique, which has received limited attention for the application to drying droplets, and specifically for measuring the dynamic solute distribution, is optical coherence tomography (OCT) (Koponen and Haavisto, 2020). OCT was originally developed for the field of ophthalmology and is a non-intrusive imaging technique that allows characterization of opaque samples. It is based on a Michelson interferometer that uses the back-scattering of near-infrared light for imaging samples (Izatt et al., 2015). The application to droplets has focused on visualization of internal flow patterns (Edwards et al., 2018; Manukyan et al., 2013; Srinivasan et al., 2003), visualization of phase changes (Davidson et al., 2017), monitoring of rehydration (Lee et al., 2016). In our view, OCT also has a high potential to *in situ* measure the dynamic distribution of solute and development of internal structures in evaporating droplets with micrometer resolution.

In this work, we explore the use of OCT for the *in situ* measurement of the dynamic distribution of solute during the drying of turbid solute-containing droplets. We use a sessile maltodextrin droplet as the model system, as maltodextrins are common in the food industry and their influence on dried particle morphology

is well known (Both et al., 2018; Both et al., 2019; Siemons et al., 2020). We demonstrate that OCT can be used to measure the drying kinetics, the solute distribution, the formation of a shell, and the internal convective flows. We demonstrate a method to map the component concentration in a drying droplet by quantifying the diffusivity of tracer particles, which can be used to estimate the local viscosity, and hence maltodextrin concentration, with at least order-of-magnitude accuracy. This work provides a solid foundation for using OCT as a characterization method for drying droplets, where the insights could guide the design of powders with desired properties. Additionally, thus obtained data is crucial for the validation of theoretical/numerical models of droplet drying (Meerdink and van't Riet, 1995; Mezhericher et al., 2010).

3.2. Materials and methods

3.2.1. Solution preparation

Maltodextrin with a dextrose equivalent of 12 (MD12, Glucidex) was mixed with deionized water to obtain a 10 wt% MD12 solution, which has a viscosity of 1.1 mPa s (Both et al., 2019). A 10 wt% MD12 concentration was chosen to illustrate the possibilities of the OCT measurements, because drying of this solution does result in the formation of a detectable skin at the interface, while the viscosity remains sufficiently low throughout the drying process to characterize it with the chosen OCT settings. Contrast in the OCT measurements was enhanced by addition of titanium dioxide nanoparticles (TiO₂ P25 AEROXIDE) at a concentration of 0.1 wt%. Individual TiO₂ nanoparticles have a diameter of 25 nm, but they form larger agglomerates. The size of the TiO₂ agglomerates was measured before the measurements, as explained later. We will refer to these agglomerates as TiO₂ particles throughout this paper. While the agglomeration affected their size, requiring calibration of the size in the solution, we found that the optical advantages of TiO₂ outweighed this disadvantage.

3.2.2. Substrate preparation

Sylgard 184 Poly(dimethylsiloxane) (PDMS) elastomer and curing agent were obtained for making a superhydrophobic substrate. PDMS was degassed, poured onto polishing sandpaper (30 000 grains/cm², Airbrush, Almere), and subsequently cured at 70 °C overnight. Removal of the sandpaper resulted in a PDMS substrate with micro-roughness. The contact angle was determined optically from droplets of Milli-Q water deposited on top of the substrate. The resulting contact angle was 154±4°.

3.2.3. Droplet drying experiment

Droplets were generated and ejected onto the superhydrophobic substrate using a PipeJet P9 NanoDispenser (BioFluidix GmbH, Freiburg, Germany) equipped with a nozzle having an orifice size of 500 μm. Using a stroke of 100 % and a stroke velocity of 80 μm s⁻¹, we generated droplets with a volume of 42.2 nL, giving an equivalent spherical diameter of 432 μm. Immediately after droplet deposition on the substrate, the substrate was placed on a micro stage under the imaging head of the OCT system, with the imaging direction in the axial (z) direction, perpendicular to the substrate, see Figure 3.1. The micro stage allowed for rapid and precise placement of the droplets. The approximate time between dispensing the droplet and the start of OCT imaging was 9 s. During imaging, droplets evaporated in ambient air with a temperature of 20 °C and a relative humidity of 35 %. Their full evaporation took approximately 240 s.

3.2.4. Optical Coherence Tomography measurements

Measurements on the droplets were made with a high-resolution spectral-domain OCT system (Ganymede-II-HR, Thorlabs Inc., Germany). This system was equipped with a long working distance lens (OCT-LK4-BB lens, Thorlabs Inc., Germany) and used near-infrared light with a center wavelength of $\lambda_c = 900$ nm and a bandwidth of 195 nm (Callewaert et al., 2017). It allowed imaging up to a depth of 1.89 mm, which is four times larger than the height of the droplets. By overlapping the focus point of the OCT sample arm with the droplet, the strength of the signal was maximized.

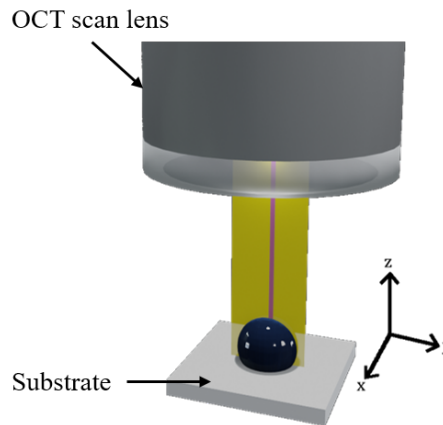


Figure 3.1: Rendered image of the optical coherence tomography setup with a sessile maltodextrin (MD12) droplet. The yellow sheet indicates the orientation of the 2D scans. The magenta line indicates the orientation of the 1D scans.

Two types of OCT measurements were performed on the drying droplets, a sequence of 1D scans performed at a fixed location showing the fast dynamics along a 1D line and a sequence of 1D scans taken while moving the OCT beam laterally, showing the slower dynamics in a 2D plane, see Figure 3.1.

The dynamic redistribution of MD12 was measured by taking 1D (often referred to as A-scans in the OCT literature) scans near the apex of the droplets. Since interfaces that are perpendicular to the beam, i.e., the air-liquid interface at the droplets' apex, result in a high scattering intensity that can overload the sensor, we used a slight lateral offset to avoid overexposure. Using Fourier domain OCT, all sampling volumes in a single 1D scan, over the full depth of a droplet, were measured simultaneously, with the dimensions of the sampling volumes of $6.7\ \mu\text{m} \times 6.7\ \mu\text{m} \times 2.6\ \mu\text{m}$ being dictated by the optical resolution in the lateral (x and y) and axial (z) direction. We note that the axial resolution is highest at the focus point and decreases slightly with increasing distance from the focus point. In all of our experiments, the axial sampling resolution was $1.95\ \mu\text{m}$, as this resolution is set by the spectral resolution of the OCT system. Temporal fluctuations arising from the scattering of light from TiO_2 particles moving through the individual sampling volumes were measured by taking 10 000 consecutive A-scans at a single lateral location at a rate of 5.5 kHz for a total scan time of 1.82 s. From the resulting sequence of 1D scans (often referred to as an M-scan), the diffusion coefficient of the TiO_2 particles was determined, which in turn was converted to the concentration of MD12, as explained later. Consecutive M-scans were taken at intervals of 3.65 s (0.27 Hz) during the drying period of 240 s. Hereafter, we will colloquially refer to M-scans as '1D OCT' scans.

The dynamic changes in the 2D shape of a droplet and the internal flows were measured by taking consecutive A-scans at a fixed x -position, while the Galvano mirror of the OCT system swept the beam across the droplet in the y -direction. 128 scans were taken along a sweep at a frequency of 36 kHz. This resulted in a step size of $6.25\ \mu\text{m}$, which ensured that the lateral resolution in the image was dictated by the optical resolution of $6.7\ \mu\text{m}$. At each y -position, a single 1D scan over the depth direction was made (and not 10 000 consecutive scans as before), as this type of measurement does not aim at resolving the rapid temporal fluctuations inside the measurement volumes. The sequence of 128 1D scans across the droplet was used to construct a 2D scan (often referred to as a B-scan). Consecutive B-scans were taken at a frequency of 1 Hz during a drying period of 240 s. Hereafter, we colloquially refer to consecutive B-scans as '2D OCT' scans.

3.2.5. OCT signal processing - General

The raw interferometric OCT signals were acquired using ThorImage[®] software (Thorlabs Inc.) and post-processed with MATLAB (2017b). The processing consisted of the following steps. First, a reference

spectrum was subtracted from the signal. Second, the resulting interference spectrum was interpolated in order to linearize the spectrum in wavenumber (because the raw interference spectrum depends on space on the spectrometer). The interpolation is essential to obtain bandwidth-limited axial resolution. Third, an inverse Fourier transform was applied to convert the signal from the spectral to the space-time domain (Izatt et al., 2015). Fourth, the absolute value was taken to obtain the final depth-resolved OCT amplitude $|a(i, j, k)|$, where the index i refers to the discretized spatial z -location along the depth of the droplets, j refers to the discretized y -location, and k to the discretized time. The index i covers 1024 pixels and spans 1.89 mm. The droplet occupied roughly 300 of these pixels in depth at the start of the drying experiment. A higher magnification was not possible as the axial range is determined by the spectrometer in the OCT system. The ranges for $j = 1 \dots J$ and $k = 1 \dots K$ depend on whether a fast 1D scan or a slower 2D scan was acquired, as detailed below.

3.2.6. OCT signal processing - Determination of the spatio-temporal diffusion coefficient of the TiO_2 particles

The first type of OCT measurement was done to resolve the spatio-temporal diffusion coefficient of the TiO_2 particles at a single and fixed lateral position ($J = 1$) along the droplet's center-line. A single sequence of 1D scans comprises $K = 10\,000$ consecutive scans, such that k runs from 1 to 10 000. The temporal autocorrelation, $\alpha(i, j, k)$, was calculated for each sampling volume along the depth, i.e. for each i . Since there is a single y -position, we drop the index j and write

$$\alpha(i, l) = \begin{cases} \frac{1}{K-l} \sum_{k=1}^{K-l} (|a(i, k)| - \langle |a(i)| \rangle) (|a(i, k+l)| - \langle |a(i)| \rangle), & \text{if } l \geq 0 \\ \frac{1}{K-|l|} \sum_{k=1+|l|}^K (|a(i, k)| - \langle |a(i)| \rangle) (|a(i, k-|l|)| - \langle |a(i)| \rangle), & \text{if } l < 0 \end{cases}$$

with l the discretized lag index running from $-K + 1$ to $K - 1$ and $\langle |a(i)| \rangle$ the mean amplitude. The temporal autocorrelation for each sampling volume provides insights on the time scale of the fluctuations in scattering intensity indicative for the local diffusion coefficient of the TiO_2 particles, which depends on the local viscosity of the MD12 solution, and hence on the local MD12 concentration. The local diffusion coefficient was determined with two assumptions. First, assuming monodisperse particles, the decay of $\alpha(i, l)$ can be described by a single exponential decay. Second, assuming that particle diffusion causes the temporal decay, the field decorrelates at a rate of Dq^2 , with diffusion coefficient D and the magnitude of the scattering vector q . This magnitude is calculated using $q = 4\pi n \sin(\theta/2)/\lambda$, with the scattering wavelength in vacuum λ , the refractive index of the medium n , and the scattering angle θ , which is 180° in OCT. We used the central wavelength $\lambda_c = 900\text{ nm}$ as the scattering wavelength, as confirmed in previous work (Kalkman et al., 2010). Since we defined the OCT signal as the absolute value and the OCT magnitude is the product of two heterodyne intensities, the measured signal decorrelates at a rate of $2Dq^2$ (Kalkman et al., 2010). With these assumptions, the diffusion coefficient of the TiO_2 particles in each sampling volume, $D(i)$, can be determined by fitting $g(i, l) = A(i)e^{-2D(i)q^2|l|/f}$ to $\alpha(i, l)$, with $A(i)$ an amplitude fitting parameter, $D(i)$ the fitted diffusion coefficient, and f the acquisition frequency of 5.5 kHz. Fitting was done using `nlinfit` (MATLAB2017b). Only the data where α had not reached zero yet was used to fit $g(i, l)$. While the value of $A(i)$ at $l = 0$ equals 1 after normalization, we saw an immediate drop in amplitude due to shot noise and ignored $l = 0$ when fitting $A(i)$. We found that fits with $A(i)$ larger than 0.3 were accurate, i.e., with the initial decay visible above the noise levels. Fits with lower values of $A(i)$ were excluded from further analysis. The depth-resolved diffusion coefficients obtained from the fits were converted from discretized positions to z -positions by multiplying i with the axial sampling resolution ($1.95\ \mu\text{m}$) and accounting for the refractive index. The $D(z)$ along the center-line was determined for each 1D sequence, while the 1D sequences were taken at 0.27 Hz to obtain the time-dependence. Hence, a spatio-temporal map of $D(z, t)$ was obtained. The influence of noise was reduced by applying a median filter (5×5) in space and time for the $D(z, t)$ map. The value of a data point was replaced with the median value of its neighbors in case its value deviated more than a factor 4 from the median value.

We conclude by pointing out that the acquisition range of $D(z, t)$ depends on the sampling frequency (5.5 kHz) and the number of successive scans (10 000) in a single sequence. The sampling frequency limits detection of short time scale fluctuations. We estimate, based on half of the decay occurring in the first ten scans, an upper limit of $D \approx 1.1 \times 10^{-12} \text{ m}^2 \text{ s}^{-1}$. For a given frequency, the number of scans in a

sequence limits detection of longer time scale fluctuations. Assuming that half the decay occurs over 10 000 scans, we estimate a lower limit of $D \approx 5.5 \times 10^{-16} \text{ m}^2 \text{ s}^{-1}$. The settings used in the experiments were chosen based on the expected dynamic range of TiO_2 diffusion coefficients in the drying droplets.

3.2.7. Testing of the diffusion coefficient determination method

The accuracy of the diffusion coefficient determination method was tested using an aqueous 2.5 wt% solution of monodisperse polystyrene particles (Polysciences, Inc.) with a reported diameter of $d = 104 \pm 6 \text{ nm}$. This size was confirmed by measuring a diluted sample (0.26 wt%) with dynamic light scattering (Malvern Zetasizer Nano ZS), resulting in $d = 107 \pm 2 \text{ nm}$. The accuracy test was done by dispensing several milliliters of the solution in a cuvette. The cuvette was sealed with a transparent cover to prevent evaporation and corresponding convective flows. The fitted $D(z)$ from 100 consecutive axial depths in the liquid was averaged and resulted in $\hat{D} = 5 \pm 1 \mu\text{m}^2 \text{ s}^{-1}$. The Stokes-Einstein equation was used to calculate the theoretical D of the polystyrene particles using the reported diameter as $D = 4.13 \pm 0.08 \mu\text{m}^2 \text{ s}^{-1}$. Hence, there was a good agreement between the D obtained with OCT and the theoretical D . The observed precision is acceptable for the purpose of the droplet drying measurements, because the diffusion coefficient in the droplet drying experiments is expected to change over several orders of magnitude. We repeated the cuvette measurements on two different occasions using the TiO_2 tracer particles in 10 wt% MD12 solution, resulting in $\hat{D} = 0.4 \pm 0.2 \mu\text{m}^2 \text{ s}^{-1}$ and $\hat{D} = 0.4 \pm 0.2 \mu\text{m}^2 \text{ s}^{-1}$, showing a good reproducibility.

3.2.8. Determination of the spatio-temporal viscosity and concentration of the MD12 solution

The obtained diffusion coefficient $D(z, t)$ provides insights on the viscosity $\eta(z, t)$, and hence on the MD12 concentration $c(z, t)$. We used the Stokes-Einstein equation to determine the viscosity using $\eta(z, t) = k_B T / 3\pi D(z, t) d$, with $k_B T$ the thermal energy and d the diameter of the TiO_2 particles, which was determined before each experiment using the sealed cuvette method as described in the previous section. The MD12 concentration $c(z, t)$ was determined from Equation 5 in the work by Both et al. (2019) on aqueous MD12 solutions. We used the fitting parameters found by the authors for calculating $c(z, t)$ from $\eta(z, t)$. Since our work used the same maltodextrin batches as the work of Both et al. (2019), we can use their fitted parameters for this calculation without introducing errors due to batch differences.

3.2.9. OCT signal processing - Droplet drying kinetics and internal flow

The 2D OCT measurements were done to (i) determine the dynamic changes in the 2D shape of the droplets, (ii) detect the formation of a concentrated skin, and (iii) capture the internal flows. Unlike the 1D scan, the 2D scan does not comprise temporal information ($K = 1$), but it does comprise 1D scans at 128 y -positions ($J = 128$). Hence, a single sequence $|a(i, j, k = 1)|$ shows the (quasi-)instantaneous amplitude in the 2D cross section of the droplet. This sequence is repeated at 1 Hz to capture the dynamic changes during the drying period of 240 s.

The 2D shape of the droplets and the substrate location can be obtained from the OCT intensity. A circle fitting algorithm was used to fit a circle to the detected droplet interface for calculating the height $h(t)$ and the radius $R(t)$ of the droplet as a function of time. From these parameters, the equivalent spherical diameter $d(t)$ was calculated using the geometrical relation for a spherical cap. Since we observed that the hollow particle that formed has the shape of a spherical cap, we used the spherical-cap description throughout the drying process.

The internal flow inside the droplet was determined by analyzing subsequent 2D OCT images using a particle image velocimetry algorithm implemented in DaVis software (LaVision, Germany). The onset of skin formation and the thickness of this skin were analyzed using the variance in intensity, further explained in the results section.

3.3. Results and Discussion

3.3.1. Drying kinetics from 2D OCT images

Before we discuss the kinetics of the droplet drying process, we first discuss the general features visible in the 2D OCT images of a drying droplet. The first panel in Figure 3.2a shows the 2D cross section of a sessile droplet shortly after the start of the drying experiment. The droplet is visible as a bright speckled area arising from the scattering of light from tracers against a dark background of the surrounding air where no backscattering takes place. The surface of the flat substrate is visible as the bright horizontal line from specularly reflected light, extending left and right from the droplet, which is best visible in the other three panels where the droplet has shrunk. The panels show that the droplet appears to extend into the flat substrate. While a similar observation is seen in brightfield microscopy images taken from the side of sessile droplets (Both et al., 2018), the explanation for this observation is different. In brightfield images, it is a reflection that itself does not contain information. In the OCT images, extension into the substrate is caused by a difference between the length of the path traveled through the air (physical path) and through the liquid droplet (optical path). We note that the substrate, which appears curved beneath the droplet, is hardly visible due to substantial multiple scattering. For the construction of the 2D OCT images, we used the physical path length, with a spacing between pixels in the z -direction of $1.84 \mu\text{m}$. The optical path length is a factor 1.33 longer, which stems from the ratio of the refractive indices of liquid and air. The flat substrate is displayed at the correct height outside the droplet, but it appears lower inside the droplet due to the longer optical path (Edwards et al., 2018; Manukyan et al., 2013). The air-liquid interface is displayed at the correct location. Hence, we can use the 2D OCT images to analyze how the shape of the droplet evolves in time. Only close to the substrate, the interface cannot be resolved for droplets at hydrophobic substrates (contact angle over 90°), as the beam is strongly deflected at the edges of the droplet (Manukyan et al., 2013).

Besides the external shape of the droplet, OCT images have the great advantage of also showing the internal structures of the droplet. The fourth panel, measured at 250 s, shows a dark area inside the droplet that has the same brightness as the background. The absence of scattering particles and what looks like the substrate being slightly visible at approximately the same height as outside the droplet, indicates that a gaseous vacuole has formed. The morphology of the fully dried droplet under the used conditions is a hollow spherical cap. Since the final morphology depends on the redistribution of solute and hence on the drying conditions, other morphologies have also been reported in literature for MD12 solutions (Both et al., 2018; Bylaitė et al., 2001; Siemons et al., 2020).

We quantified the drying kinetics of the droplet by analyzing the dynamic change in the external shape of the droplet, see supplementary video 1 for a video of the 2D OCT images. The theory for drying droplets without solute predicts that the diameter of a spherical droplet decreases with the square root of time (Jakubczyk et al., 2012). Hence, we expect the square of the droplet diameter to linearly decrease in time until the accumulation of MD12 at the air-liquid interface starts to hinder the evaporation process. We fitted a circle to the shape of the droplet in each of the consecutive 2D OCT images using the routine explained before and plotted the normalized square of the diameter ($d^2(t)/d^2(0)$) as a function of time. Initially, the d^2 indeed decreases linearly in time, which is seen in Figure 3.2b. The initial drying rate, κ , found by fitting the measured d^2 in the first 20 s against the relation $d^2 = d_0^2 - \kappa t$ with $d_0 = 432 \mu\text{m}$, is equal to $\kappa = 8.8 \times 10^2 \mu\text{m}^2 \text{s}^{-1}$. Based on this initial rate, full evaporation of the droplet is expected to take 213 s. After the first regime with drying at a constant rate, a second regime is visible in which drying occurs at a decreasing rate. The transition between the two regimes occurs around 60 s, observed as a deviation of the data from the linear fit, see Figure 3.2b. After about 160 s, a third regime is visible, referred to as the locking phase, in which the shape remains constant indicative for reaching a critical surface concentration (Mezhericher et al., 2012). At the transition between the second and third regime, known as the locking point, invagination of the droplet surface starts near the droplet's apex, eventually forming a vacuole inside the droplet. Surface invagination close to the apex has been reported in previous work and can be attributed to inhomogeneous evaporation (Bansal et al., 2015; Bouman et al., 2016). The onset of the invagination can be seen in the third panel (190 s) of Figure 3.2a as a concave deformation of the interface. With OCT, it is easily confirmed that the forming vacuole contains gas, as the extension effect due to a difference in refractive index is suppressed in the region of the vacuole, there is no observable

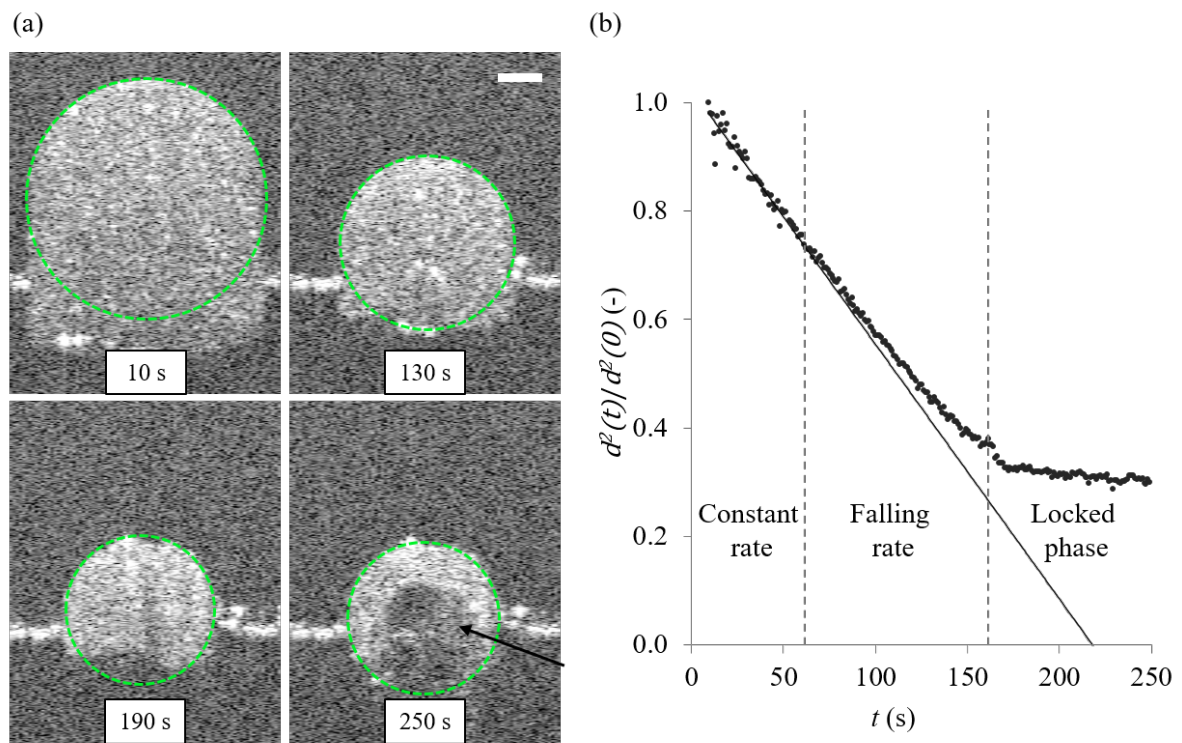


Figure 3.2: Drying kinetics. a) Selected images from the 2D OCT-scans at 10 s, 130 s, 190 s and 250 s of evaporation. Brighter pixels correspond to greater scattering intensity. The scale-bar is $100 \mu\text{m}$. The green circles indicate the fitting result. The black arrow indicates the vacuole. b) Droplet drying kinetics from the application of the circle fitting algorithm to the 2D scans. With d being the equivalent spherical diameter. The two dashed lines indicate the regime transitions as analyzed from the drying curve. A linear trend-line is fitted through the initial 20 s for comparison of the measured drying curve with the constant drying rate curve.

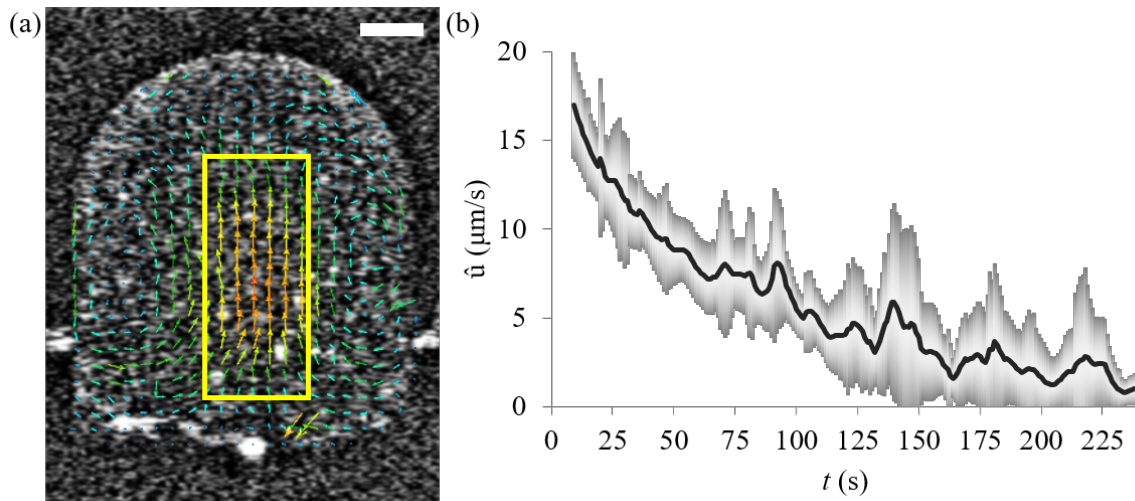


Figure 3.3: Convective flow characterization. The scale-bar is $100\ \mu\text{m}$. a) Velocity vector field at $t = 9\ \text{s}$, as obtained from the particle image velocimetry analysis. Blue indicates a low velocity and orange indicates a high velocity. The yellow box indicates the region from which the mean upward velocity \hat{u} was determined. b) Mean upward velocity \hat{u} during droplet drying. The gray bars show the standard deviation.

scattering and the location of the planar substrate is at the same height as the location of the substrate outside the droplet (Figure 3.2a - 250 s). While OCT, like brightfield imaging, allows determining the drying curve, including the transitions between the three regimes, it also allows studying the formation of the skin and determining the spatio-temporal viscosity and MD12 concentration, as detailed later.

3.3.2. Internal flow from 2D OCT images

The 2D OCT images can also be used to get an impression of the internal flow, with the TiO_2 agglomerates acting as tracer particles. The scattering of the individual agglomerates was sufficient to allow performing particle image velocimetry on the 2D OCT images. Hence, we analyzed the 2D OCT images to get an estimation of the magnitude of the internal flow along the center-line of the droplet. This information is essential to confidently quantify the contribution of convection when later analyzing the fast 1D OCT scans to resolve the spatio-temporal diffusion coefficient of the TiO_2 particles, as well as the viscosity and the MD12 concentration along the center-line of the droplet.

A recirculation flow pattern was observed in the droplet, with an upward flow in the center and a downward flow along the interface, see Figure 3.3a. Other work has shown that this pattern is characteristic for droplets on hydrophobic substrates and caused by inhomogeneous evaporation that results in thermocapillary driven flows, also known as Marangoni flows (Edwards et al., 2018; Manukyan et al., 2013) The largest velocities were found in the central region, which is where the 1D OCT scans were performed. The average velocity \hat{u} in the central region indicated by the yellow rectangle is about $20\ \mu\text{m s}^{-1}$ at the start of drying, see Figure 3.3b. This velocity gradually decreases, which is explained by the increasing viscosity of the droplet as evaporation proceeds.

3.3.3. Skin formation from 2D OCT images

The 2D OCT images were also used to study the formation of a solid skin at the droplets interface. The temporal fluctuations in brightness in subsequent 2D images contain information about the dynamics. Rapid fluctuations correspond to liquid regions, while slower fluctuations correspond to highly viscous or solid regions. We started the analysis by removing the background of the raw 2D OCT images presented in Figure 3.2a, see the result in Figure 3.4a. We then analyzed the temporal variation in the intensity of each pixel for a moving time window of 3 subsequent images, which we found to be optimal for identifying skin and bulk after testing a range of 2-11 subsequent images. The values of the variance σ^2 are presented

in the panels in Figure 3.4b, with a higher brightness corresponding to a higher variance. In the first two panels, the brightness is uniform across the droplet. The last two panels show a darkened area near the interface with less fluctuations that is indicative of a solidifying skin.

We quantified the dynamics of skin formation as follows: for each image, we determined the center of the circle that describes the interface. Then, while ignoring all pixels below that center, we analyzed the variance as a function of the distance from the center $\sigma^2(r)$. The transition from liquid to solid is gradual, which results in a gradual decrease of $\sigma^2(r)$ with increasing r . We fitted the profile $\sigma^2(r)$ with an arbitrary exponential function $p(r) = \sigma_{min}^2 + (\sigma_{max}^2 - \sigma_{min}^2) \cdot e^{(-1.2r^{-b})}$ with σ_{min}^2 and σ_{max}^2 the minimum and maximum variance along the radius, respectively. The factor 1.2 in the exponent was manually determined to match the curve of $p(r)$ with the gradual decrease of the variance at the transition point. The location r_{skin} along the line where the variance was halfway its minimum and maximum value, i.e. $e^{(-1.2r_{skin}^{-b})} = 0.5$, was taken as the transition between solid and liquid. For each image, we determined the skin thickness, $\delta = R - r_{skin}$, with $R(t)$ the fitted droplet radius. By analyzing consecutive images, we determined how the skin thickness increases in time $\delta(t)$. We divided the obtained thickness by the refractive index of water to correct for the optical extension in the OCT images.

Figure 3.4c show the dynamics of the skin thickness $\delta(t)$. Skin formation starts about 15 s before locking of the droplet. At the start of the third regime, the skin grew to a thickness of $20 \pm 3 \mu\text{m}$. The skin reaches a maximum of $87 \pm 2 \mu\text{m}$ at 217 s. Interestingly, $\delta(t)$ decreases to about $40 \mu\text{m}$ as the end of drying approaches. From supplementary video 2, which shows the variance images, this effect looks to be caused by the moving front of the vacuole, which appears to compress the stagnant skin region. Comparing the measured skin thickness to the thickness estimated based on the total solids content provides a clue about how dry the stagnant layer is. With an initial droplet volume of $4.2 \times 10^{-11} \text{m}^3$ and an initial concentration of 10 wt%, the total solids contents is $5.1 \mu\text{g}$. Assuming the skin to be fully dry and amorphous, the volume of the skin follows from the total solids contents and the density of dry amorphous maltodextrin ($1.1\text{-}1.4 \text{g mL}^{-1}$ (Takeiti et al., 2010)). With an outer radius of $141 \mu\text{m}$ at 250 s, we estimate the thickness of the skin to be about $20 \mu\text{m}$. The measured skin thickness is about $40 \mu\text{m}$, showing that the stagnant layer observed in the measurements is not fully dry.

3.3.4. Measuring the dynamic intra-droplet solute redistribution

Spatio-temporal diffusion coefficient of TiO_2 particles

We now turn to the main point of the paper, which is to explore the use of OCT to determine the spatio-temporal redistribution of solute in a drying droplet. This redistribution of solute was measured using the fast 1D OCT data obtained along the center-line of the droplet. A map of the diffusion coefficient, $D(z, t)$, is shown in Figure 3.5a. Initially, the diffusion coefficient is uniform across the height of the droplet, which is consistent with a uniform distribution of TiO_2 , and averages to $D = 2.9 \times 10^{-13} \text{m}^2 \text{s}^{-1}$. Over time, the diffusion coefficient in the region near the interface decreases, seen from the change from yellow to purple. Additionally, the region at the interface with a reduced diffusion coefficient widens over time. Further inspection of the autocorrelation curves in the low D region near the interface showed that the lowest measurable diffusion coefficient was $D \approx 5.3 \times 10^{-15} \text{m}^2 \text{s}^{-1}$, which is larger than the estimated lower detection limit of $D \approx 5.5 \times 10^{-16} \text{m}^2 \text{s}^{-1}$. For values of D below the measurable ones, the amplitude of the autocorrelation function was too low ($A < 0.3$) to perform a faithful fit. The reason for why the estimated lower detection limit was not reached is not clear, although, we expect that over the timescale of the entire M-scan accumulation of noise leads to a reduced signal quality. When reaching $t = 195 \text{s}$, the measured height becomes zero, and only the bright line of the PDMS substrate remained on the OCT scan. Visual observation post factum showed that a vacuole had formed inside the droplet, similar to what was seen in Figure 3.2a, but, the hole in the shell that lead to the vacuole formed at the droplet's apex. Hence, the OCT bundle went through the hole hitting the PDMS substrate without hitting parts of the partially-dried droplet. We can identify this time where the measured height goes to zero as the transition to the third drying regime. Since we had no access to the spherical diameter of this droplet, the transition to the second regime was not determined.

A final feature we point out in the map is the growing region of decreasing diffusion coefficient near the

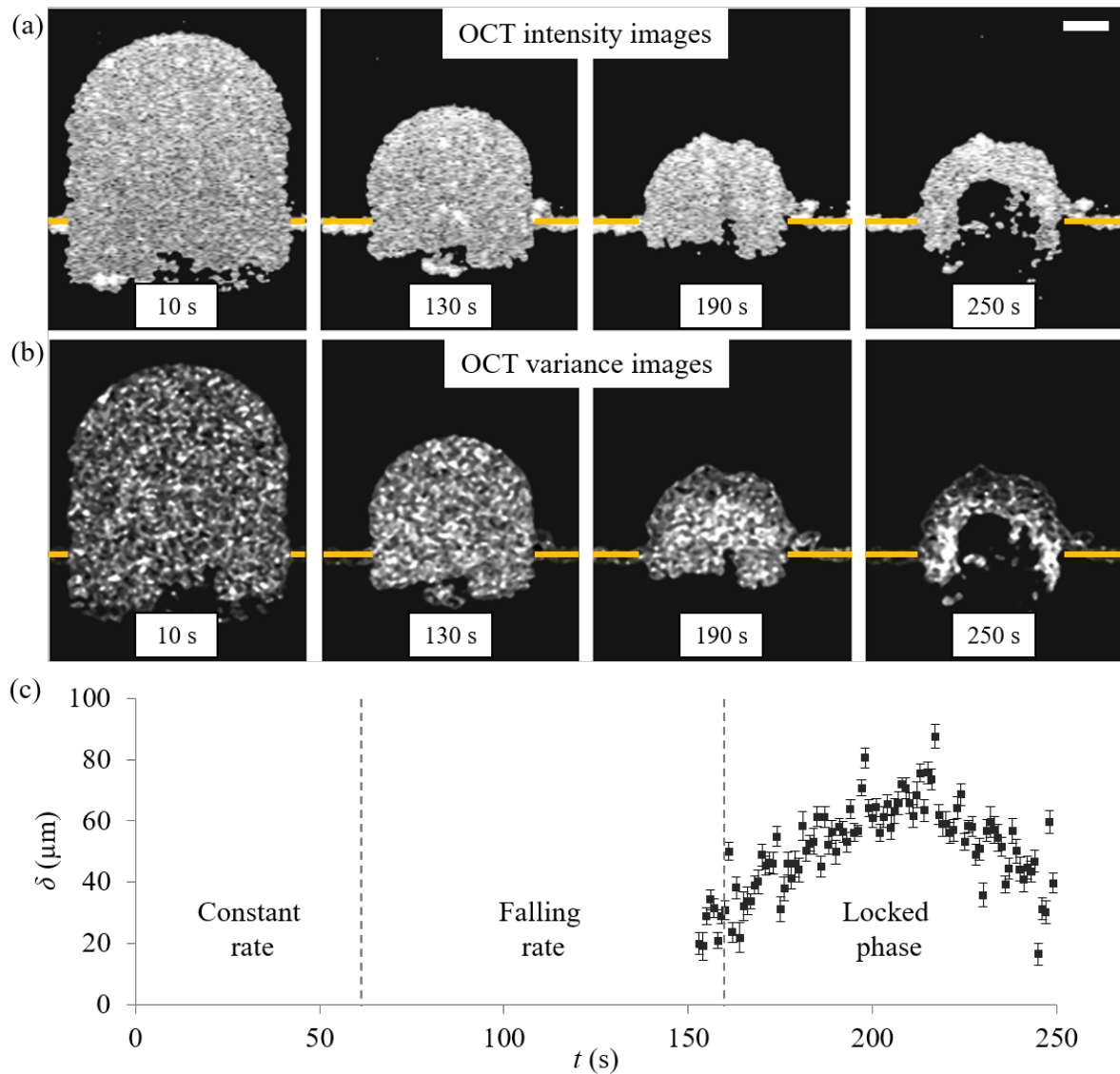


Figure 3.4: Detection of the stagnant skin from the 2D OCT scans. The scale-bar is 100 μm . a) OCT 2D intensity images with the droplet isolated from the background. b) The images constructed from the temporal variance of the OCT intensity. c) The skin thickness $\delta(t)$ as determined from the variance figures in b). The error bars indicate the 95% confidence interval of the fit. The regimes, as found in Figure 3.2, are also indicated in the figure.

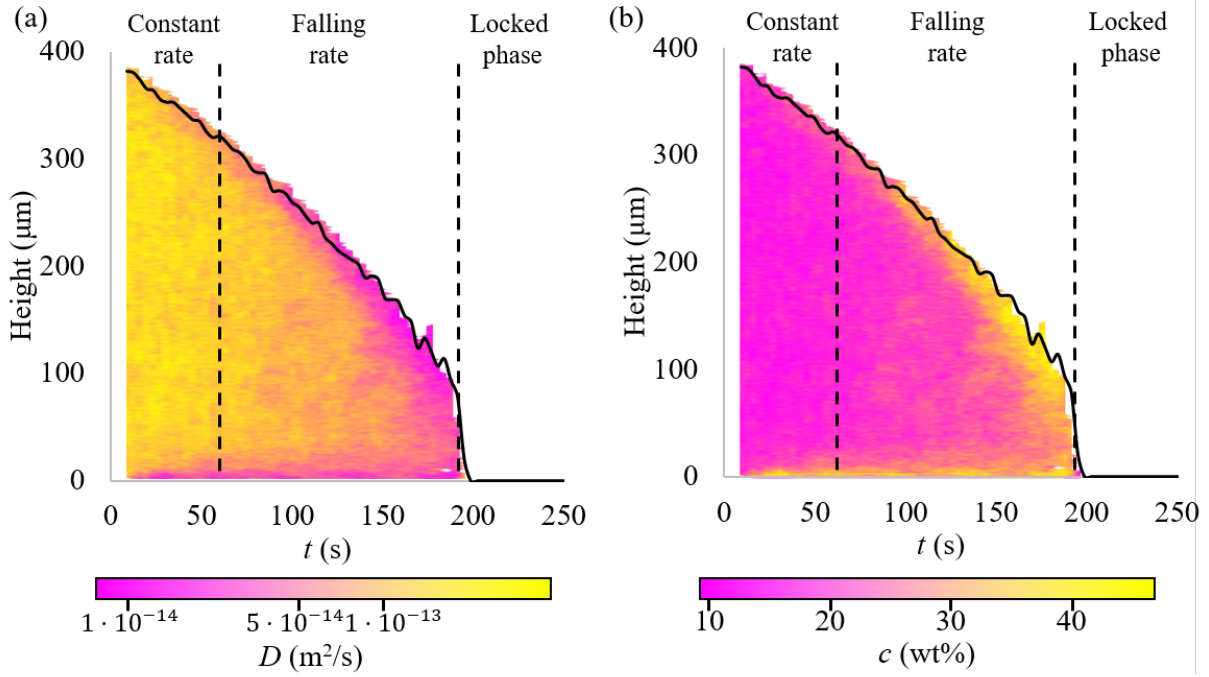


Figure 3.5: Mapping of the intra-droplet properties. a) Local logarithmic diffusion coefficient of the TiO₂ particles. b) Local MD12 concentration. In both figures, the black line indicates the height of the droplet, as determines from the 1D OCT scans. The dashed lines indicate the transition between the different drying regimes.

substrate. The diffusion coefficient in this region differs at least one order of magnitude from the diffusion coefficient in the core of the droplet. Figure 3.5a shows that this region grows to a thickness of about 10 μm in the first 100 s. The decreased diffusion coefficient indicates that MD12 accumulates near the substrate, which may be attributed to the internal recirculations (Bansal et al., 2015; Bansal et al., 2018) as observed in the particle image velocimetry analysis of the 2D OCT scans.

Contribution of convective flow to measurement of $D(z, t)$

The autocorrelation of the 1D OCT scans used to determine the spatio-temporal diffusion coefficient of the TiO₂ particles is affected by diffusion and convection of those particles. We neglected the convective contribution in our quantitative analysis. Here, we justify that. The contribution to the autocorrelation of the 1D OCT scans by convective flow is described by $e^{-2[\frac{u_z l}{w_z}]^2}$, with l the discretized lag time, f the acquisition frequency, u_z the velocity in the direction of the beam, and w_z the beam radius in the axial direction. For Fourier-domain OCT, the axial beam radius is approximately equal to the coherence length of 2.6 μm (Weiss et al., 2015). The contribution by diffusion is described by $e^{-2Dq^2 l/f}$. The two contributions are multiplicative in the autocorrelation function, such that the contribution by convection can be neglected with respect to the contribution by diffusion when $[(f w_z^2)/(l u_z^2)]/(D q^2)^{-1} \gg 1$. Using the values for u_z and D at the start of drying, i.e. $v_z \approx 20 \mu\text{m s}^{-1}$ and $D \approx 3 \times 10^{-13} \text{ m}^2 \text{ s}^{-1}$, together with a lag time of $l/f = 18/5500 \text{ s}$ as estimated from $e^{-2Dq^2 l/f} \approx 0.5$, we find that this criterion is met by two orders of magnitude. During drying, the convective flow velocity lessens in the bulk region and becomes negligible in the skin region. Considering a drying time of $t \approx 140 \text{ s}$, at which we take a conservative velocity of $u_z = 10 \mu\text{m s}^{-1}$, a diffusion coefficient in the bulk region of $D \approx 6 \times 10^{-14} \text{ m}^2 \text{ s}^{-1}$, and a lag time of $l/f = 93/5500 \text{ s}$ for $e^{-2Dq^2 l/f} \approx 0.5$, we find, again, that the criterion is met by two orders of magnitude. While we considered the axial velocity in this analysis, the lateral velocity also influences the correlation, however, it is significantly lower than the axial velocity as evident from Figure 3.3 and its contribution can be safely neglected. Hence, the contribution of both axial and lateral convection to the decay of the autocorrelation function can be confidently neglected under the here-tested conditions.

Spatio-temporal viscosity and concentration of MD12 solution

We determined the spatio-temporal viscosity $\eta(z, t)$ and, subsequently, the MD12 concentration $c(z, t)$ based on the spatio-temporal diffusion coefficient of the TiO_2 particles as explained in Section 3.2.8. The features in the MD12 concentration map are similar to the features in the map of the diffusion coefficient of the TiO_2 particles. The concentration map is shown in Figure 3.5b. The initial concentration averaged over the depth of the droplet is 14 ± 2 wt%, slightly larger than the 10 wt% of the prepared MD12 solution, partly explained by the first OCT scan being taken about 10 s after dispensing the droplet. Another explanation is the lower accuracy for the concentration measurement at lower concentrations, as the $\eta(c)$ curve remains comparatively flat for low concentrations (< 30 wt%) and strongly increases for higher concentrations (Both et al., 2019). Hence, a relatively small measurement error would have a greater effect on the resulting concentration at lower concentrations. At $t = 60$ s, which is when the droplet in the 2D OCT scan transitioned to the second drying regime, the bulk concentration was 15 ± 2 wt%, while the concentration near the air-liquid interface increased to 23 ± 3 wt%. From then onward, the concentration near the interface further increased to the maximum measurable concentration of 46 wt%. Around the transition to the third drying regime, the bulk concentration had also noticeably increased to values over > 30 wt%. Based on this it is unclear whether the transition to the third drying regime is due to reaching a critical surface concentration (≈ 46 wt%), or, because the bulk concentration became elevated.

It is worthwhile to compare the measured $c(z, t)$ map to typical results from numerical approaches that determine the spatio-temporal concentration of solute in an evaporating droplet. Numerical approaches commonly show an exponential shape of the radial solute concentration, where the surface layer has a highly elevated concentration compared to the center of the droplet. This exponential shape is maintained until the surface layer reaches a critical condition, which is, typically, when the surface layer solidifies (Porowska et al., 2016). The measured $c(z, t)$ map also shows a sharp increase of concentration from the bulk to the interface, but from about 100 s onward, the concentration appears to plateau at concentrations between 40 wt% and 46 wt%. However, the viscosity at $c \approx 46$ wt% is only $\eta \approx 0.1$ Pa s, while viscosity measurements have shown that MD12 remains liquid-like up to concentrations of ≈ 70 wt% (Both et al., 2019). Hence, we expect the concentration to exceed the highest measurable value of 46 wt%. While further experimental research is needed to resolve the higher concentrations at the interface, we do demonstrate that OCT can quantitatively measure the concentration of solutes dynamically in time inside a drying droplet.

The use of OCT for other materials, especially those with increased complexity such as milk powders, is of interest. In this work, we used a binary system (maltodextrin in water) for which the relation between the viscosity and maltodextrin concentration is known, making it possible to determine the spatio-temporal maltodextrin concentration from the spatio-temporal viscosity. This is also possible for multi-component systems for which a combination of concentrations of the various components uniquely relates to the viscosity of the mixture. Care should be taken when dealing with multi-component mixtures in which components unmix during evaporation (Both et al., 2018). While it may be difficult to determine the individual spatio-temporal concentrations in such systems, the spatio-temporal viscosity can be measured and used for optimization or validation purposes.

3.4. Conclusion

The goal of this work was to explore the use of optical coherence tomography to study drying of turbid solute-containing droplets, with the emphasis on measuring the dynamic redistribution of solute during drying. Using aqueous droplets containing maltodextrin as a model system, we demonstrated that OCT can be used to measure the drying kinetics, the internal flows, and the development of internal structures inside drying droplets, such as the solidifying skin on the air-liquid interface and the growth of a gaseous vacuole. Moreover, we demonstrated that spatio-temporal maltodextrin concentration maps can be obtained over the center-line of a sessile droplet, providing an advantage over conventional single droplet drying methods. We think that the ability to measure the dynamic redistribution of solutes and linking it to the development of the morphology of dried particles is instrumental for the rational design of powders with specific properties and for the optimization of process equipment such as spray dryers. Additionally, we think that the ability to measure the spatio-temporal concentrations is important for the validation of numerical models that aim

to predict the morphology or drying droplets and their agglomeration behavior from the development of spatio-temporal concentrations during drying. While the here presented experimental method focuses on sessile droplets that are larger than droplets typically encountered in spray dryers, we think that mechanistic insights obtained from a quantitative comparison between experiments and numerical models at the scale of sessile droplets guide our mechanistic understanding of drying of smaller droplets relevant for spray drying processes.

Bibliography

- Bansal, L., Miglani, A., & Basu, S. (2015). Universal buckling kinetics in drying nanoparticle-laden droplets on a hydrophobic substrate. *Physical Review E*, *92*(4), 042304. <https://doi.org/10.1103/physreve.92.042304>
- Bansal, L., Sanyal, A., Kabi, P., Pathak, B., & Basu, S. (2018). Engineering interfacial processes at mini-micro-nano scales using sessile droplet architecture. *Langmuir*, *34*(29), 8423–8442. <https://doi.org/10.1021/acs.langmuir.7b04295>
- Both, E. M., Nuzzo, M., Millqvist-Fureby, A., Boom, R. M., & Schutyser, M. A. I. (2018). Morphology development during single droplet drying of mixed component formulations and milk. *Food Research International*, *109*, 448–454. <https://doi.org/10.1016/j.foodres.2018.04.043>
- Both, E. M., Siemons, I., Boom, R. M., & Schutyser, M. A. I. (2019). The role of viscosity in morphology development during single droplet drying. *Food Hydrocolloids*, *94*, 510–518. <https://doi.org/10.1016/j.foodhyd.2019.03.023>
- Bouman, J., Venema, P., de Vries, R. J., van der Linden, E., & Schutyser, M. A. I. (2016). Hole and vacuole formation during drying of sessile whey protein droplets. *Food Research International*, *84*, 128–135. <https://doi.org/10.1016/j.foodres.2016.03.027>
- Bylaitė, E., Venskutonis, P. R., & Maždžierienė, R. (2001). Properties of caraway (*carum carvi* L.) essential oil encapsulated into milk protein-based matrices. *European Food Research and Technology*, *212*(6), 661–670. <https://doi.org/10.1007/s002170100297>
- Callewaert, T., Dik, J., & Kalkman, J. (2017). Segmentation of thin corrugated layers in high-resolution OCT images. *Optics Express*, *25*(26), 32816–32828. <https://doi.org/10.1364/oe.25.032816>
- Davidson, Z. S., Huang, Y., Gross, A., Martinez, A., Still, T., Zhou, C., Collings, P. J., Kamien, R. D., & Yodh, A. G. (2017). Deposition and drying dynamics of liquid crystal droplets. *Nature Communications*, *8*(1), 1–7. <https://doi.org/10.1038/ncomms15642>
- de Souza Lima, R., Ré, M.-I., & Arlabosse, P. (2020). Drying droplet as a template for solid formation: A review. *Powder Technology*, *359*, 161–171. <https://doi.org/10.1016/j.powtec.2019.09.052>
- Edwards, A. M. J., Atkinson, P. S., Cheung, C. S., Liang, H., Fairhurst, D. J., & Ouali, F. F. (2018). Density-driven flows in evaporating binary liquid droplets. *Physical Review Letters*, *121*(18), 184501. <https://doi.org/10.1103/physrevlett.121.184501>
- Foerster, M., Gengenbach, T., Woo, M. W., & Selomulya, C. (2016). The influence of the chemical surface composition on the drying process of milk droplets. *Advanced Powder Technology*, *27*(6), 2324–2334. <https://doi.org/10.1016/j.apt.2016.07.004>
- Fu, N., Woo, M. W., & Chen, X. D. (2012). Single droplet drying technique to study drying kinetics measurement and particle functionality: A review. *Drying Technology*, *30*(15), 1771–1785. <https://doi.org/10.1080/07373937.2012.708002>
- Griffith, J. D., Bayly, A. E., & Johns, M. L. (2008). Magnetic resonance studies of detergent drop drying. *Chemical Engineering Science*, *63*(13), 3449–3456. <https://doi.org/10.1016/j.ces.2008.03.043>
- Izatt, J. A., Choma, M. A., & Dhalla, A.-h. (2015). *Optical Coherence Tomography*. Springer, Berlin, Heidelberg. https://doi.org/https://doi.org/10.1007/978-3-540-77550-8_2
- Jakubczyk, D., Kolwas, M., Derkachov, G., Kolwas, K., & Zientara, M. (2012). Evaporation of microdroplets: The "radius-square-law" revisited. *Acta Physica Polonica-Series A General Physics*, *122*(4), 709. <https://doi.org/10.12693/aphyspola.122.709>
- Kalkman, J., Sprik, R., & van Leeuwen, T. G. (2010). Path-length-resolved diffusive particle dynamics in spectral-domain optical coherence tomography. *Physical Review Letters*, *105*(19), 198302. <https://doi.org/10.1103/physrevlett.105.198302>

- Koponen, A. I., & Haavisto, S. (2020). Analysis of industry-related flows by optical coherence tomography a review. *KONA Powder and Particle Journal*, 2020003. <https://doi.org/10.14356/kona.2020003>
- Lee, J., Bathany, C., Ahn, Y., Takayama, S., & Jung, W. (2016). Volumetric monitoring of aqueous two phase system droplets using time-lapse optical coherence tomography. *Laser Physics Letters*, 13(2), 025606. <https://doi.org/10.1088/1612-2011/13/2/025606>
- Lemoine, F., & Castanet, G. (2013). Temperature and chemical composition of droplets by optical measurement techniques: A state-of-the-art review. *Experiments in Fluids*, 54(7), 1–34. <https://doi.org/10.1007/s00348-013-1572-9>
- Manukyan, S., Sauer, H. M., Roisman, I. V., Baldwin, K. A., Fairhurst, D. J., Liang, H., Venzmer, J., & Tropea, C. (2013). Imaging internal flows in a drying sessile polymer dispersion drop using spectral radar optical coherence tomography (sr-oct). *Journal of Colloid and Interface Science*, 395, 287–293. <https://doi.org/10.1016/j.jcis.2012.11.037>
- Meerdink, G., & van't Riet, K. (1995). Modeling segregation of solute material during drying of liquid foods. *AIChE Journal*, 41(3), 732–736. <https://doi.org/10.1002/aic.690410331>
- Mezhericher, M., Levy, A., & Borde, I. J. D. T. (2010). Theoretical models of single droplet drying kinetics: A review. *Drying Technology*, 28(2), 278–293. <https://doi.org/10.1080/07373930903530337>
- Mezhericher, M., Naumann, M., Peglow, M., Levy, A., Tsotsas, E., & Borde, I. (2012). Continuous species transport and population balance models for first drying stage of nanosuspension droplets. *Chemical Engineering Journal*, 210, 120–135. <https://doi.org/10.1016/j.cej.2012.08.038>
- Munoz-Ibanez, M., Nuzzo, M., Turchiuli, C., Bergenstahl, B., Dumoulin, E., & Millqvist-Fureby, A. (2016). The microstructure and component distribution in spray-dried emulsion particles. *Food Structure*, 8, 16–24. <https://doi.org/10.1016/j.foostr.2016.05.001>
- Nuzzo, M., Overgaard, J. S., Bergenstahl, B., & Millqvist-Fureby, A. (2017). The morphology and internal composition of dried particles from whole milk from single droplet to full scale drying. *Food Structure*, 13, 35–44. <https://doi.org/10.1016/j.foostr.2017.02.001>
- Nuzzo, M., Sloth, J., Brandner, B., Bergenstahl, B., & Millqvist-Fureby, A. (2015). Confocal raman microscopy for mapping phase segregation in individually dried particles composed of lactose and macromolecules. *Colloids and Surfaces A: Physicochemical and Engineering Aspects*, 481, 229–236. <https://doi.org/10.1016/j.colsurfa.2015.04.044>
- Porowska, A., Dosta, M., Fries, L., Gianfrancesco, A., Heinrich, S., & Palzer, S. (2016). Predicting the surface composition of a spray-dried particle by modelling component reorganization in a drying droplet. *Chemical Engineering Research and Design*, 110, 131–140. <https://doi.org/10.1016/j.cherd.2016.03.007>
- Quiño, J., Hellwig, T., Griesing, M., Pauer, W., Moritz, H.-U., Will, S., & Braeuer, A. (2015). One-dimensional raman spectroscopy and shadowgraphy for the analysis of the evaporation behavior of acetone/water drops. *International Journal of Heat and Mass Transfer*, 89, 406–413. <https://doi.org/10.1016/j.ijheatmasstransfer.2015.05.053>
- Sadek, C., Schuck, P., Fallourd, Y., Pradeau, N., Le Floch-Fouéré, C., & Jeantet, R. (2015). Drying of a single droplet to investigate process-structure-function relationships: a review. *Dairy Science and Technology*, 95(6), 771–794.
- Santos, D., Mauricio, A. C., Sencadas, V., Santos, J. D., Fernandes, M. H., & Gomes, P. S. (2018). Spray drying: An overview. *Pignatello, R. (Comp.). Biomaterials-Physics and Chemistry-New Edition. InTech. UK*, 9–35. <https://doi.org/10.5772/intechopen.72247>
- Schutysen, M. A. I., Both, E. M., Siemons, I., Vaessen, E. M. J., & Zhang, L. (2019). Gaining insight on spray drying behavior of foods via single droplet drying analyses. *Drying Technology*, 37(5), 525–534.
- Sewalt, E. J. G., Zhang, F., van Steijn, V., van Ommen, J. R., & Meesters, G. M. H. (2020). Static and dynamic stickiness tests to measure particle stickiness. *KONA Powder and Particle Journal*, 2021017. <https://doi.org/10.14356/kona.2021017>
- Siemons, I., Politiek, R. G. A., Boom, R. M., van der Sman, R. G. M., & Schutysen, M. A. I. (2020). Dextrose equivalence of maltodextrins determines particle morphology development during single sessile droplet drying. *Food Research International*, 131, 108988. <https://doi.org/10.1016/j.foodres.2020.108988>

- Srinivasan, V., Pamula, V. K., Rao, K. D., Pollack, M. G., Izatt, J. A., & Fair, R. B. (2003). 3-d imaging of moving droplets for microfluidics using optical coherence tomography, Squaw Valley, California USA, Citeseer. <https://doi.org/10.1.1.575.7151>
- Takeiti, C. Y., Kieckbusch, T. G., & Collares-Queiroz, F. P. (2010). Morphological and physicochemical characterization of commercial maltodextrins with different degrees of dextrose-equivalent. *International Journal of Food Properties*, *13*(2), 411–425. <https://doi.org/10.1080/10942910802181024>
- Tuckermann, R., Puskar, L., Zavabeti, M., Sekine, R., & McNaughton, D. (2009). Chemical analysis of acoustically levitated drops by raman spectroscopy. *Analytical and Bioanalytical Chemistry*, *394*(5), 1433–1441. <https://doi.org/10.1007/s00216-009-2800-2>
- Van Der Kooij, H. M., Fokink, R., Van Der Gucht, J., & Sprakel, J. (2016). Quantitative imaging of heterogeneous dynamics in drying and aging paints. *Scientific Reports*, *6*(1), 1–10. <https://doi.org/10.1038/srep34383>
- van der Hoeven, M. (2008, August 1). *Particle-droplet collisions in spray drying* (Ph.D. Thesis). School of Engineering, The University of Queensland.
- Vehring, R., Foss, W. R., & Lechuga-Ballesteros, D. (2007). Particle formation in spray drying. *Journal of Aerosol Science*, *38*(7), 728–746. <https://doi.org/10.1016/j.jaerosci.2007.04.005>
- Walton, D. E. (2000). The morphology of spray-dried particles a qualitative view. *Drying Technology*, *18*(9), 1943–1986. <https://doi.org/10.1080/07373930008917822>
- Weiss, N., van Leeuwen, T. G., & Kalkman, J. (2015). Simultaneous and localized measurement of diffusion and flow using optical coherence tomography. *Optics Express*, *23*(3), 3448–3459. <https://doi.org/10.1364/oe.23.003448>

4

The influence of drying on the collision outcome of partially-dried droplets and particles using maltodextrin systems

Partial evaporation of solute-containing droplets in spray drying leads to the development of radial concentration gradients that strongly affect the collision outcome when these droplets collide. In spray drying, collisions of partially-dried droplets, or wet particles, with solid particles or other partially-dried droplets can result in agglomeration. The degree of drying strongly correlates with whether agglomeration takes place. Too little drying and the liquid droplet lumps on collision. Too much drying and the dry particle bounces away. Predicting the collision outcome based on drying time and droplet condition has remained challenging due to the difficulty of experimentally controlling both droplet evaporation and the collision variables. In this work, we study how the rate of drying and, in extension, the development of the radial concentration gradient influences the outcome of collisions between dry particles and partially-dried droplets using a common excipient, maltodextrin. Experimental collisions were obtained using a custom particle ejector with collisions in a Weber number range of 10^{-2} to 10^1 . Observed collision outcomes in order of increasing drying time were coalescence, sticking, and bouncing. The transitions between these collision outcomes occurred substantially before reaching the locking point of the droplets, suggesting that collision outcomes for partially-dried maltodextrin droplets depend on viscous effects. The collision outcomes could be categorized based on drying time and the rate of surface accumulation and an empirical relation describing the critical drying time for the greatest likelihood of agglomeration could be established. Further work should test the universality of this relation.

4.1. Introduction

Collisions of partially-dried droplets of amorphous material in spray drying can lead to separation or merging depending on the degree the droplets have dried. Merging can be coalescence or agglomeration, where the agglomeration is a merger where the constituent particles are independently recognizable. Agglomeration is often desired for its beneficial dispersability and flowability (Verdurmen et al., 2004). Successfully forming agglomerates with the desired open porous structures strongly depends on timing the collisions of partially-dried droplets, i.e. the colliding droplet should stick to another partially-dried droplet or a dry particle upon colliding (van der Hoeven, 2008). Currently, the agglomeration of particles in spray drying is controlled through operator experience, as a successful predictive approach is still lacking (Petersen, 2015). For effective control of the agglomeration process, a priori prediction of the collision outcome would be beneficial, for which knowing the properties of the partially-dried droplet as a result of the droplet's drying history is necessary. Such a predictive approach opens the door to an improved design and operation of spray dryers. In this article, we explore how drying time and droplet conditions can be used to form a predictive approach based on experimental collisions of partially-dried droplets and solid particles, using maltodextrins.

Spray dryers are large chambers with billions of droplets, turbulent airflow and droplet velocities that can reach 10 m s^{-1} (Lang & SantAna, 2021). Consequently, the result of spray drying is typically evaluated based on the properties of the product powder and the macro-scale parameters of the spray drying process. The spray dryer is opaque to both the properties of individual partially-dried droplets and, especially, the outcome of collisions of those droplets. To overcome the challenges of studying the spray drying process, aspects of it are studied in isolation. The drying process of the droplets is commonly studied using single droplet drying methods (de Souza Lima et al., 2020). These methods have shown that droplet evaporation in spray drying occurs under conditions that promote accumulation of solute at the interface with clearly identifiable drying stages (Both et al., 2018; Sadek et al., 2015; Vehring et al., 2007). Typically, drying solute-containing droplets goes through three stages: a constant drying rate stage where the droplet shrinks at a constant rate and the evaporation rate is externally limited, a falling drying rate where the shrinking slows down and the evaporation rate is internally limited due to the accumulation of solute near the droplet's interface, and a final stage of morphological changes indicated by the locking of the droplet's surface, where the structural changes within the droplet take place (Both et al., 2018). A characteristic point in these three stages is the locking point, which is the transition between the second and the third stage. The locking point is the point where the shrinking of the droplet suddenly halts as the surface reaches some critical strength (Both et al., 2018). The benefit of single droplet drying methods mainly comes from isolating the droplet in a controlled environment where the drying rate can be set through setting temperature and humidity. Hence, we explore how a single droplet drying method and the drying stages can be used to relate to collision outcomes.

Various researchers have investigated the collision outcomes of solute-containing droplets, both in binary-droplet collisions and droplet-particle collisions, under conditions unaffected by evaporation. These studies have identified bouncing, stretching separation, reflexive separation, and coalescence as the most common collision outcomes (Krishnan & Loth, 2015; Pawar et al., 2016). However, disruption has also been observed in cases of high Weber numbers and low Capillary numbers (Finotello et al., 2019). While these studies provide valuable insights into the role of inertial force, surface tension force, and viscous force in determining the collision outcomes, they do not consider the effects of evaporation or the typical viscosity of droplets in spray drying. Therefore, they do not provide a complete understanding of how droplet evaporation affects collision outcomes under spray drying conditions.

To gain insight into the surface stickiness of evaporating droplets, researchers have used stickiness tests. These tests have shown that the sticky phase, where agglomeration is likely to occur, is reached earlier than expected based on bulk moisture content due to solute accumulation near the droplet's interface as a result of evaporation (Adhikari et al., 2003; Werner et al., 2007).

Petersen et al. (2015) conducted a study combining drying and collision outcomes by using a single droplet drying method. They employed an acoustic levitator in combination with a piston impactor to examine the influence of drying time on the transition between a droplet sticking to the piston and bouncing away from

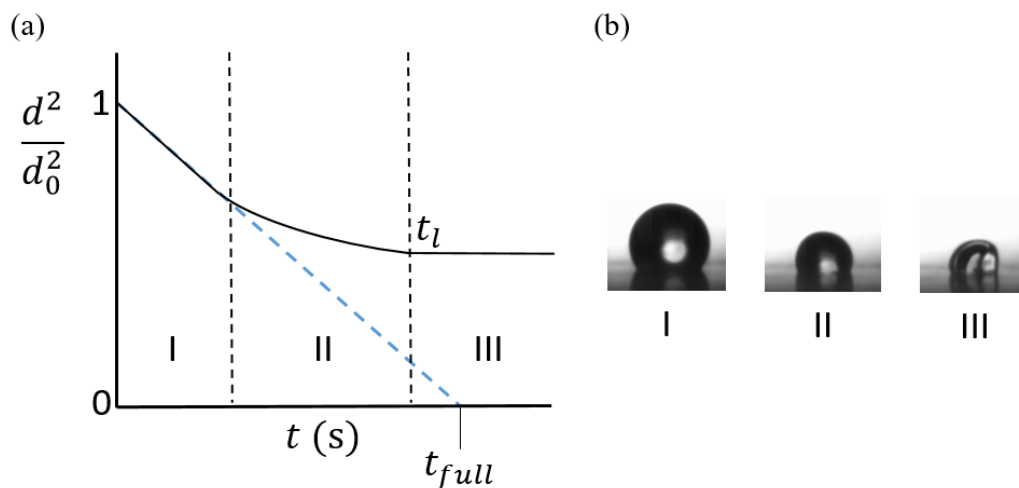


Figure 4.1: a) Schematic drying curve of a solute-containing droplet (black line) and a pure water droplet (blue line). t is the time, t_{full} is the time needed to fully dry the water droplet, and t_l is the time to reach the locking point. b) Typical droplet morphology during each drying stage.

it. They identified a critical t/R_0^2 value that marked the transition between sticking and bouncing, where t is the drying time and R_0 is the initial droplet radius (Petersen, 2015). However, it is important to note that collisions leading to agglomeration mostly involve dry particles and partially-dried droplets, whereas the collisions with the piston impactor are more similar to the collisions between partially-dried droplets and the spray dryer wall (van der Hoeven, 2008). Therefore, it is unclear whether this experimental approach can be used to develop predictive approaches for agglomeration. Further experimental investigation is necessary to validate its applicability in this regard.

Overall, while significant progress has been made in understanding the collision outcomes of solute-containing droplets, further research is needed to fully understand the effects of evaporation and the typical viscosity of droplets in spray drying on collision outcomes and agglomeration.

In this experimental work, we study the collisions outcomes of partially-dried maltodextrin-containing droplets with fully-dried maltodextrin particles. We developed a custom particle ejector setup to study the droplet-particle collisions of droplets in the upper range of the typical sizes of droplets in spray drying (Santos et al., 2018). Maltodextrin was chosen as a model system since it is commonly used as an excipient for spray drying purposes. We aim to explore how collision outcomes relate to the drying stages of the droplets and whether these drying stages provide a basis for a uniform predictive approach. To adequately test the universality of our predictive approach, we study the influence of initial maltodextrin concentration, environment temperature, and the dextrose equivalence of the maltodextrin.

As a basis for a unified approach to predicting collision outcomes, we choose two approaches: The first approach was based on the characteristic point in the three stages of the drying droplet. The locking point, being the transition from the second to the third drying stage, is the most characteristic and recognizable point of the drying curve related to the surface properties (Figure 4.1). The locking point is representative of a certain strength of the surface; we investigate whether the critical rheological conditions that trigger the locking point are predictive of the critical viscosity that results in sticking (Wallack & King, 1988). The second approach is a theoretical approach that uses the Péclet number, which represents the accumulating rate of advective solute transport due to the shrinking surface and the dispersing rate of diffusion at steady state drying conditions (Vehring et al., 2007).

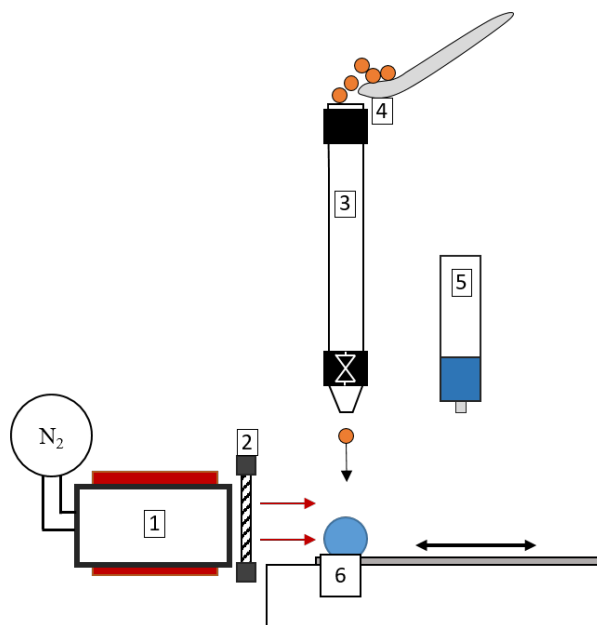


Figure 4.2: Schematic of the particle ejector setup. 1) is the heater, 2) is the shutter for controlling the hot flow to the droplet, 3) is the particle ejector tube, 4) is the powder loading site, 5) is the PipeJet dispenser and 6) is the location of the droplet, which sits on top of a movable hydrophobic PTFE surface.

4.2. Experimental

4.2.1. Materials

All maltodextrins originate from corn-starch and were obtained from Roquette Frères (Lestrem, France). Four different dextrose equivalents, 5, 12, 21, and 38%, were used. Maltodextrin solutions were made using deionized water. Initial maltodextrin concentrations of $c_0 = 10, 20$ and 30 wt% were chosen for the experiments. Maltodextrins are polysaccharides that are made by partial hydrolyzation of starch and consists of chains of D-glucose units. The maltodextrin variants are classified by the dextrose equivalence (DE), which represents the length of the glucose chain with lower DE meaning longer chains (Loret et al., 2004). Maltodextrins with different DEs, due to their different glucose-chain size, vary in their rheological behavior (Siemons et al., 2020).

4.2.2. Droplet drying setup

The drying unit and the particle ejector are both shown in Figure 4.2. A PipeJet P9 Nanodispenser (BioFLuidix GmbH, Freiburg, Germany) equipped with a 500 μm nozzle was used to dispense a droplet onto a hydrophobic PTFE substrate. The PTFE substrate lay on a glass slide, which itself lay on a custom 3D-printed PLA holder designed to allow only one-directional movement of the glass slide. Because of this, the droplet could, in a single handling, be rapidly moved in front of the camera and under the particle ejector exit. Subsequently, the shutter, which was blocking the hot N_2 flow from reaching the droplet, was opened and a timer was started to track the total time of drying. After the desired amount of time had passed, the valve of the particle ejector system was opened to drop the maltodextrin particles on top of the droplet.

Droplets were dried in the sessile single droplet drying unit. The drying medium was a temperature-controlled unidirectional flow of nitrogen gas. A temperature of $T_a = 25^\circ\text{C}$ at the droplet location was used as the reference setting. Additionally, for the $c_0 = 20$ wt%, N_2 temperatures of $T_a = 45^\circ\text{C}$ and $T_a = 65^\circ\text{C}$ at the droplet location were used.

4.2.3. Particle Ejector

The collisions between maltodextrin particles and partially-dried maltodextrin droplets were performed using a custom-built particle ejector and recorded using a high-speed camera (Phantom V9.1, Vision Research, USA). The particle ejector was designed to allow solid particles to fall onto a drying droplet. To achieve this, a vertical tube with a valve at the bottom was constructed. By pouring particles into the top of the tube, these particles fall on the closed valve. When the valve was opened, the particles would fall on top of the droplet due to gravity. The schematic of the particle ejector is shown in Figure 4.2. The particle ejector consists of a stainless steel tube with an internal diameter of 3.17 mm and a ball valve near the bottom. At the bottom exit, a cone-shaped constriction with a 700 μm diameter was made. The particle size of the purchased maltodextrin powder and droplet volume were taken into consideration during the design of the ejector. The ejection procedure of the particle ejector involved ensuring that the bottom valve was closed initially. A spatula tip of particles was loaded into the top of the particle ejector, which then fell to the bottom of the column, on top of the closed valve. Upon opening the bottom valve, the particles would fall on top of the drying droplet. The droplet was placed below the particle ejector exit to dry in the hot N_2 . After drying for the desired time, the bottom valve of the particle ejector was opened, and the particles dropped on top of the droplet. Even though multiple particles were loaded simultaneously, the first particle that hit the droplet was identifiable from the high-speed recording without any issues.

4.2.4. Collision image processing

Image processing for acquiring the relevant information, e.g. particle sizes, impact velocity, of the collisions was done with a custom script in MATLAB (2019b, Mathworks, USA). The collision type, coalescence, sticking or bouncing, was manually determined from the high-speed recording. The mean impact velocity that was obtained for all collisions was $v_i = 0.37 \pm 0.20 \text{ m s}^{-1}$. Although viscosity changes would affect the dispensed droplet volume, the aim was to maintain the same droplet volume throughout all experiments. The initial spherical equivalent diameter of the sessile droplets was $462 \pm 66 \mu\text{m}$. The spherical equivalent diameter of the purchased maltodextrin particles was $160 \pm 62 \mu\text{m}$. Based on these values, we obtain a range for the Weber number of 10^{-2} to 10^1 for all experiments, assuming a surface tension of $\sigma = 50 \text{ mN m}^{-1}$.

4.3. Results & Discussion

4.3.1. Collision outcomes

Collisions of maltodextrin particles with partially-dried droplets were performed using the particle ejector to determine the influence of partial drying on the collision outcome. As illustrated in Figure 4.3, three distinct collision types, coalescence, sticking, and bouncing, were identified. In the particle ejector experiments, these three collision types were identified based on the following observations. Coalescence was observed as the merging of the particle and the droplet. For these collisions, the particle impacted the droplet's surface, penetrated it, and then became submerged in the droplet. Within the coalescence collision type, there was variation in how quickly the particle became submerged in the droplet. Sticking was observed as the impingement of the particle on the droplet surface, where the particle became lodged onto the droplet's surface. Bouncing was observed as the impact and rebound of the particle on the droplet's surface.

The maltodextrin particles impacting the droplets had varying and non-spherical shapes, as can also be seen in Figure 4.3. The influence of particle shape on the collision outcome was assessed using the circularity parameter. However, circularity had a very minor influence on the collision outcome (Winkenius, 2021). Hence, we focus on the influence of the drying time and neglect the influence of particle shape. As mentioned in the experimental section, the impact velocity of the particles v_i was $0.37 \pm 0.20 \text{ m s}^{-1}$. Compared to the influence of drying on the collision outcome, this velocity range had a negligible influence on the collision outcome (Winkenius, 2021).

The full drying of the droplets takes several tens of seconds and depends mainly on the initial droplet volume, initial maltodextrin concentration, and air temperature. Figure 4.4 shows how the collision outcomes of all experiments vary based on the drying time. There is a substantial amount of overlap between the different

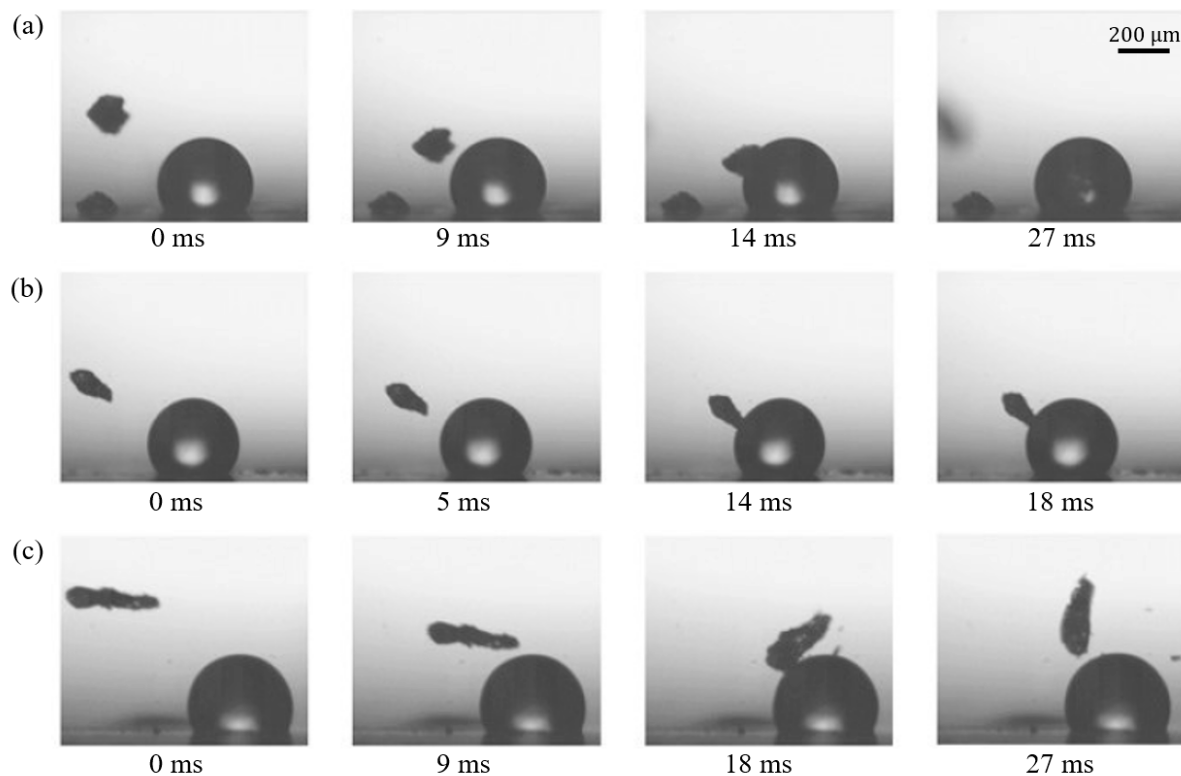


Figure 4.3: Four image series showing the typical collision outcomes. a) Coalescence. b) Sticking. c) Bouncing. The time of each frame is indicated in millisecond.

collision types due to the different experimental conditions. However, some overlap is also caused by the minor variation in droplet diameter resulting from variability in the dispenser.

4.3.2. Locking point acquisition

The drying of a droplet follows a typical drying curve with a constant rate regime, a falling rate regime, and a morphological development regime (Both et al., 2018). In Figure 4.5, the typical drying history of a maltodextrin-containing droplet is shown. The snapshots of the evaporation process show how the droplet initially shrinks until a point is reached where the circumference is locked into place, which for the droplet in the figure was at $t = 52$ s. Although, other typical morphological changes, such as wrinkling, were also detected (Sadek et al., 2015). However, these morphological changes were not a focus of this work. The transition from shrinking droplet to the morphological changes was sharp, making it straightforward to detect the moment of full locking and finding the locking point time t_l .

In Table 4.1, the timing of the locking point t_l determined from the single droplet drying experiments and adapted with t_{full} are shown. The t_l and the initial radius r_i are shown in Appendix 4.5.2. To account for variation by the droplet dispenser, the time of drying at the moment of collision t_l cannot be used to directly compare the influence of drying on the collision outcomes, as the drying time is proportional to the squared initial droplet diameter (Petersen, 2015). Hence, for any specific droplet i , we use $t_l/t_{full}(R_{0,i})$ to adapt for variation of the initial droplet size, where t_{full} is the time for full evaporation of a theoretical pure water droplet with an initial radius $R_{0,i}$, which is the initial equivalent sphere radius of the specific droplet i in the collision experiment. Similarly, we also normalize t_l with t_{full} , giving $t_l/t_{full}(R_{0,i})$. The calculation of t_{full} is shown in Appendix 4.5.1.

The comparison of the locking point time with experimental conditions showed a reduced locking point time for greater initial maltodextrin concentration c_0 . Compared to c_0 , increasing the temperature had a smaller effect, as no substantial trend was found. One reason why temperature did not noticeably influence $t_l/t_{full}(R_{0,i})$, is that t_{full} also reduces for greater temperature, while it is, per definition, unaffected by

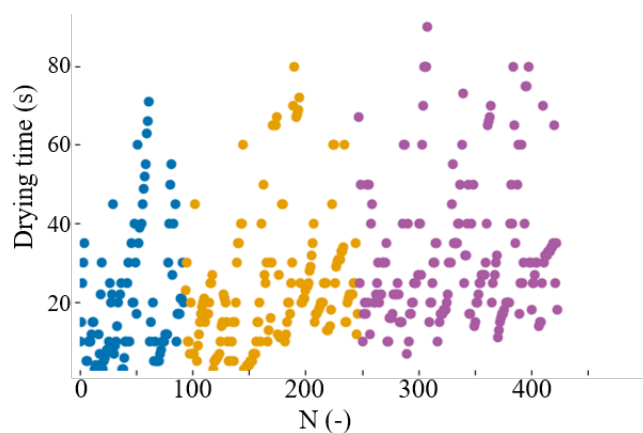


Figure 4.4: Collision outcome off all experiments in relation to the drying time in seconds, ordered based on collision outcome for the particle ejector. N is the number of the experiment. Blue is coalescence, yellow is sticking, and purple is bouncing. A strong overlap of collisions and drying time is found.

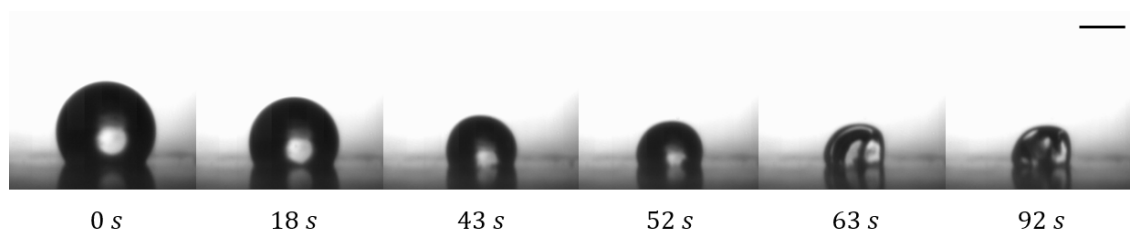


Figure 4.5: Capturing the drying history and locking point of a drying droplet. Snapshots of a 10 wt% maltodextrin droplet with an initial radius of $R_0 = 213 \mu\text{m}$ evaporating in a nitrogen flow at 25°C . The scale bar, which represents $200 \mu\text{m}$, is included for reference. The locking point time, t_l , was visually determined as the frame where the droplet circumference became locked and vacuole formation started, which for this series occurred at $t_l = 52\text{s}$.

Table 4.1: Adapted timing of the locking point $t_l/t_{full}(R_{0,i})$ for the used maltodextrin DEs, initial concentrations, and temperatures. The error margin is the standard deviation of four repetitions.

DE	c_0 (wt%)	25 °C	45 °C	65 °C
5	10	0.92±0.17	-	-
5	20	0.89±0.27	0.54±0.11	0.76±0.15
5	30	0.54±0.08	-	-
12	10	1.04±0.02	-	-
12	20	0.86±0.04	0.90±0.12	0.79±0.06
12	30	0.52±0.11	-	-
21	10	1.14±0.18	-	-
21	20	0.93±0.33	0.74±0.20	0.81±0.05
21	30	0.63±0.29	-	-
38	10	1.29±0.18	-	-
38	20	1.08±0.07	1.01±0.13	1.19±0.09
38	30	0.72±0.10	-	-

changes in c_0 . Hence, when increasing the temperature, both the locking point time and t_{full} decrease as a result of the higher temperatures. The $t_l/t_{full}(R_{0,i})$ was slightly higher for higher DE maltodextrins compared to lower DE maltodextrins, which we attributed to the greater viscosity of low DEs at similar concentrations (Siemons et al., 2020).

4.3.3. Collision outcome in relation to the locking point

To place the collision outcome in relation to the drying kinetics, the drying time of a droplet i at the moment of collision t is compared to t_l , where both t and t_l are adapted using t_{full} , resulting in

$$\tau_i = \frac{t_i}{t_{full}(R_{0,i})} / \frac{t_l}{t_{full}(R_{0,i})} = \frac{t_i}{t_l} \frac{t_{full}(R_{0,i})}{t_{full}(R_{0,i})} \quad (4.1)$$

The occurrence of coalescence, sticking and bouncing collisions in relation to the locking point are shown for maltodextrin DE5 and DE12 in Figure 4.6 and for maltodextrin DE21 and DE38 in Figure 4.7.

Coalescence, sticking and bouncing were commonly observed for all conditions, except $c_0 = 30$ wt%. For $c_0 = 30$ wt%, coalescence did not occur outside of a single instance for DE38. Visual observation showed that the droplets with $c_0 = 30$ wt% deformed much less upon particle impact than those with $c_0 = 10$ wt% or $c_0 = 20$ wt%. Suggesting that the initial viscosity was already sufficiently high to strongly reduce the likelihood of coalescence. Hence, it can be expected that further increase of c_0 will prevent coalescence due to the high initial viscosity, on the condition that the impact forces are small compared to viscous drag forces.

Comparing the collision outcomes to the locking point time showed that, expect for $c_0 = 10$ wt%, the transitions between collision outcomes occur substantially before the locking point time. For $c_0 = 10$ wt%, bouncing started at $\tau \approx 1$ for all DEs. For DE5 and DE12, sticking was observed as low as $\tau \approx 0.6$ and $\tau \approx 0.3$, respectively. For DE21 and DE38, sticking was isolated to a small region around the locking point time. For $c_0 = 20$ wt% and $c_0 = 30$ wt% at $T_a = 25$ °C, bouncing was observed to start as low as $\tau \approx 0.25$ to 0.5. Collisions at air temperatures of $T_a = 45$ °C and 65 °C showed a slight delay of bouncing compared to $T_a = 25$ °C, with only DE5 at $T_a = 45$ °C an outlier, however, the locking point time found for this condition also deviated from the overall trend.

The experimental results show that bouncing commonly starts at or before the locking point, and in many instances substantially before the locking point. Additionally, no clear trends of collision outcome as a result of the locking point were found. In the following section, we explore a second approach for predicting the collision outcome based on the findings of these experiments.

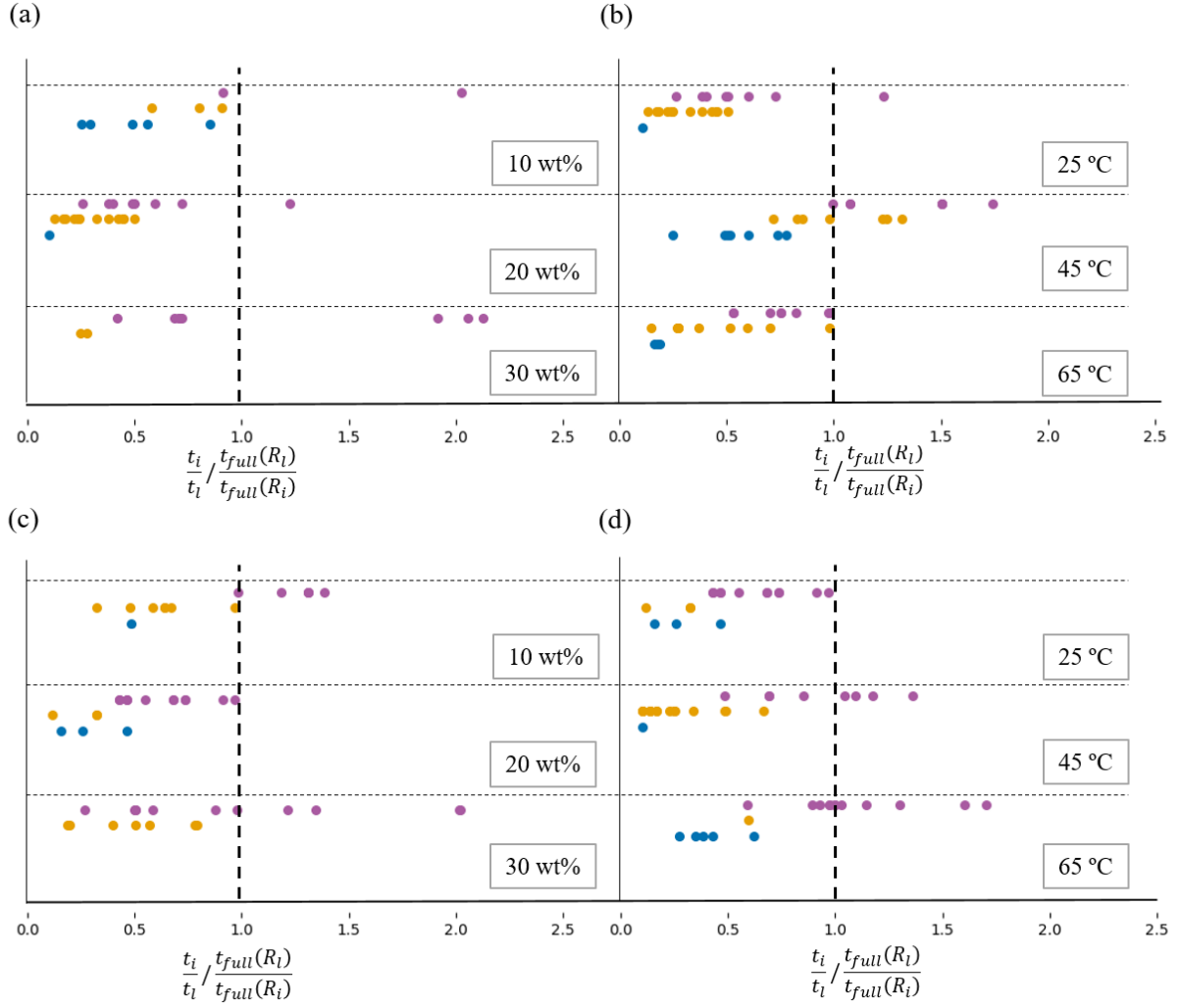


Figure 4.6: Relation of the collision outcome to the droplet locking point. Collision outcomes are color coded with coalescence as blue dots, sticking as yellow dots, and bouncing as purple dots. a) DE5 and c_0 dependence with $T_a = 25^\circ\text{C}$. b) DE5 and T_a dependence with $c_0 = 20\text{ wt}\%$. c) DE12 and c_0 dependence with $T_a = 25^\circ\text{C}$. d) DE12 and T_a dependence with $c_0 = 20\text{ wt}\%$. A dashed line is inserted to mark the locking point time.

4.3.4. Relating collision outcomes to the intra-droplet concentration gradient

The occurrence of bouncing collisions substantially earlier than the locking point has implications for the prediction of collision outcomes. The locking point is the condition where the skin has reached a critical strength so that it resists further shrinking. At the locking point, the surface is still wet and is expected to have mostly elastic properties for low DEs and viscous properties for high DEs (Siemons et al., 2020). Before the locking point, the maltodextrin droplets' behavior is expected to be viscous. Hence, this suggests that predicting of the collision outcome of partially-dried maltodextrin droplets is possible using methods that describe the merger of viscous liquid surfaces, such as with direct numerical simulation (Finotello et al., 2017) or using liquid bridging models (Paterson et al., 2015). These approaches do require a known viscosity. However, determining the viscosity is not straightforward, since the intra-droplet concentration is not radially homogeneous but a gradient. Since the droplet concentration is not radially homogeneous, the intra-droplet concentration gradient should be estimated to determine the contribution of the viscous force. The most successful way to predict the development of the intra-droplet concentration gradient is through numerical methods (Mezhericher et al., 2010), since experimental in situ measurement is still lacking (Schutyser et al., 2019; Sewalt et al., 2022). Our results suggest that numerical approaches to solve intra-droplet concentration gradients can exclude structural change for the purpose of predicting

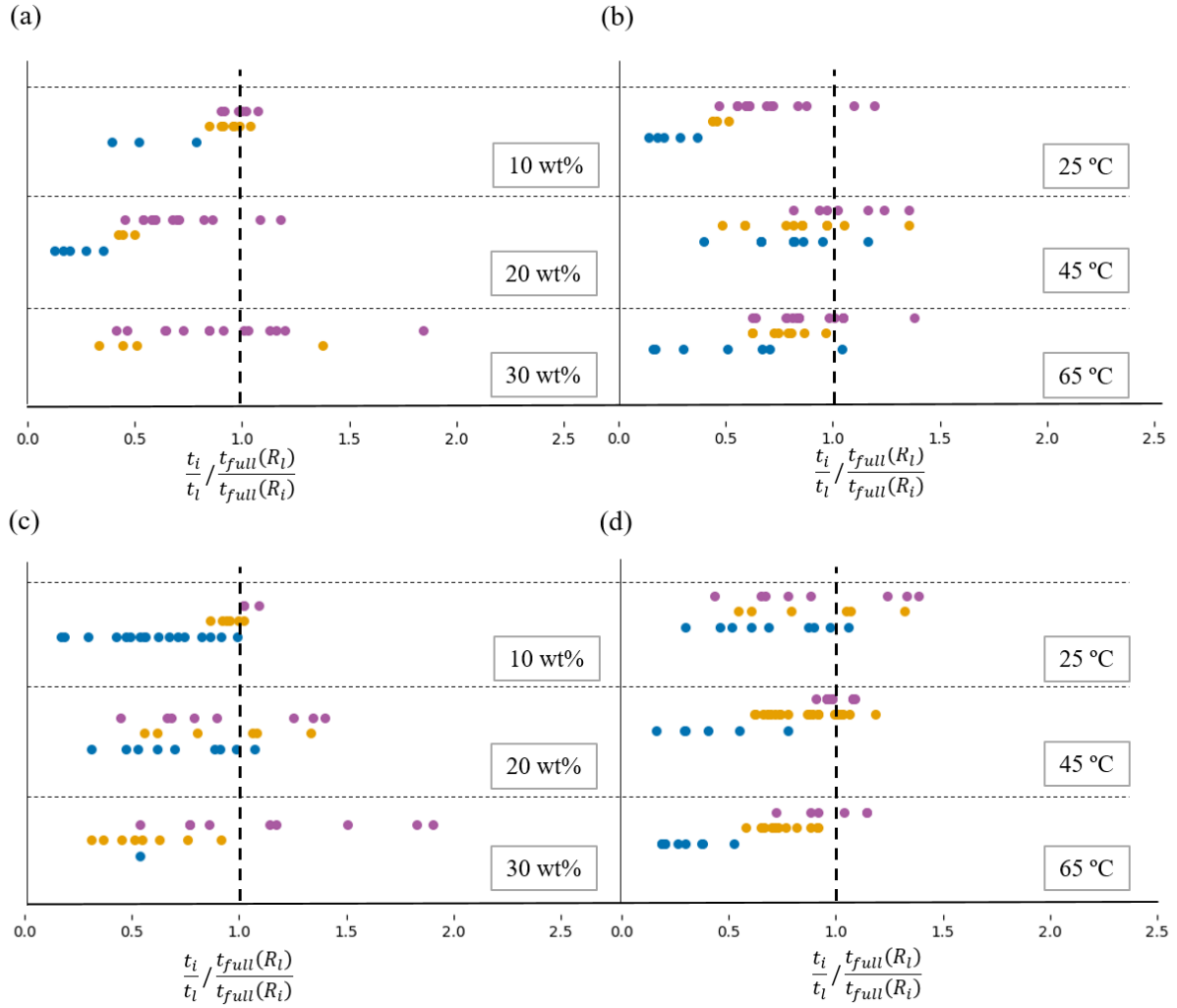


Figure 4.7: Relation of the collision outcome to the droplet locking point. Collision outcomes are color coded with coalescence as blue dots, sticking as yellow dots, and bouncing as purple dots. a) DE21 and c_0 dependence with $T_a = 25^\circ\text{C}$. b) DE21 and T_a dependence with $c_0 = 20\text{ wt}\%$. c) DE38 and c_0 dependence with $T_a = 25^\circ\text{C}$. d) DE38 and T_a dependence with $c_0 = 20\text{ wt}\%$. A dashed line is inserted to mark the locking point time.

collision outcomes.

Alternatively, the analytic solution of the intra-droplet concentration gradient can be used to estimate a rate of accumulation, which gives an indication of the droplet surface properties. This rate of accumulation can be described with the dimensionless Péclet number, which follows from the analytic solution (Vehring et al., 2007). The Péclet number is defined as $Pe(r, t) = \kappa/8D(r, t)$, where κ is the evaporation constant, and $D(r, t)$ the maltodextrin solute diffusion coefficient (Vehring et al., 2007). When $Pe \gg 1$, the droplet develops a sharp concentration gradient where the surface solute concentration becomes much greater than the concentration in the center. When $Pe \ll 1$, the solute concentration remains homogeneous and minimal surface accumulation is expected (Bouman et al., 2016). Since our locking point analysis suggested that for most of the tested conditions the transitions between collision types occurs while the droplet displays viscous behavior, we find it sensible to compare the collision results with the rate of surface accumulation as described by the Péclet number. The parameters DE, c_0 , and T_a were varied in the collision experiments. These parameters all influence the $Pe(r, t)$ independently. Moreover, the $Pe(r, t)$ changes during drying due to the increasing viscosity, which affects $D(r, t)$. To negate the radial influence during evaporation, we will use $Pe(r, t = 0)$, which is independent of r , to inspect how the expected rate of surface accumulation relates to different collision outcomes. We will refer to $Pe(r, 0)$ as Pe throughout

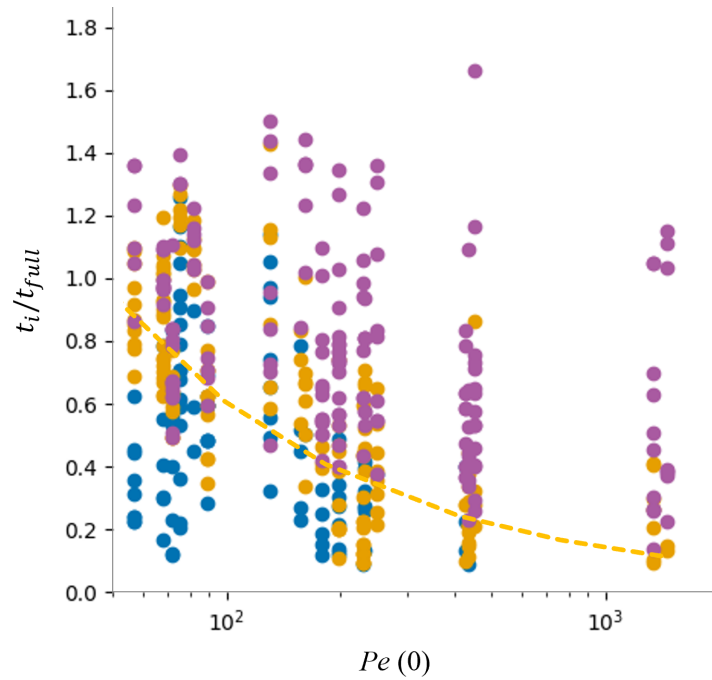


Figure 4.8: Relation of the collision outcome to Pe . Collision outcomes are presented for all conditions. Coalescence is blue, sticking is orange and bouncing is purple. The dashed orange line is the power law trend line fitted to the sticking collisions.

the following sections. The Pe for each condition is shown in Table 4.2. D was calculated with the Stokes-Einstein equation with an estimated hydrodynamic diameter of 2 nm (Qi and Tester, 2018).

Table 4.2: The estimated $Pe(r, 0)$ for the used DEs, concentrations, and temperatures in the particle ejector experiments. The Pe is calculated using the wet bulb temperature.

DE	c(wt%)	25 °C	45 °C	65 °C
5	10	157	-	-
5	20	434	231	198
5	30	1453	-	-
12	10	161	-	-
12	20	427	229	197
12	30	1344	-	-
21	10	82	-	-
21	20	179	89	72
21	30	451	-	-
38	10	75	-	-
38	20	130	68	57
38	30	250	-	-

For all conditions $Pe \gg 1$ is true, thus, substantial surface accumulation was expected to occur in the droplets, which matched the observations during the collision experiments. Pe strongly increased with c_0 and decreased for greater DE. The Pe was comparable for DE5 and DE12 maltodextrin and similarly so for DE21 and DE38. Since κ does not change with DE, the difference can only be attributed to the solute diffusion coefficient, which is primarily affected by viscosity. Since rheological data shows that maltodextrins with lower DE have greater viscosity at similar concentrations, greater Pe values for lower DEs at the same c_0 can be explained by this more rapid scaling of viscosity for greater DEs (Siemons et al., 2020).

To visualize the relation of collision outcome to Pe , the dependence of the collision outcomes on Pe is

shown for all collision experiments in Figure 4.8. Here, it shows that collision outcomes become separated based on t/t_{full} and Pe . Coalescence occurs at low Pe and short drying times. Bouncing occurs at high Pe and long drying times. Sticking occurs predominantly in the overlap region between coalescence and bouncing. Hence, the grouping of the collision outcomes suggests that $Pe(0)$, describing the rate of surface accumulation based on initial droplet properties, appears to be potent indicator of after how much drying time an evaporating droplet transitions from coalescence to sticking and from sticking to bouncing. Even with variations in the DE, c_0 , and T_a , their independent influence on the collision outcomes is captured adequately by the $Pe(0)$. Consequently, the rate of solute accumulation at the interface as a result of droplet properties and drying environment unifies the effects of these parameters.

The unification of the collision types could allow an operator to steer the drying conditions to promote agglomeration. To promote agglomeration for the conditions in this work, our results suggest that the drying time should be tuned to approximate the empirical power law trend line for the stickiness collisions, which is $t_{stick}/t_{full} = 9.9Pe(0)^{-0.60}$, where t_{stick} is the time where sticking is the most probably collision outcome. We find this power law to be valid for maltodextrins of DE5, 12, 21 and 38 over a range of $Pe(0) = 50$ to 1500. Note that relevant values for t/t_{full} do not increase much further than $t/t_{full} = 1$, since by then the droplet will have fully dried.

The analysis presented here is sensitive to the impact velocity, since stickiness is affected by impact velocity (Sewalt et al., 2020). This trend line was found for a range of impact velocities of $v_i = 0.37 \pm 0.20 \text{ ms}^{-1}$. As particle velocities in spray drying are greater than those used in the particle ejector experiments (Santos et al., 2018), we expect that dependence on v_i must be tested to assess the application of this empirical relation in spray drying. The relation of Pe to the collision outcome is established for the experimental ranges in this work. This relation Within the experimental ranges used here, the influence material viscosity and the drying rate did not strongly affect the relation of Pe to the collision outcome.

Additionally, the used experimental range does not exclude that the material itself and the drying rate, although Pe does account for these, could substantially affect the relation of Pe to the collision outcome. Especially, since droplets dry at much higher temperatures in spray drying conditions. Hence, the empirical relations that describes maximum stickiness or the onset of separation should ideally be determined for each material independently until the universality of this approach is tested for a wider range of conditions.

4.4. Conclusion

In this work, we investigated the influence of drying on the collision outcome of maltodextrin particles impacting on sessile maltodextrin-containing droplets. We observed three different collision outcomes: coalescence, sticking, and bouncing, which occur in order of increasing drying time. The boundaries between the three collision outcomes were strongly affected by the initial solute concentration, temperature and maltodextrin dextrose equivalent. To unify these boundaries, we explored two approaches: normalizing the drying time with the locking point time and presenting the collision outcome in a map with two non-dimensional quantities, the normalized drying time and the Péclet number. We compared the occurrence of these collision outcomes to the locking point as a measure for the properties of the droplet surface. Contrary to expectations, bouncing collisions occurred substantially earlier than the locking point time for nearly all tested conditions, except when the initial concentration was 10 % by weight. Since initial concentrations for spray drying in the food sector are typically much higher, we expect that the transitions between coalescence, sticking, and bouncing for maltodextrins in spray drying do not rely on the structural dependencies that lead to surface locking. Instead, our results suggest that the transitions between coalescence, sticking, and bouncing are determined by viscous behavior as a result of the intra-droplet concentration gradient. We found that coalescence, sticking, and bouncing collisions could be separated based on t/t_{full} and $Pe(0)$, reflecting the steady state intra-droplet solute concentration gradient based on initial properties. Low $Pe(0)$ and t/t_{full} were dominated by coalescence, while high $Pe(0)$ and t/t_{full} were dominated by bouncing. In the transition region, sticking was the dominant collision outcome. We established an empirical relation of $t_{stick}/t_{full} = 9.9Pe(0)^{-0.60}$, where t_{stick} is the drying time corresponding to a maximum likelihood of the stickiness collision outcome, which is ideal for agglomeration. The regime plot of t/t_{full} and $Pe(0)$ shows a promising result for predicting collision outcomes. However, we acknowledge that the dependence

of collision outcomes on $Pe(0)$ may be specific to the impact velocity and drying rates used in this work. Thus, further studies using a broader range of parameters are needed to assess how they affect the found empirical relation.

4.5. Appendix

4.5.1. Calculations

Constant drying for stage 1 of drying in Figure 4.1 is defined by the radius-square law (Equation (A.1), Jakubczyk et al., 2012). Solving the radius for $R(t) = 0$ gives the full drying time t_{full} for a pure water droplet, which is calculated as

$$t_{full} = \frac{R_0^2}{\kappa} \quad (\text{A.1})$$

where κ is the evaporation rate with units $\frac{m^2}{s}$.

The D is determined from the Stokes-Einstein equation,

$$D = \frac{k_b T_s}{6\pi\eta_0 r_h} \quad (\text{A.2})$$

where k_b is the Boltzmann constant and r_h is the hydrodynamic radius. The r_h is estimated as 1 nm (Qi and Tester, 2018). The initial viscosity η_0 for each maltodextrin DE is calculated from equation 5 in the work by Both et al (Both et al., 2019) on aqueous MD12 solutions. We used the fitting parameters found by the authors for calculating η_0 from c_0 .

4.5.2. Locking point raw data

Table 4.3: Locking point times t_i and initial radii r_i from the locking point experiments. The results from all four repetitions are shown.

DE	c_0 (wt%)	T (°C)	t_{i1} (s)	r_{i1} (μm)	t_{i2} (s)	r_{i2} (μm)	t_{i3} (s)	r_{i3} (μm)	t_{i4} (s)	r_{i4} (μm)
5	10	25	56	213.1	43	231.3	52	230.5	44	231.4
5	20	25	35	218.2	41	197.9	52	198.3	23	197.3
5	30	25	20	181.7	28	211.5	14	179.6	23	185.7
12	10	25	45	203.3	50	215.1	51	212.8	-	-
12	20	25	36	207.4	36	194.7	31	187.5	30	178.8
12	30	25	25	182.9	24	206.2	17	193.4	20	212.8
21	10	25	51	191.1	62	217.6	49	227.2	-	-
21	20	25	70	213.4	37	196.5	29	206.3	29	203.0
21	30	25	42	186.6	24	231.8	29	233.5	27	233.4
38	10	25	58	196.6	65	203.6	54	203.3	52	218.3
38	20	25	50	226.9	43	207.2	46	204.0	45	194.3
38	30	25	43	226.9	24	207.2	33	204.0	28	194.3
5	20	45	17	215.2	28	244.0	19	247.1	17	243.7
12	20	45	20	197.1	31	206.8	27	207.8	24	205.9
21	20	45	31	219.5	34	248.5	28	244.0	19	259.7
38	20	45	39	221.9	30	226.5	36	230.1	30	227.4
5	20	65	20	207.8	22	254.8	19	249.3	18	249.2
12	20	65	15	206.9	21	226.3	17	221.0	20	225.2
21	20	65	18	208.4	15	195.3	14	200.1	14	198.6
38	20	65	29	227.6	16	180.6	19	177.4	18	177.9

Bibliography

- Adhikari, B., Howes, T., Bhandari, B. R., & Truong, V. (2003). In situ characterization of stickiness of sugar-rich foods using a linear actuator driven stickiness testing device. *Journal of Food Engineering*, 58(1), 11–22. [https://doi.org/10.1016/s0260-8774\(02\)00328-x](https://doi.org/10.1016/s0260-8774(02)00328-x)
- Both, E. M., Nuzzo, M., Millqvist-Fureby, A., Boom, R. M., & Schutyser, M. A. I. (2018). Morphology development during single droplet drying of mixed component formulations and milk. *Food Research International*, 109, 448–454. <https://doi.org/10.1016/j.foodres.2018.04.043>
- Both, E. M., Siemons, I., Boom, R. M., & Schutyser, M. A. I. (2019). The role of viscosity in morphology development during single droplet drying. *Food Hydrocolloids*, 94, 510–518. <https://doi.org/10.1016/j.foodhyd.2019.03.023>
- Bouman, J., Venema, P., de Vries, R. J., van der Linden, E., & Schutyser, M. A. I. (2016). Hole and vacuole formation during drying of sessile whey protein droplets. *Food Research International*, 84, 128–135. <https://doi.org/10.1016/j.foodres.2016.03.027>
- de Souza Lima, R., Ré, M.-I., & Arlabosse, P. (2020). Drying droplet as a template for solid formation: A review. *Powder Technology*, 359, 161–171. <https://doi.org/10.1016/j.powtec.2019.09.052>
- Finotello, G., Padding, J. T., Buist, K. A., Jongasma, A., Innings, F., & Kuipers, J. A. M. (2019). Droplet collisions of water and milk in a spray with langevin turbulence dispersion. *International Journal of Multiphase Flow*, 114, 154–167. <https://doi.org/10.1016/j.ijmultiphaseflow.2019.03.003>
- Finotello, G., Padding, J. T., Deen, N. G., Jongasma, A., Innings, F., & Kuipers, J. A. M. (2017). Effect of viscosity on droplet-droplet collisional interaction. *Physics of Fluids*, 29(6), 067102. <https://doi.org/10.1063/1.4984081>
- Jakubczyk, D., Kolwas, M., Derkachov, G., Kolwas, K., & Zientara, M. (2012). Evaporation of microdroplets: The "radius-square-law" revisited. *Acta Physica Polonica-Series A General Physics*, 122(4), 709. <https://doi.org/10.12693/aphyspola.122.709>
- Krishnan, K. G., & Loth, E. (2015). Effects of gas and droplet characteristics on drop-drop collision outcome regimes. *International Journal of Multiphase Flow*, 77, 171–186. <https://doi.org/10.1016/j.ijmultiphaseflow.2015.08.003>
- Lang, E., & SantAna, A. S. (2021). Microbial contaminants in powdered infant formula: What is the impact of spray-drying on microbial inactivation? *Current Opinion in Food Science*, 42, 195–202. <https://doi.org/10.1016/j.cofs.2021.06.007>
- Loret, C., Meunier, V., Frith, W. J., & Fryer, P. J. (2004). Rheological characterisation of the gelation behaviour of maltodextrin aqueous solutions. *Carbohydrate Polymers*, 57(2), 153–163. <https://doi.org/10.1016/j.carbpol.2004.03.026>
- Mezhericher, M., Levy, A., & Borde, I. J. D. T. (2010). Theoretical models of single droplet drying kinetics: A review. *Drying Technology*, 28(2), 278–293. <https://doi.org/10.1080/07373930903530337>
- Paterson, A. H. J., Ripberger, G. D., & Bridges, R. P. (2015). Measurement of the viscosity of freeze dried amorphous lactose near the glass transition temperature. *International Dairy Journal*, 43, 27–32. <https://doi.org/10.1016/j.idairyj.2014.11.005>
- Pawar, S. K., Henrikson, F., Finotello, G., Padding, J. T., Deen, N. G., Jongasma, A., Innings, F., & Kuipers, J. H. (2016). An experimental study of droplet-particle collisions. *Powder Technology*, 300, 157–163. <https://doi.org/10.1016/j.powtec.2016.06.005>
- Petersen, T. (2015). *Model stickiness in spray drying* (Ph.D. Thesis). Technical University of Denmark. Technical University of Denmark.
- Qi, X., & Tester, R. F. (2018). Is starch or maltodextrin glucose? *Starch-Stärke*, 70(9-10), 1700304. <https://doi.org/10.1002/star.201700304>
- Sadek, C., Schuck, P., Fallourd, Y., Pradeau, N., Le Floch-Fouéré, C., & Jeantet, R. (2015). Drying of a single droplet to investigate processstructurefunction relationships: a review. *Dairy Science and Technology*, 95(6), 771–794.
- Santos, D., Mauricio, A. C., Sencadas, V., Santos, J. D., Fernandes, M. H., & Gomes, P. S. (2018). Spray drying: An overview. *Pignatello, R.(Comp.). Biomaterials-Physics and Chemistry-New Edition. InTech. UK*, 9–35. <https://doi.org/10.5772/intechopen.72247>

- Schutyser, M. A. I., Both, E. M., Siemons, I., Vaessen, E. M. J., & Zhang, L. (2019). Gaining insight on spray drying behavior of foods via single droplet drying analyses. *Drying Technology*, *37*(5), 525–534.
- Sewalt, E. J. G., Kalkman, J., van Ommen, J. R., Meesters, G. M. H., & van Steijn, V. (2022). Revealing how maltodextrin-containing droplets dry using optical coherence tomography. *Food Research International*, *157*, 111049. <https://doi.org/10.1016/j.foodres.2022.111049>
- Sewalt, E. J. G., Zhang, F., van Steijn, V., van Ommen, J. R., & Meesters, G. M. H. (2020). Static and dynamic stickiness tests to measure particle stickiness. *KONA Powder and Particle Journal*, 2021017. <https://doi.org/10.14356/kona.2021017>
- Siemons, I., Politiek, R. G. A., Boom, R. M., van der Sman, R. G. M., & Schutyser, M. A. I. (2020). Dextrose equivalence of maltodextrins determines particle morphology development during single sessile droplet drying. *Food Research International*, *131*, 108988. <https://doi.org/10.1016/j.foodres.2020.108988>
- van der Hoeven, M. (2008, August 1). *Particle-droplet collisions in spray drying* (Ph.D. Thesis). School of Engineering, The University of Queensland.
- Vehring, R., Foss, W. R., & Lechuga-Ballesteros, D. (2007). Particle formation in spray drying. *Journal of Aerosol Science*, *38*(7), 728–746. <https://doi.org/10.1016/j.jaerosci.2007.04.005>
- Verdurmen, R. E. M., Menn, P., Ritzert, J., Blei, S., Nhumaio, G. C. S., Sonne Sørensen, T., Gunging, M., Straatsma, J., Verschueren, M., Sibeijn, M., et al. (2004). Simulation of agglomeration in spray drying installations: The edecad project. *Drying technology*, *22*(6), 1403–1461. <https://doi.org/10.1081/drt-120038735>
- Wallack, D. A., & King, C. J. (1988). Sticking and agglomeration of hygroscopic, amorphous carbohydrate and food powders. *Biotechnology Progress*, *4*(1), 31–35. <https://doi.org/10.1002/btpr.5420040106>
- Werner, S. R. L., Jones, J. R., & Paterson, A. H. J. (2007). Stickiness of maltodextrins using probe tack test during in-situ drying. *Journal of food engineering*, *80*(3), 859–868. <https://doi.org/10.1016/j.jfoodeng.2006.08.008>
- Winkenius, S. (2021). *The influence of partial drying on the collision outcome of a droplet-particle collision* (MSc. Thesis). Delft University of Technology.

5

Experimental characterization of partially-dried droplet collisions for mapping regimes using the glass transition

Agglomeration in spray drying can be used to control the properties of powder, such as flowability and dispersibility. This process occurs through inducing collisions between partially-dried droplets, the outcome of which is largely determined by the droplet properties that change significantly due to evaporation. However, predicting the effect of evaporation on droplet properties and collision outcomes is challenging due to a lack of experimental insight under spray drying conditions. To investigate this, we performed experimental collisions of maltodextrin-containing droplets in two setups: one operating under spray drying conditions, and another under milder drying conditions, with the droplet diameter ranging between 170 μm to 480 μm . We performed different sets of experiments in which we varied droplet diameter, maltodextrin types, maltodextrine concentration, drying temperatures, and relative humidities. We commonly observed three different collision outcomes: coalescence, sticking, and bouncing, with the boundaries between these regimes depending on the drying time. Given that the drying time varied over three orders of magnitude (0.1 s to 100 s) between the different sets of experiment, we investigated up to what extent the boundaries can be made universal between all sets by comparing the drying time to the time required for the surface of a drying droplet to reach a glassy state. This time was predicted with a deterministic one-dimensional numerical model. For the mild drying conditions, the transition from coalescence/sticking collisions to bouncing collisions occurred around the same order-of-magnitude of drying time as the time needed to reach the glass transition at the droplet's surface. However, for the fastest drying rates approximating industrial spray drying, bouncing collisions were observed until four times the time needed to reach the surface glass transition. Our work shows that the rationale to use the time required for a droplet's surface to reach the glassy states is a valid approach to determine the boundary at which droplets bounce when dried at mild conditions. This underlines the importance to take into account the spatio-temporal maltodextrin concentration inside drying droplets in predicting the collision outcome. The experiments at the highest drying rates suggest that surface stickiness as captured by the one-dimensional model in the form of the time for a droplet to obtain a glassy surface is too simplistic to successfully predict collision outcomes of partially-dried droplets.

5.1. Introduction

Spray drying is a widely used method for producing powders with desired properties. Agglomeration of solute-containing microdroplets in a spray dryer is an effective way to achieve good flowability and increased dispersability of the powder. Agglomerates, which are particles consisting of smaller constituent particles stuck together in an open structure, can be formed through droplet collisions when the droplets are sticky. During evaporation, droplets go from the liquid state to the dry particle state, and are temporarily sticky in between. Liquid droplet collisions typically result in coalescence, while sticky droplet collisions result in agglomeration, and dried droplet collisions result in bouncing (Adhikari et al., 2007; Elesini et al., 2016; Sewalt et al., 2023). Tuning the conditions in a spray dryer is crucial to achieve the desired collision outcome, such as agglomeration between droplets or bouncing between droplets and the dryer wall. Therefore, it is important for both the design and operation of spray dryers to understand the relationship between drying time and collision outcome of partially-dried droplets.

Most literature on droplet collisions considers non-drying, non-solute containing droplets. Outcomes that have been reported for those collisions are coalescence and bouncing, with the boundaries being rationalized in terms of the dominant forces at play, as for example captured by the Capillary or Weber number (Finotello et al., 2017; Krishnan & Loth, 2015). While important insights can be drawn from collision between non-drying, non-solute containing droplets, a crucial difference with collisions between drying solute-containing droplets is that the properties of the droplet, especially its surface, change during drying, influencing its deformability and stickiness. Hence, the established boundaries for collision outcomes resulting from an analysis of the relevant forces for non-drying, non-solute containing droplets break down when introducing heterogeneity as a result of drying.

Particles that resemble partially-dried droplets in spray drying are commonly studied in particle stickiness measurements (Adhikari et al., 2001). These measurements involve heating or liquefaction of particles until it is observed that these particles become sticky. The measurement of stickiness is done based on the difference between the temperature of the particle and the glass transition temperature of the particle's surface ($T - T_g$) (Sewalt et al., 2020). The collision outcome of a particle is related to this difference $T - T_g$ and the impact velocity (Murti et al., 2010; Palzer, 2005; Sewalt et al., 2020). A deposition criterion for the sticking to bouncing transition has been developed but requires properties that are difficult to determine for the surface of a drying droplet (Walmsley et al., 2014). While stickiness measurements resemble spray drying properties more closely than droplet-droplet or particle-droplet collisions, they typically involve bringing particles from the glassy state to the rubbery state. This makes it unclear how well the results translate to spray drying, as droplets in spray drying start as viscous droplets and transition through the rubbery state to the glassy state. Additionally, the sticky-point found from the glassy state is different from the sticky-point found from the liquid state, and only the probe tack method approaches the glassy state from the liquid state, but this method is not suitable for measuring properties of droplets drying in spray drying conditions (Adhikari et al., 2003; Kudra, 2003).

Experimental studies involving collisions between drying, solute-containing droplets are limited. Petersen (2015) used an acoustic levitator to dry solute-containing droplets and collided them with a piston to investigate collision outcomes. Presenting the outcome in terms of the drying time, they found clear regimes for sticking and bouncing, yet with a substantial overlap between these regimes. This overlap was attributed for the variation in initial droplet radius (R_0). Accounting for this variation, by scaling the drying time t_{dry} with the square root of the initial droplet radius, they showed that there is a critical t_{dry}/R_0^2 that describes the boundary between the sticking and bouncing outcomes of partially-dried solute-containing droplets.

Besides experimental work, numerical approaches have been used to simulate evaporation and predict collisions or spray drying performance. These methods include identifying the locking point (Verheijen, 2021), comparing surface tension and viscous forces (Verdurmen et al., 2004), and using the surface glass transition temperature to predict droplet stickiness (Adhikari et al., 2005). However, these approaches have not been compared with dedicated collision experiments of partially-dried droplets, except for one study (Petersen, 2015). It remains unclear how accurately these methods can predict collision outcomes and agglomeration performance. Therefore, more experiments are necessary to understand whether sur-

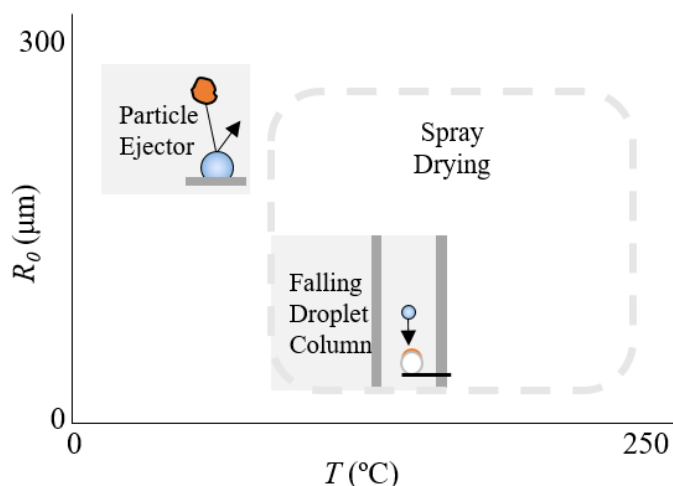


Figure 5.1: Map of the initial droplet radius and air temperature, showing the here-presented collision setups in relation to typical conditions for spray drying in the food sector.

face stickiness from a numerical evaporation model can explain transitions between collision outcomes of partially-dried droplets under spray drying conditions.

In this study, we conduct experimental collisions of partially-dried maltodextrin droplets using two collision setups. One setup collides dry maltodextrin particles with a drying sessile maltodextrin droplet, while the other setup has free-falling maltodextrin droplets that dry under spray drying-like conditions and collide with a solid maltodextrin coated particle. The typical operating conditions of these setups are shown in Figure 5.1. We use maltodextrins with varying polymer lengths to investigate the impact of material properties and vary initial concentration and environmental temperature to explore the influence of these parameters on the collision outcomes. To interpret the results, we compare the collision outcomes at different drying times with the time required for the droplet's surface to reach the glass transition temperature, predicted numerically using a one-dimensional model. Our aim is to determine to what extent this approach is predictive for the transitions between the collision regimes for our experiments.

5.2. Experimental

5.2.1. Solution preparation

Maltodextrin agglomerates with dextrose equivalents of 5, 12, 21, and 38 (Glucidex, Roquette Frères) were individually mixed with deionized water to make solutions. Fresh solutions were prepared before each experiment, which took place within 5 days of preparation. Samples were refrigerated until use.

5.2.2. Falling particles on a stagnant partially-dried droplet - particle ejector

Collisions of dry particles falling on stagnant maltodextrin droplets drying over a timescale of about 1 min were performed using the particle ejector (PE), which is shown schematically in Figure 5.2a. The particle ejector consists of a stainless steel tube of 1.6 mm diameter with two valves on either end. At the bottom exit, a cone-shaped constriction is made with a 700 μm diameter. Halfway the tube, a t-shape connection is made to connect a pressurized air-line. This pressurized air has two functions. Firstly, it can be used to clean the main tube of residual powder. Secondly, it can be used to pressurize the main tube to increase the impact velocity. The latter was not used for this publication, as the maltodextrin agglomerates of the powder were too weak to withstand the higher pressure and disintegrated upon exiting the particle ejector.

The ejection procedure of the particle ejector is by first ensuring that the bottom valve is closed. While the top valve is open, a small amount of particles is loaded into the top of the particle ejector. The particles proceed to fall through the column on top of the closed bottom valve, readying the system for the collision

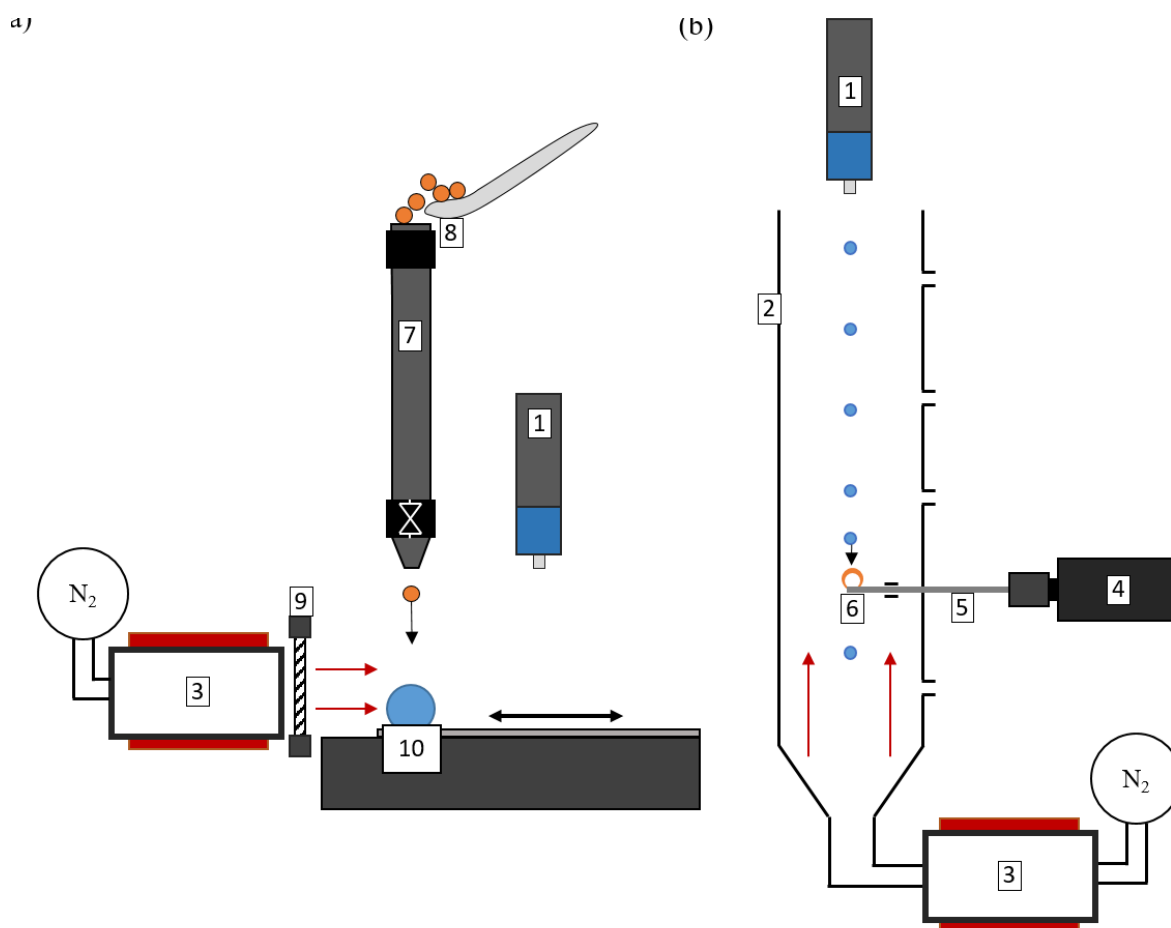


Figure 5.2: Schematic of a) the particle ejector setup and b) the falling droplet column setup. 1: PipeJet Nanodispenser. 2: Glass column. 3: Heating system for the nitrogen supply. 4: High-speed camera. 5: Borescope. 6: Collision object covered with a fully-dried maltodextrin film. 7: Particle Ejector system. 8: Loading site. 9: Diaphragm. 10: Hydrophobic PTFE surface.

experiment. After the droplet, which was placed directly below the exit of the particle ejector, had evaporated the desired amount in a stream of dry nitrogen with a controlled temperature, the bottom valve of the particle ejector was opened, dropping the particles on top of the drying droplet. While several dozens of particles were loaded simultaneously, the particle that hit the droplet first could be clearly identified from the high-speed recording (Phantom V9.1, Vision Research).

5.2.3. Falling partially-dried droplets on a stagnant particle - falling droplet column

Collisions of small falling droplets drying over a timescale of about 1 s on a stagnant dry particle were performed using the falling droplet column (FDC), which is shown schematically in Figure 5.2b. The FDC consists of a glass column of 60 cm length with an inner diameter of 2.6 cm. Hot nitrogen was blown upwards through the column, which controls the temperature and humidity. A heating system and mass flow controller maintained the temperature and the flow rate. A flow rate of 6 L min^{-1} to 8 L min^{-1} was used, which results in a flow velocity of $\approx 0.2 \text{ m s}^{-1}$. Initially, the hot nitrogen did not maintain a uniform temperatures over the length of the column. This was solved by placing an infrared-lamp along the length of the column to maintain the temperature of the insulating housing around the column, resulting in less cooling of the nitrogen. A PipeJet P9 NanoDispenser (BioFluidix GmbH, Freiburg) equipped with a nozzle

having an orifice diameter of 125 μm was placed above the column for droplet dispensing. Along the side of the column - the falling path of the droplet - there were six slots in the column with 5.7 mm diameter. On these locations, also holes in the insulating housing were made to allow insertion of a collision object into the column. A high-speed camera (Phantom V9.1, Vision Research) with a borescope (series 5, Olympus) was fitted with a custom-made extension that allowed for a small glass sphere ($d \approx 1.75 \text{ mm}$) to be inserted, as the collision object, into the column and the path of the droplets. Before insertion of the borescope, a film of maltodextrin solution was pipetted onto the glass sphere and left to dry.

Collisions were recorded by setting the nozzle to continuously dispense. When a droplet collided with the dried film on the glass sphere, the borescope was removed from the column. Repeating this process for different slots resulted in collisions with different falling heights, leading to different drying times.

The impact velocity, droplet size and collision outcome was determined from the recording of the collision using a custom script (MATLAB, 2017b). The drying time and initial radius for each droplet were estimated from the impact velocities and droplet size measured close to the dispenser and at each hole in the glass column.

5.2.4. Evaporation model

A one-dimensional deterministic numerical model was used to simulate the evaporation process of the maltodextrin-containing droplets and obtain the time t_{glass} necessary for reaching the T_g at the droplet's surface. The complete description of the model is presented in Appendix section 5.6.

5.3. Results & Discussion

5.3.1. Experimental collisions

The collision experiments were carried out using two experimental setups, namely the particle ejector and the falling droplet column setup. For the particle ejector, droplet diameters of $450 \pm 30 \mu\text{m}$ and temperatures of 25 $^{\circ}\text{C}$, 45 $^{\circ}\text{C}$ and 65 $^{\circ}\text{C}$ were used, resulting in drying times between 16 s to 77 s. The falling droplet column approximated spray drying conditions with temperatures of $100 \pm 20 \text{ }^{\circ}\text{C}$ and droplet diameters of $210 \pm 40 \mu\text{m}$, with drying times between 0.10 s to 1.29 s. In both setups, three distinct collision outcomes were identified. The collision outcomes were coalescence, sticking, and bouncing. Examples of these collision outcomes for both experimental setups are illustrated in Figure 5.3. The three observed outcomes are in line with those reported for droplet-droplet collisions (Krishnan & Loth, 2015).

For the particle ejector setup, coalescence was defined as the submersion of the particle in the droplet, sticking was defined as the impingement of the particle on the droplet surface, and bouncing was defined as the impact of the particle on the droplet surface followed by a rebound. For the falling droplet column setup, coalescence was defined as the wetting of the droplet on the film after impact, where the droplet deformed strongly, and the contact angle of the droplet adapted to the maltodextrin film. Sticking was defined as the impingement of the droplet on the film, with minimal deformation of the droplet while maintaining the spherical droplet shape. In this case, no noticeable wetting or contact angle change took place between the impacting droplet and the dried maltodextrin film. Bouncing was defined as the impact on the film and subsequent rebound of the droplet.

The different collision outcomes were observed by varying the drying time of the droplets at different temperatures of the nitrogen flow. The temperatures were selected to achieve a broad range of drying rates and times, ranging from lab-scale to spray-drying conditions. We note that variation in drying time was also introduced through variations in droplets diameter dispensed by the PipeJet dispenser. While those variations are minor, they may translate into significant variations in drying time and in the observed transition between sticking and bouncing (Petersen, 2015), explained by the drying time being proportional to the square of the initial droplet diameter (Jakubczyk et al., 2012). The collisions observed in the falling droplet column and the particle ejector were separated based on their outcomes. As shown in Figure 5.4a and b, respectively, collisions in the particle ejector exhibited a greater overlap compared to collisions in the falling droplet column. For the falling droplet column, we see that the outcomes depend on the drying

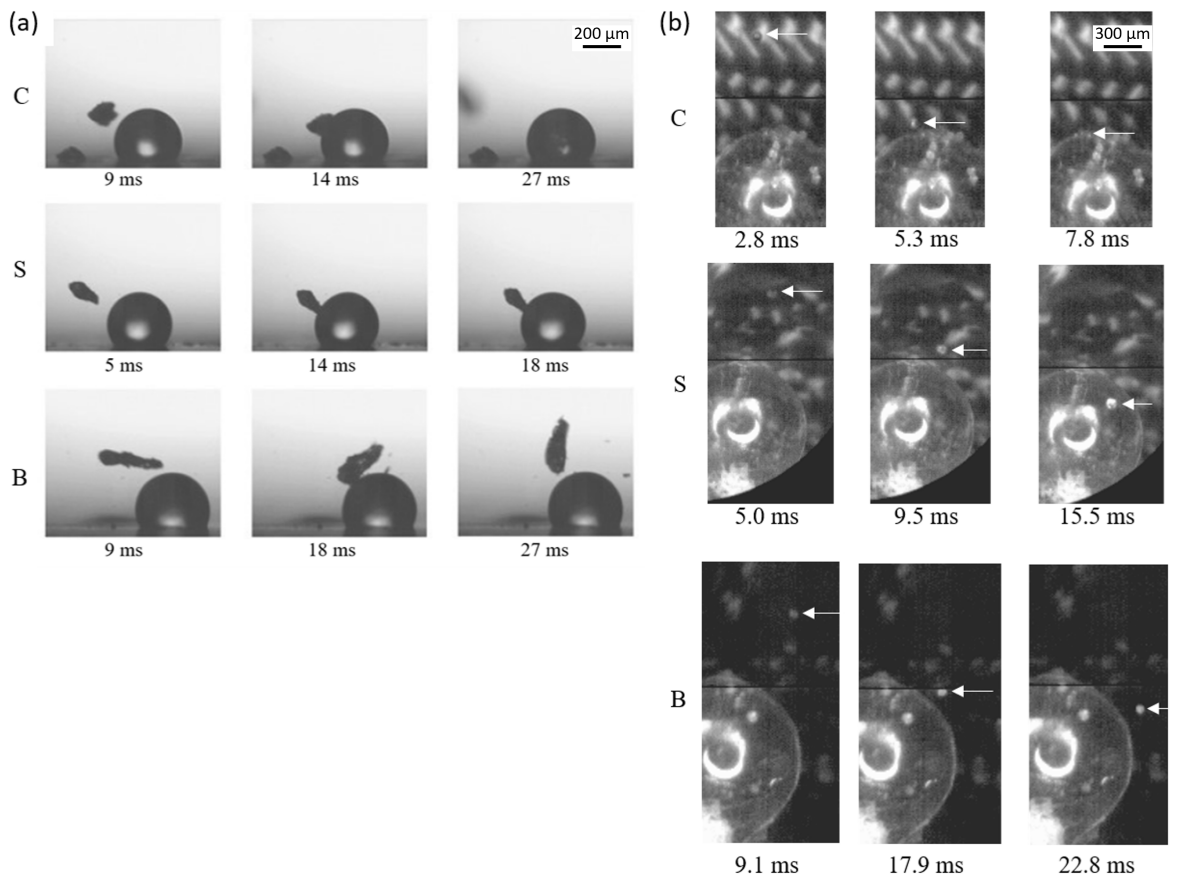


Figure 5.3: Images of the coalescence (C), sticking (S) and bouncing (B) as observed from a) the particle ejector and b) the falling droplet column.

time, where we observe coalescence, sticking and bouncing at increasing drying times. For the particle ejector, we see the same trend, but with much more overlap as compared to the more intense conditions in the falling droplet column. This overlap was mainly a result of a broader experimental range of initial solids concentration, drying temperature, and droplet diameter. We note that the impact velocity for both collision setups was similar, with values of $0.4 \pm 0.2 \text{ m s}^{-1}$ for the particle ejector and $0.5 \pm 0.2 \text{ m s}^{-1}$ for the falling droplet column. Therefore, there was little variation in the impact velocity, and its influence on collision outcome is expected to be negligible compared to the influence of droplet properties (Sewalt et al., 2020; Winkenius, 2021). Particle shape and size were also investigated for the particle ejector, and a negligible influence was found, except for extreme outliers (Winkenius, 2021).

5.3.2. Comparison of experimental collisions with the surface glass transition as a predictor of collision outcome

Rapidly drying droplets can develop a sharp concentration gradient, with the surface concentration being highly elevated from the initial concentration, while the concentration in the droplet's center remains close to the initial concentration (Vehring et al., 2007). This means that surface properties change more rapidly than bulk properties, affecting the collision outcomes (Adhikari et al., 2003). Surface stickiness, based on the surface properties, can potentially be used to predict collision outcomes. Stickiness is strongly related to the glass transition, so the surface $T - T_g$ provides a measure of the stickiness of a partially dried droplet (Sewalt et al., 2020; van der Hoeven, 2008).

Measuring the concentration gradient and temperature in the droplet at drying rates and droplet diameters approximating spray drying is extremely challenging, instead, we opted for a numerical model to determine

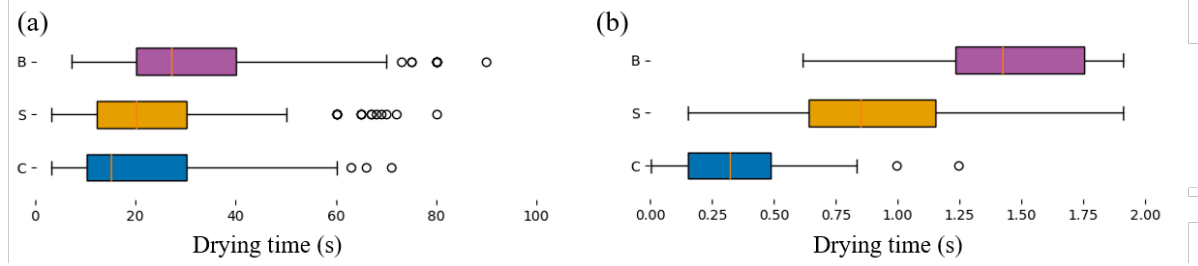


Figure 5.4: Boxplot of the collision outcomes in relation to the drying time in seconds, separated based on collision outcome for a) the particle ejector and b) the falling droplet column. C are coalescence collisions, S are sticking collisions, and B are bouncing collisions. The circles are 1.5 times the interquartile range greater or smaller than Q3 and Q1, respectively.

the surface $T - T_g$ of the droplets. For each experimental condition in both the particle ejector and the falling droplet column, the model predicted the corresponding droplet's concentration gradient and surface $T - T_g$. Figure 5.5 shows an example of the model output for a droplet in the falling droplet column. The radius of the droplet gradually decreased until the surface glass transition was reached at a drying time of 0.27 s. Surface concentration increased from 20 wt% to 80 wt% where the glass transition was reached. Figure 5.5b shows that the $T_g - T$ followed a similar curve as the surface concentration, only increasing more rapidly after 0.2 s. The droplet temperature exhibited different stages of drying. Until 0.1 s, the droplet adapted to the heating environment. Then, from 0.1 s to 0.25 s, the wet bulb temperature was maintained until the evaporation rate was reduced due to the accumulation of solids at the droplet surface, hindering the transfer of water to the environment, causing temperature to increase (Sadek et al., 2015).

In Table 5.1, we present the modeling results for each experimental condition. While there was variation in the initial droplet diameter for both the particle ejector and the falling droplet column due to the inherent variation of the dispenser, the model did not account for this variation. Instead, a single value for the initial droplet diameter was used.

Therefore, the obtained t_{glass} was adjusted assuming $t_{glass} \sim R_0^2$ (Petersen, 2015). This relation closely approximated the modeled values when the droplet diameter did not vary too greatly. A constant initial droplet radius of 240 μm was used for the particle ejector, and the mean initial diameter was used for each different experimental condition for the falling droplet column.

The t_{glass} values obtained ranged from $t_{glass} = 0.12$ s to 53.9 s. These values are of the same order of magnitude as the drying times under investigation in the experimental collisions. The results from the particle ejector provide the clearest insight into the influence of initial solids concentration, air temperature, and dextrose equivalence.

The initial solids concentration had the greatest influence on the t_{glass} , as observed from a rapid decrease in t_{glass} when increasing the initial solids concentration for the particle ejector experiments. For DE5, increasing the initial solids concentration from 10 wt% to 30 wt% decreased t_{glass} from 53.9 s to 11.8 s. Although not as impactful on intra-droplet gradient formation as the initial solids concentration, greater temperature substantially reduced the modeled t_{glass} . Increasing the environment temperature T from 25 $^\circ\text{C}$ to 65 $^\circ\text{C}$ decreased t_{glass} from 27.5 s to 10.2 s for DE5. The dextrose equivalence had a minor influence on the t_{glass} , with greater values for the DE slightly increasing the observed t_{glass} .

Thus, the initial droplet diameter and initial solids concentration had the most substantial influence on the intra-droplet gradient formation and, therefore, the droplet's surface properties.

Further insight into the formation of intra-droplet gradients can be gained by analyzing the ratio of t_{glass}/t_{full} , where t_{full} is the time in seconds required for complete evaporation of a pure water droplet with an equivalent initial radius. For the calculation of t_{full} , see equation A.1 in Chapter 4. This ratio provides an indication of how quickly solids accumulate at the droplet's interface. A value $t_{glass}/t_{full} \approx 1$ indicates that the surface glass transition is reached around the same time a pure water droplet with equivalent initial radius would fully evaporate. This indicates little surface accumulation takes place, hence, surface

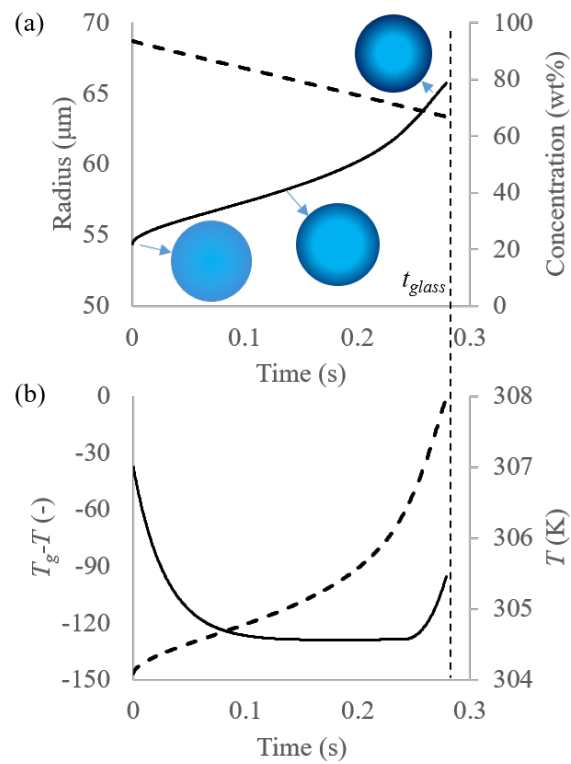


Figure 5.5: Example output of the numerical evaporation model. a) The radius of the droplet (dashed) and the surface concentration of maltodextrin (dashed). The approximate gradient in the droplet is shown graphically for three points, with light blue low concentrations and dark blue high concentrations. b) $T - T_g$ for the droplet surface (solid) and T for the droplet (dashed). The thin dashed line indicates the moment of reaching t_{glass} , the time until reaching the glass transition at the interface.

Table 5.1: t_{glass} and t_{glass}/t_{full} as calculated with the one-dimensional evaporation model for the chosen conditions particle ejector (PE) and the falling droplet column (FDC).

Setup	DE	c_0 (wt%)	T (°C)	t_{glass} (s)	t_{glass}/t_{full}
PE	5	10	25	53.9	0.93
PE	5	20	25	27.5	0.48
PE	5	30	25	11.8	0.20
PE	5	20	45	15.6	0.42
PE	5	20	65	10.2	0.39
PE	12	10	25	53.9	0.93
PE	12	20	25	27.5	0.48
PE	12	30	25	11.9	0.21
PE	12	20	45	15.5	0.42
PE	12	20	65	10.3	0.39
PE	21	10	25	55.4	0.96
PE	21	20	25	28.7	0.50
PE	21	30	25	12.4	0.21
PE	21	20	45	16.3	0.44
PE	21	20	65	10.7	0.41
PE	38	10	25	57.8	1.00
PE	38	20	25	31.8	0.55
PE	38	30	25	14.5	0.25
PE	38	20	45	18.7	0.51
PE	38	20	65	12.8	0.49
FDC	5	30	105	0.73	0.07
FDC	5	20	91	1.15	0.28
FDC	5	30	111	0.28	0.32
FDC	12	20	85	1.25	0.40
FDC	12	30	125	0.46	0.11
FDC	12	30	111	0.25	0.38
FDC	21	20	125	0.63	0.33
FDC	21	35	100	0.44	0.10
FDC	21	35	109	0.21	0.20
FDC	21	35	109	0.22	0.17
FDC	21	40	109	0.19	0.10
FDC	38	20	120	1.74	0.38
FDC	38	30	105	0.74	0.32
FDC	38	40	85	0.51	0.09
FDC	38	50	94	0.12	0.05

concentration is similar to bulk concentration. When $t_{glass}/t_{full} \ll 1$, the surface glass transition occurs substantially before a pure water droplet of equivalent diameter has fully evaporated. In this situation it is expected that a sharp intra-droplet maltodextrin concentration gradient has formed.

For all experimental conditions, a range of $t_{glass}/t_{full} = 0.05$ to 1 was observed, where a value of 0.05 indicates that the glass transition was reached at the droplet interface at only 5% of the drying time of a pure water droplet with an equivalent radius.

A value close to one for t_{glass}/t_{full} at $c_0 = 10$ wt% and $T = 25$ °C suggests that no significant surface accumulation took place under this condition, as the surface glass transition occurred around the time of full evaporation of a pure water droplet of equivalent diameter. For all other conditions, t_{glass}/t_{full} indicated that substantial surface accumulation took place, especially when the initial solids concentration was increased as observed from the low values for t_{glass}/t_{full} for the c_0 of 40 wt% and 50 wt%.

By knowing the t_{glass} for each experimental condition, the collision outcomes can be related to the con-

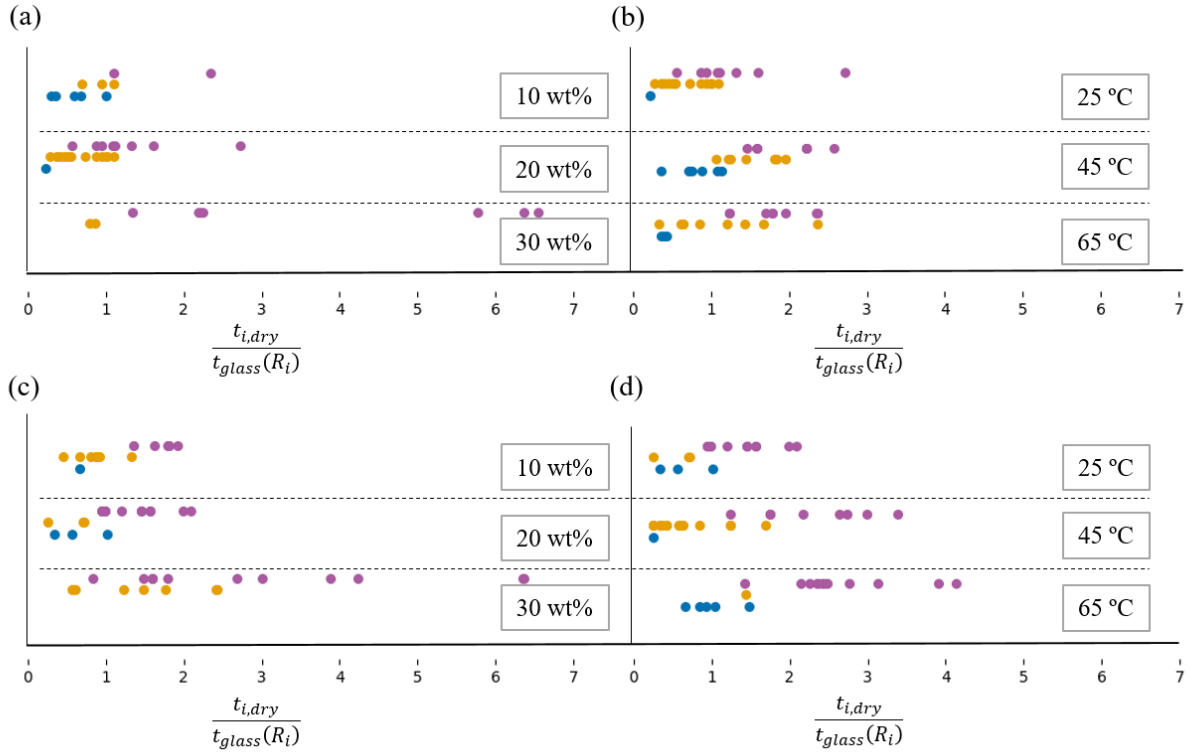


Figure 5.6: Relation of the collision outcome to the surface glass transition for the particle ejector collision setup. Collision outcomes are color coded with coalescence as blue dots, sticking as yellow dots, and bouncing as purple dots. a) DE5 and c_0 dependence. b) DE5 and T dependence. c) DE12 and c_0 dependence. d) DE12 and T dependence.

ditions at the droplet's surface. In the following sections, the drying times t_{dry} for each experimental collision are compared to the t_{glass} values obtained from the simulation of droplet evaporation.

Comparison of particle ejector collisions with surface glass transition

The drying times of collisions resulting from the particle ejector were compared to the modeled t_{glass} . The ratio of t_{dry}/t_{glass} was plotted for DE5 and DE12 in Figure 5.6 and for DE21 and DE38 in Figure 5.7.

It was expected that the transition between sticking and bouncing would occur around $t_{dry}/t_{glass} = 1$. For DE5 and DE12, due to the overlap between sticking and bouncing, no exact transition time was found. However, the first instances of bouncing were generally observed in the range of $t_{dry}/t_{glass} = 0.5$ to 1.5. Hence, the modeled onset of the glass transition at the droplet surface provided an approximation of the start of bouncing. For DE21 and DE38, there was also substantial overlap between the collision types, and, similarly, no exact transition times could be defined. The first instances of bouncing for all collisions at 25 °C showed similar behavior as for the collisions using DE5 and DE12. However, when the air temperature was 45 °C or 65 °C, the first instances of bouncing were delayed to $t_{dry}/t_{glass} = 1.5$ to 2.2, which was particularly prominent for the maltodextrin DE38 sample.

These results from the particle ejector led to several conclusions. First, normalizing the drying time with the time for the droplet's surface to reach the glassy state, which was calculated from a one-dimensional deterministic model, provided an order of magnitude prediction of when the occurrence of coalescence/sticking collisions was replaced by bouncing collisions. Second, the absence of a clear transition shows that while the drying time in relation to t_{glass} primarily determined collision outcome, there are secondary effects that affected the collision outcomes. Previous studies have shown an influence of impact velocity and size ratio, which had minor variation in the particle ejector experiments (Krishnan & Loth, 2015). Our results showed that a change in temperature and a change in DE affected the timing of the transitions between

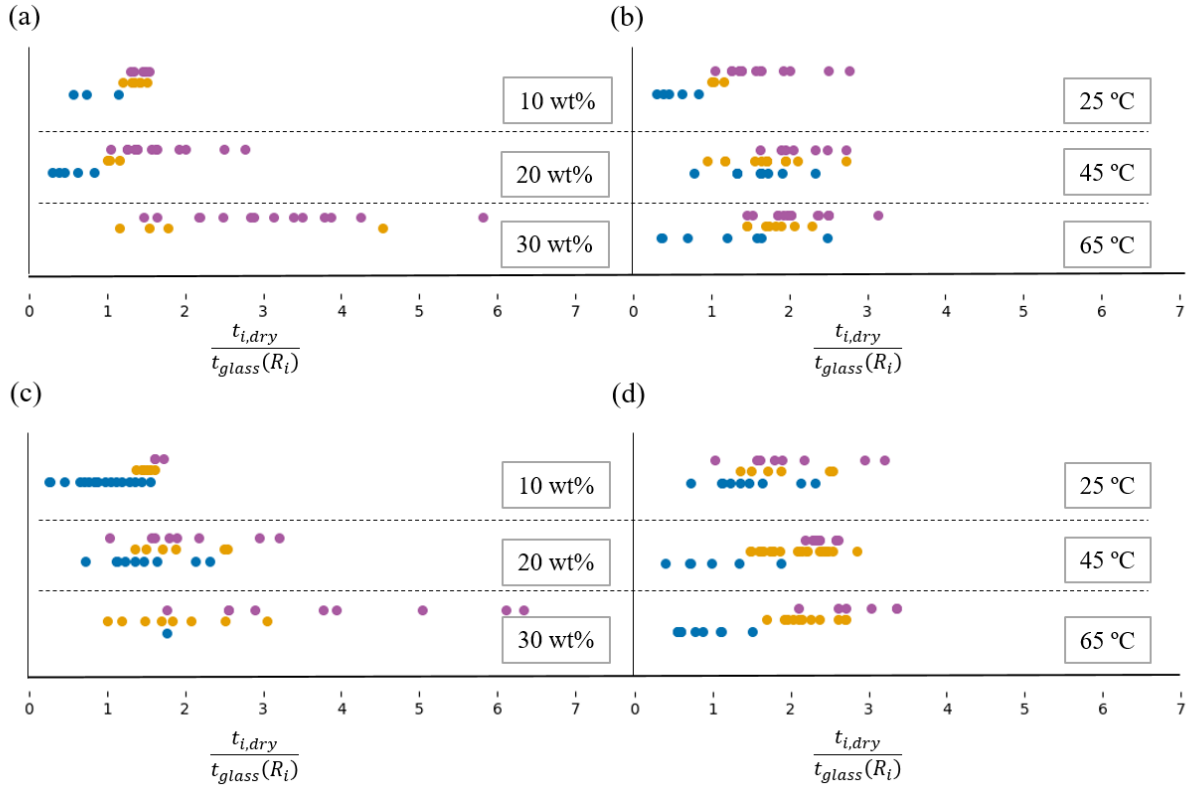


Figure 5.7: Relation of the collision outcome to the surface glass transition for the particle ejector collision setup. Collision outcomes are color coded with coalescence as blue dots, sticking as yellow dots, and bouncing as purple dots. a) DE21 and c_0 dependence. b) DE21 and T dependence. c) DE38 and c_0 dependence. d) DE38 and T dependence.

collisions. The change in DE is primarily a change in viscosity due to the different scaling of viscosity with solids concentration for different DEs. However, the comparison with t_{glass} using the model takes the differences in viscous behavior between DEs into account. Temperature and viscosity do affect how the shape of the radial gradient of maltodextrin concentration develops during evaporation (Vehring et al., 2007). In the next section, further insight on the influence of temperature and DE is gained from the falling droplet column collisions.

5.3.3. Comparison of falling droplet column collisions with surface glass transition

Collisions of partially-dried droplets and dried maltodextrin films were performed using the falling droplet column. Similar to the particle ejector experiments, the collision outcomes were related to t_{glass} and are shown in Figure 5.8. Notably, bouncing only occurred for DE5, DE12, and DE21 for the smallest droplets with the highest initial concentration. For larger droplets or lower initial concentrations, no bouncing occurred. We expect that the droplets had not sufficiently dried before reaching the bottom of the drying column. Collisions of DE38 did not result in bouncing at all, even for the $c_0 = 50\text{wt}\%$ sample, which had the shortest t_{glass} out of all experiments. An explanation is proposed based on the anhydrous glass transition temperature $T_{g,s}$. For DE38, this $T_{g,s}$ was lower than T , which meant that under equilibrium conditions, the maltodextrin solution would not reach the glassy state. Hence, the droplet's surface would not become dry, nor would the maltodextrin film be in the glassy state at the used temperatures. A comparison with t_{glass} shows that, except for DE38, the occurrence of coalescence for all DEs matches the timing for DE21 and DE38 in the particle ejector experiments. For the FDC, bouncing occurred at $t_{dry}/t_{glass} > 3.5$ for DE5 and at later times for DE12 and DE21, up to $t_{dry}/t_{glass} > 4.5$ for DE21. Compared to the PE, the timing of sticking collisions was very broad, ranging from $t_{dry}/t_{glass} < 1$ to $t_{dry}/t_{glass} = 7.5, 5.5,$ and 8.5 for DE5, DE12, and DE21, respectively.

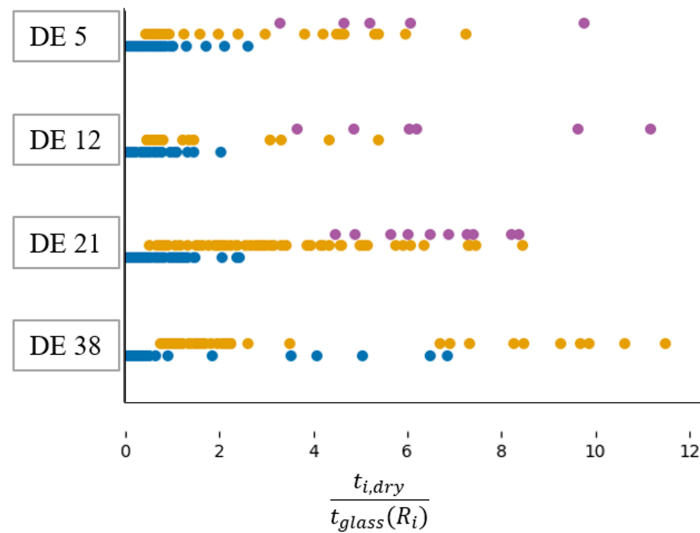


Figure 5.8: Relation of the collision outcome to the surface glass transition for the falling droplet collision setup. Collision outcomes are color coded with coalescence as blue dots, sticking as yellow dots, and bouncing as purple dots.

Whereas the particle ejector experiments showed a minor influence of secondary effects such as temperature and DE, this influence was greater for the collisions in the falling droplet column. Surprisingly, for DE5, 12, and 21, drying had to be extended for around four times the expected time based on the modeling of surface glass transition. This required searching the operating limits of the dispenser with regards to droplet diameter and initial viscosity. This behavior was unexpected and challenges the hypothesis that collision behavior of droplets is a result of surface stickiness. Consequently, the experiments presented in this work suggest that the surface conditions alone cannot be used to represent the droplet when predicting collision outcomes and that other variables must be taken into account.

5.4. Discussion

Our results from both the particle ejector and the falling droplet column suggest that the numerically predicted glass transition of the droplet surface provides an order-of-magnitude estimation of when the transition from coalescence and sticking to bouncing occurs. Additionally, they also suggest a substantial influence from temperature and material properties on the transitions between collision outcomes. Moreover, the collisions presented in this work support the idea that surface conditions of droplets alone are insufficient to explain collision outcomes of partially-dried droplets.

We found over a range of initial concentrations and environmental temperatures that the surface properties, defined as the time in seconds until reaching the glass transition temperature, do not fully explain the transitions between collision types. While there were already small variations in the onset of bouncing for the particle ejector collisions, the FDC data shows a much greater offset when comparing the onset of bouncing. If a critical surface condition would result in different collision outcomes, it would be expected that transitions would occur at similar timings for different conditions. Therefore, our work suggests that other factors must be included for more accurate prediction of collision outcomes, and that the rate of solids accumulation is a crucial aspect of characterizing the collision outcomes of partially-dried maltodextrin droplets (Sewalt et al., 2023).

Especially at higher temperatures that approach spray drying conditions, the deviation from the numerically predicted surface T_g became substantial. Therefore, approaches that apply numerical prediction should take this deviation into account and characterize how changes in operating conditions influence the collision timings. Alternatively, operators must account for larger margin of errors when estimating the sticky-dry transition based on numerical prediction.

An intuitive explanation for the secondary effects of temperature and material properties on the relation of the collision outcomes to the t_{glass} is that the surface layer, while it might be at or approaching the glassy condition, is too thin to have a collision without bending or breaking. Hence, the subsurface layer would also play a relevant role in the collision outcome. Depending on how sharp the concentration gradient is, the subsurface layer can have similar properties to the surface if the concentration gradient is shallow, or, have a much lower concentration when the concentration gradient is sharp. Our results suggest that predictive relations for partially-dried collisions should account for the shape of the entire concentration gradient in combination with an assessment of the surface properties.

Overall, our study highlights the importance of considering the effects of temperature and material properties on collision outcomes of partially-dried droplets, and underscores the need for a more comprehensive understanding of the underlying physical mechanisms. Future work could focus on characterizing the properties of the subsurface layer and its role in collision outcomes, as well as investigating the influence of other factors such as droplet diameter and velocity.

5.5. Conclusion

Maltodextrin droplets were partially dried before colliding with a solid maltodextrin particle in the particle ejector and a dried maltodextrin film in the falling droplet column. The two setups allowed for exploring total drying times over a range between 0.1 s to 100 s, through varying the droplet size and air temperature. Three different collision outcomes were found, coalescence, sticking and bouncing, which occurred in order of increasing drying time. Greater initial concentration strongly reduced the drying times where transition between collision occurred, while greater temperature mildly reduced these drying times.

Numerical prediction of droplet surface properties as a result of evaporation was compared to the experimental collision outcomes. Whereas it was expected that the collision outcome would be related to a specific surface condition, such as the transition from a viscous to a glassy state, only an order-of-magnitude accuracy was found for the numerically predicted time to reach the glass transition at the droplet's surface. The particle ejector collisions showed a dependency of collision outcome on dextrose equivalence, initial solids concentration, and temperature. For the smaller droplets at fast drying rates in the falling droplet column, no bouncing was observed for DE38 due to the glass transition temperature being below the air temperature. The transition from coalescence/sticking to bouncing collisions occurred at drying times around four times longer than the time to reach the surface glass transition temperature. These results indicated that a critical surface condition alone, while commonly used for assessing particle stickiness, is insufficient for predicting collision outcomes of partially-dried droplets. Besides the surface conditions, the experimental collisions in this work suggest that the shape of the intra-droplet concentration gradient has a substantial influence on the collision outcome of partially-dried droplets. Hence, methods that use numerical prediction of droplet properties should account for the shape of the intra-droplet concentration gradient at the moment of collision.

5.6. Appendix

5.6.1. Numerical model for obtaining the time until glass transition at the droplet's surface

This appendix draws upon the MSc thesis of Lorenzo Presili (Presili, 2020), which was supervised by Erik Sewalt as part of his Ph.D. thesis.

The results of the experimental collisions at various drying times in this chapter are interpreted by comparing them to the time required for the surface of a drying droplet to reach the glassy state. To achieve this objective, a 1D deterministic model was developed, which was numerically solved to determine the value of t_{glass} . An illustrative example of the model's output is presented in Figure 5.5, demonstrating the reduction in the radius of the drying droplet and the increase in maltodextrin concentration at the surface as the surface temperature approaches the glass transition temperature, signifying the attainment of the glassy state. The values of t_{glass} are documented in Table 5.1 for experiments that involved variations in maltodextrin type, initial concentration, and drying temperature.

5.6.2. Assumptions

The following list outlines the assumptions made in constructing the model.

- **The droplet is spherical:** Droplets may deform due to external forces, such as shear exerted by the drying air that flowing past the droplet. The droplet is assumed to be spherical, which is justified by the droplets studied being less than 1 mm, and therefore surface tension forces will be a dominant force on the droplet.
- **Dominance of diffusion in species transport within the droplet:** Within droplets, various transport mechanisms come into play. This model considers the influence of diffusion and evaporation as primary factors. In reality, additional mechanisms, such as convective currents driven by surface tension or density gradients, also play a role. For instance, rapid evaporation at contact lines is a well-known example for which such gradients play a role (Deegan et al., 1997; Edwards et al., 2018; Sadek et al., 2015). In the case of our modeled droplets, we assume a free-floating droplet without contact. Consequently, surface tension-driven flow is not considered. While density may increase locally in a droplet due to solute accumulation, it is accompanied by a substantial increase in viscosity owing to the amorphous solids present. Thus, density-driven flow is also considered negligible. Neglecting convective flows allows us to model the droplet's behavior in a one-dimensional radial direction.
- **Thin film around the droplet for average air properties:** It is assumed that there is a thin film around the droplet where the transport takes place to the air through diffusion only. An implication of this diffusive boundary layer is the presence of a linear temperature gradient between the droplet surface and the surrounding air. We use the average temperature of the boundary layer to calculate the air properties.
- **Boundary layer that describes mass and heat transfer with Sherwood and Nusselt respectively:** Similar to the earlier assumption, it is postulated that a boundary layer exists in which heat and mass transfer occur between the droplet and the surrounding air. However, it should be noted that the heat and mass profiles of the transported substances may not exhibit a linear behavior. Determining these profiles can be a complex task, but fortunately, there exist practical correlations that can characterize them. In their seminal work, Ranz and Marshall (1952) established heat and mass transfer coefficients for the drying of droplets. These coefficients are employed in conjunction with the Sherwood and Nusselt numbers to elucidate the mechanisms governing the transport of heat and mass within the boundary layer.
- **Ideal gas law to describe the density of water vapor:** Calculating the mass transfer from droplets to the drying air requires knowledge of the density of water vapor. This calculation is based on the principles of the ideal gas law.
- **Ideal mixing of water and solute species:** When different liquid species are combined, interactions between their molecules result in changes in entropy and, consequently, temperature changes during mixing. Additionally, the volume of the mixture may not remain the same. In the context of this study, we make the assumption that the liquid species form an ideal mixture. This assumption entails neglecting temperature changes caused by mixing and maintaining the sum of the species volumes constant.
- **Homogeneous temperature inside the Droplet:** The temperature profile throughout the droplet is assumed to be uniform. This assumption is grounded in the fact that liquids are significantly better conductors of heat compared to gases. Consequently, most of the heat resistance is concentrated in the gas phase surrounding the droplet. The dimensionless Biot number is a parameter that quantifies the relationship between internal and external heat resistance. According to Mills (1992), when the Biot number (Bi) is less than 0.1, it is justifiable to disregard the internal heat resistance of the droplet and, therefore, assume a homogeneous temperature distribution. The Biot number is calculated for various operational conditions in section 5.6.5 and typically falls below 0.01 in the majority of conditions encountered in single droplet drying experiments and within spray dryers.

5.6.3. Numerical method

In this section, we present the methods employed within the model. Figure 5.9 provides an overview of the calculation steps involved in simulating the drying of a droplet. The initial step involves setting up the necessary spatial grid. During this stage, we also determine the material properties of the solute. Following the initialization step, the model iterates over the time domain, executing several key steps: evaporation, shrinking, and diffusion.

In the evaporation phase, we calculate the mass transfer from the droplet to the drying air. This calculation necessitates determining the water vapor pressure at the droplet interface and the vapor pressure of the bulk drying air. The corresponding heat transfer to the droplet is also determined, as explained in Section 5.6.4.

After the water has evaporated from the droplet, it undergoes shrinkage. This process requires a reevaluation of the spatial grid to align with the new droplet geometry. The grid points shift relative to their original positions before the shrinkage. Consequently, we must reevaluate the concentration of species stored in the grid points using the cup-mix method. Using the information about heat transfer from the evaporation section and the heat capacity of the droplet, we calculate the droplet's temperature with the update geometry. These aspects are discussed in Section 5.6.5.

Once the droplet has shrunk, the final step is to determine the diffusion of species within the droplet. First, we present the discretized diffusion scheme used in the simulation. Second, the diffusion coefficient is calculated. This coefficient relies on knowledge of the droplet's viscosity, which, in turn, requires knowledge of its density. More details on diffusion-related topics can be found in Section 5.6.6.

This chapter concludes with validation methods for the simulation to assess its accuracy. Detailed discussions of these validation methods are provided in Section 5.6.7.

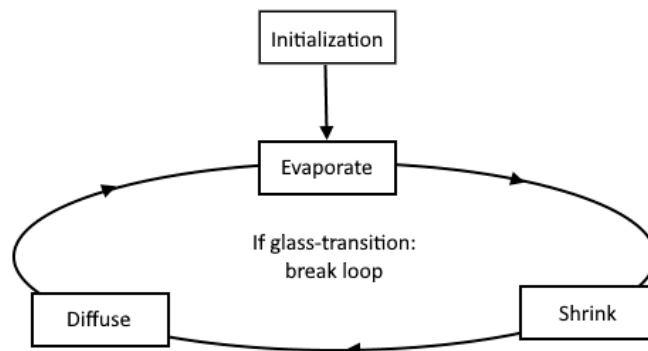


Figure 5.9: Visual presentation of the simulation steps.

Initialization

In the initialization phase, prior to commencing the drying droplet simulation, the spatial domain is created and the material properties are selected.

The spatial domain is represented by a grid composed of discrete points. We assume the drying droplet to be spherical, thus employing a spherical coordinate system for the grid. Given the droplet's angular symmetry and dominance of diffusion per the assumption in Section 5.6.2, only the radial direction is considered, resulting in a 1D grid that characterizes a 3D droplet. Careful selection of grid points is crucial. Each grid point possesses properties, including position, volume, and concentration, which are utilized and modified during the simulation. The initial point originates from the origin, while the final point resides at the interface, enabling the computation of surface properties. The grid points are evenly distributed throughout the grid, as shown in Figure 5.10 for reference.

Table 5.2: Material properties of species inside the drying droplet. Sources for maltodextrin are Meerdink (1993) and Siemons et al. (2020).

species	M (g mol ⁻¹)	T _g (K)	C _p (J kg ⁻¹ K)	dC _p (kJ kg ⁻¹)	ρ (kg L ⁻¹)
MD12	1518	425	1500	0.426	1.54
Water	18	134	4186	1.92	0.998

The material properties of the species within the droplet influence the drying process. Throughout the simulation, these properties remain constant. However, numerous parameters that rely on concentration and temperature are also impacted by these material properties, such as the glass transition temperature and the density of the mixture. The material properties of the species that are included in the model can be found in Table 5.2. The molar density of maltodextrin DE12 (MD12) was determined by equation A.1.

$$M = 162 \frac{111.11}{DE} + 18 \quad (\text{A.1})$$

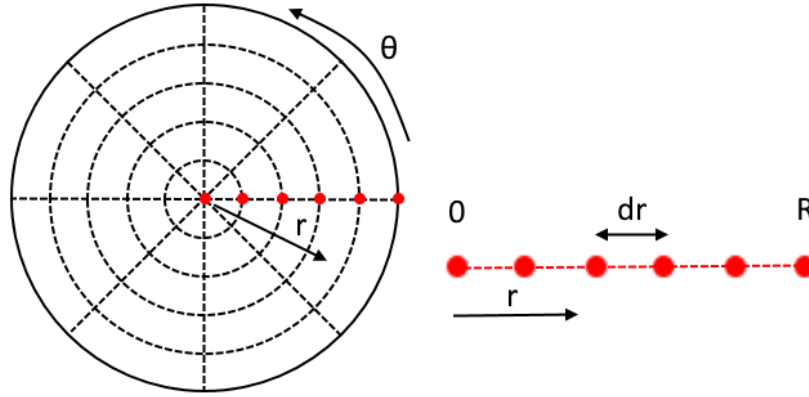


Figure 5.10: Grid points representing the spatial domain of the droplet.

5.6.4. Evaporate

In the Evaporate phase, the determination of vapor pressure occurs both within the bulk drying air and at the droplet interface. This calculation encompasses the assessment of mass and heat transfer between the droplet and the drying air. In conjunction with the humidity level of the drying air and the saturation pressure, the vapor pressure within the bulk is computed. The vapor pressure at the interface, in turn, depends on the saturation pressure, which denotes the maximum amount of water vapor that can exist in the air, and the water activity. The water activity is correlated with the relative humidity and is influenced by material properties and the surface concentration of the solute. The gradient in vapor pressure drives the mass transfer between the droplet interface and the bulk drying air, leading to the loss of water mass within the drying droplet. Analogous to mass transfer, a temperature gradient induces heat transfer, which provides the necessary energy for water evaporation. The subsequent sections delve into each of these topics in detail.

Bulk Vapor Pressure

The saturation pressure determines the maximum water content the air can hold. Once the saturation pressure is established, it can be combined with the humidity of the bulk drying air to determine the vapor pressure within the bulk phase. The saturation pressure is temperature-dependent, and its relationship with temperature is approximated using the Antoine equation as shown in equation A.2.

Table 5.3: Antoine coefficients of water (DBBST, 2023).

Range (K)	A	B	C
273.150 to 373.150	8.071 31	1730.63	233.426
373.150 to 647.096	8.140 19	1810.94	244.485

$$P_{sat} = 10^{A - \frac{B}{T+C}} \cdot \frac{133.32}{10^5} \quad (\text{A.2})$$

The Antoine equation incorporates parameters A, B, and C, which are specific to the species for which the saturation pressure is being calculated. For water, these coefficients are presented in Table 5.3 .

To validate these Antoine coefficients within the temperature range of $T = 273 \text{ K}$ to 647 K , equation A.2 is evaluated against available data on water saturation pressure at various temperatures (NIST, 2023). The accuracy of the equation is assessed using the R-squared formula presented in equation A.3, where y represents the correlated parameter, in this case, saturation pressure.

$$R^2 = 1 - \frac{\sum_i (y_i - y - model)^2}{\sum_i (y_i - y_{av})^2} \quad (\text{A.3})$$

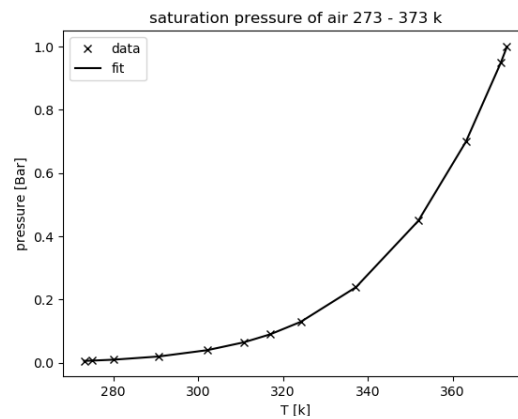
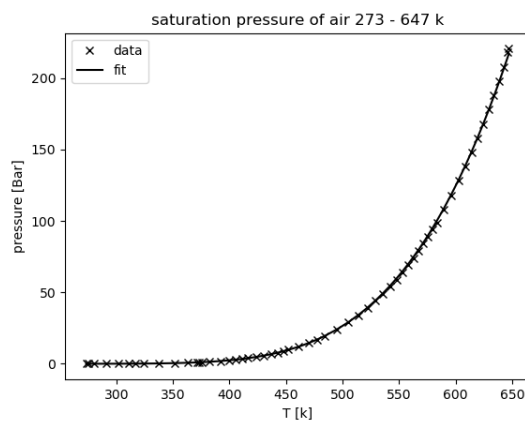
**Figure 5.11:** Antoine equation for water in the low temperature range.**Figure 5.12:** Antoine equation for water in the high-temperature range.

Table 5.4: GAB parameters for different solute species (Abramovi & Klofutar, 2002; Lin & Chen, 2006).

species	w_m	k	c
MD12	0.0510	0.92	16.91
Lactose	0.0627	1.01	2.81

Figures 5.11 and 5.12 depict the comparison between tabulated data and the Antoine equation across the specified temperature range. Notably, there is a high correlation of 0.9998 between the data and the Antoine equation over the entire temperature range, substantiating the accuracy of the saturation pressure determination.

With a reliable method now established for determining the saturation pressure of water at different temperatures, the final step involves calculating the vapor pressure within the bulk drying air (P_∞) based on the relative humidity. The relative humidity H serves as an input parameter in this model and represents the proportion of water vapor in the air relative to the maximum possible amount at a specific temperature. The equation governing the vapor pressure of the drying air is given by equation A.4.

$$P_\infty = HP_{sat} \quad (\text{A.4})$$

Interface Vapor Pressure

The vapor pressure at the interface (P_s) can be determined using the saturation pressure (P_{sat}) and the water activity (a_w) at the surface. The definition of water activity is provided in equation A.5, where a_w represents the water activity. Water activity serves as a measure of the equilibrium moisture content, with an activity of one denoting pure water.

$$P_s = a_w P_{sat} \quad (\text{A.5})$$

The relationship between equilibrium moisture content and relative humidity yields the sorption isotherm. Numerous models are available to describe this isotherm, with Basu et al. providing a comprehensive review (Basu et al., 2006). In this work, we employ the GAB model, chosen for its consistent performance across a wide range of food materials and its inclusion of a temperature term, which proves valuable in describing drying droplets at different temperatures. The GAB model is applied to lactose and MD12. The model itself is represented by equation A.6, where w denotes the ratio between water mass and solute mass, and w_m , k , and c are fitting parameters.

$$w = \frac{a_w c k w_m}{1 - 2k a_w + c k a_w + k^2 a_w^2 - c k^2 a_w^2} \quad (\text{A.6})$$

The fitting parameters for the GAB model are detailed in Table 5.4 for various solute species. To obtain the water activity from equation A.6, we employed the numerical bisection method. To validate the GAB model and the fitting parameters for MD12 and lactose, we compared the model with data from the literature, as depicted in Figure 5.13 and Figure 5.14. The correlation coefficients for MD12 and lactose are 0.9954 and 0.9958, respectively, demonstrating a highly accurate fit for both materials.

Mass Transfer

Mass transfer is responsible for the evaporation of droplets. This transfer occurs due to the vapor pressure gradient between the droplet interface and the bulk drying air. By calculating both vapor pressures as discussed in the preceding sections, we can determine the change in water mass within the droplet, as indicated by equation A.7. The mass transfer coefficient (β) is computed using the Sherwood number, using equation A.8, as suggested by Ranz and Marshall (1952).

$$m_{vap} = \rho_{vap} A \beta \frac{P_s - P_\infty}{P_{atm}} dt \quad (\text{A.7})$$

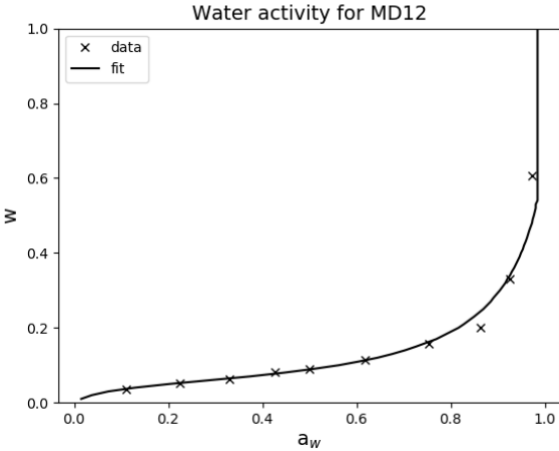


Figure 5.13: Comparison between data and the GAB model for MD12 (Darken, 1948).

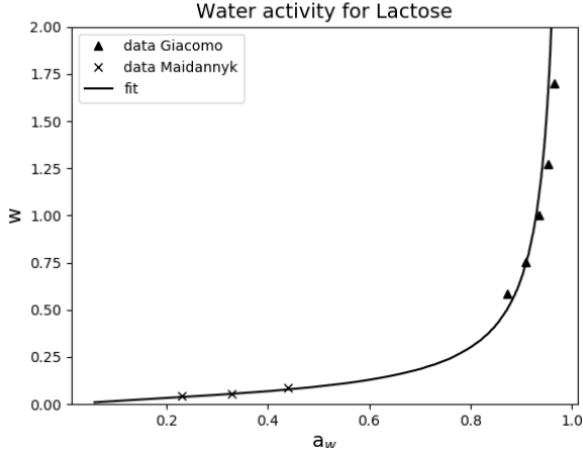


Figure 5.14: Comparison between data and the GAB model for lactose (Di Giacomo et al., 2017; Maidannyk & Roos, 2017).

$$\beta = Sh \frac{D_{vap,a}}{2R} \quad (A.8)$$

Before equations A.7 and A.8 can be solved, we must find the vapor density (ρ_{vap}), the diffusion coefficient of vapor in the air ($D_{vap,a}$), and the Sherwood number (Sh). Starting with vapor density, we employ the ideal gas law to derive equation A.9, where M represents the molar water density, and R_g is the gas constant. In simulating a drying droplet in an open system, the pressure equals atmospheric pressure (P_{atm}). The temperature is the sole variable that is not constant, with a temperature gradient existing between the interface and the bulk drying air. We use the thin-film theory to calculate the vapor density, considering the average temperature between the interface and the bulk drying air temperature.

$$\rho_{vap} = \frac{P_{atm}M}{R_gT} \quad (A.9)$$

The diffusion coefficient depends on air temperature and is described by a simple linear correlation, as shown in equation A.10.

$$D = 0.000000148500T - 0.000018880500 \quad (A.10)$$

This correlation is validated against tabulated data in Figure 5.15, where the R^2 value of 0.9993 indicates excellent agreement with the data.

The final parameter to evaluate is the Sherwood number, which correlates convective and diffusive mass transport. The Sherwood correlation is analogous to the Nusselt correlation for spheres proposed by Ranz and Marshall (1952) and depends on the Reynolds (Re) and Schmidt numbers (Sc). The Sherwood correlation is provided in equation A.11, where $Re < 200$ and $Sc < 250$.

$$Sh = 2 + 0.6Re^{0.5}Sc^{1/3} \quad (A.11)$$

$$Re = \frac{\rho u L}{\mu_{air}} \quad (A.12)$$

$$Sc = \frac{\mu_{air}}{\rho D} \quad (A.13)$$

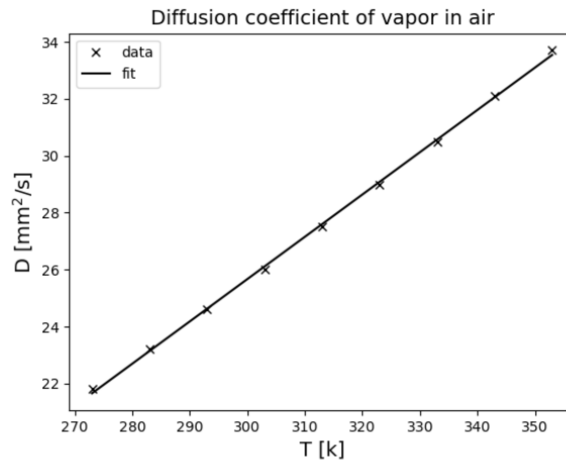


Figure 5.15: The diffusion coefficient of vapor compared to tabulated data (Bolz, 1970).

The Reynolds and Schmidt numbers necessitate the calculation of air viscosity (μ_{air}), which is temperature-dependent. We employ a second-order polynomial, as shown in equation A.14, to describe air viscosity.

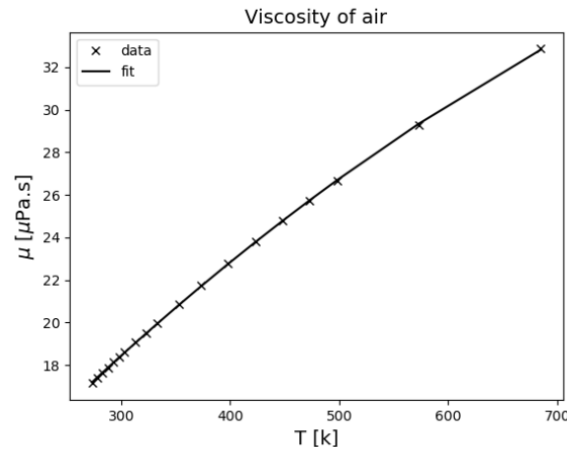


Figure 5.16: Viscosity of air plotted together with tabulated data (Engineering Toolbox, 2003)

This correlation is compared with data in Figure 5.16, demonstrating an excellent fit with a correlation coefficient of 0.9999 over a temperature range from $T = 273$ K to 685 K.

$$\mu_{air} = -0.0000000002293T^2 + 0.0000005991782T + 0.00000253901766 \quad (\text{A.14})$$

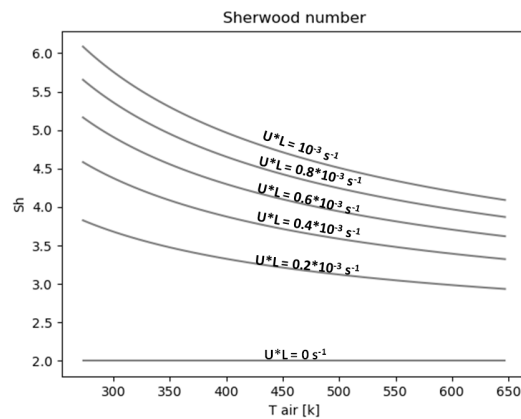


Figure 5.17: Sherwood number at different air temperatures, drying air velocities and droplet sizes. The later two parameters are combined with the product $U \cdot L$.

Finally, the Sherwood number is determined, depending on air temperature, drying air velocities, and droplet size. These latter two parameters are combined as $U \cdot L$ in the Reynolds numbers' denominator, as shown in Figure 5.17. The figure illustrates that as temperature rises, diffusion becomes more significant, leading to a decrease in the Sherwood number. Conversely, an increase in $U \cdot L$ amplifies convection, resulting in higher Sherwood numbers.

Heat transfer

Heat transfer is analogous to mass transfer and is driven by a temperature gradient between the droplet interface and the bulk drying air. The drying air temperature is an input parameter, while the interface temperature is calculated based on the previous time step, as explained in Section 5.6.5. The change in energy within the droplet is calculated using equation A.15. A heat transfer coefficient (γ) is introduced, which is a correlation based on the Nusselt (Nu) number, as proposed by Ranz and Marshall (1952).

$$E_{vap} = \gamma(T_{\infty} - T_s)Adt \quad (\text{A.15})$$

$$\gamma = Nu \frac{\lambda_{air}}{2R} \quad (\text{A.16})$$

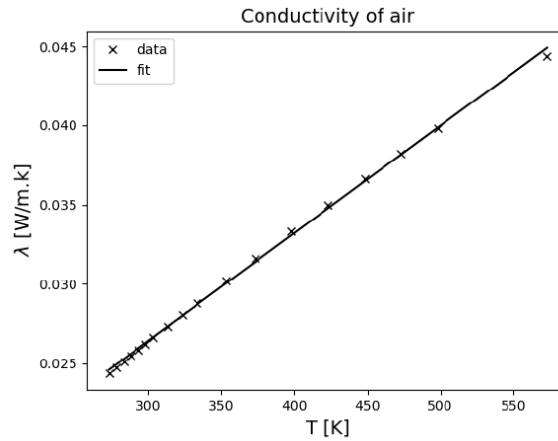


Figure 5.18: Heat conductivity of air validated with data (Engineering Toolbox, 2009)

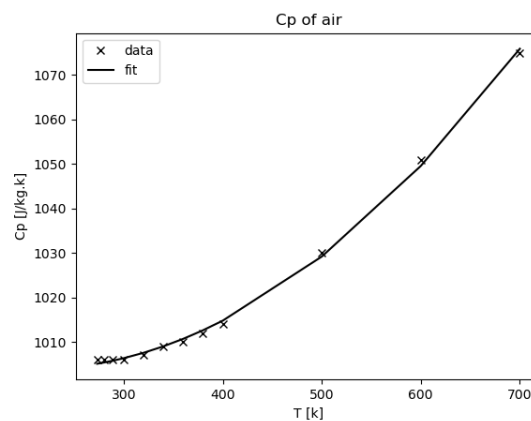


Figure 5.19: Heat capacity of air validated with data (Engineering Toolbox, 2004a)

Similar to solving mass transfer, we need to find the heat conductivity of air (λ_{air}) and the Nusselt number before we can solve equations A.15 and A.16. Air conductivity depends on temperature and is described by a linear correlation in equation A.17. The correlation's fit is validated against tabulated data in Figure 5.18, with a high R^2 value of 0.9988 over a temperature range from $T = 273$ K to 373 K.

$$\lambda_{air} = 0.000067755124T + 0.006108642996 \quad (\text{A.17})$$

The Nusselt number, correlating convective and conductive heat transfer, is provided in equation A.18 (Ranz & Marshall, 1952).

$$Nu = 2 + 0.4Re^{0.5}Pr^{1/3} \quad (\text{A.18})$$

$$Pr = \frac{\mu C_{p,air}}{\lambda_{air}} \quad (\text{A.19})$$

The Prandtl number requires knowledge of the air's heat capacity ($C_{p,air}$), which is temperature-dependent. We use a second-order polynomial, as shown in equation A.20, to describe air heat capacity. This correlation is compared with data in Figure 5.19, yielding a correlation coefficient of 0.9987 over a temperature range from $T = 273$ K to 700 K. The average temperature between the interface and bulk drying air is used to calculate the air heat capacity in the thin film.

$$C_{p,air} = 0.000298463495T^2 - 0.124554461009T + 1016.858539115300 \quad (\text{A.20})$$

The Nusselt number is determined for various temperatures, air velocities, and droplet sizes, as shown in Figure 5.20. Similar to the Sherwood number, air velocity and droplet size are combined as $U \cdot L$. An increase in temperature enhances conductivity, leading to lower Nusselt numbers. Conversely, an increase in $U \cdot L$ strengthens convection, resulting in higher Nusselt numbers.

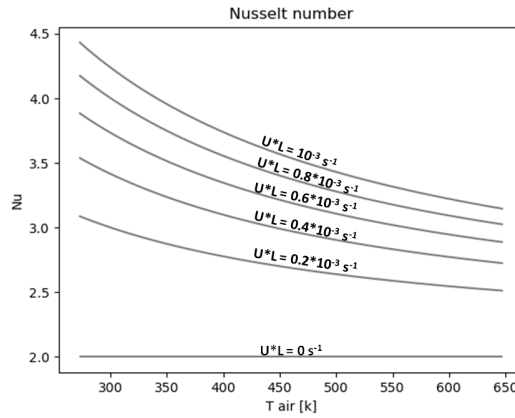


Figure 5.20: Nusselt number for different temperatures, drying velocity U and droplet size L

5.6.5. Shrink

In the shrink phase, the model computes the new geometry of the droplet. This involves recalculating the volume fraction of solute species at the grid points using cup mixing and determining the temperature of the droplet.

The new geometry is determined from the previous geometry and the evaporated mass of water. As the droplet shrinks, so does the distance between the grid points, which equally distribute over the droplet's radius. The new fractions of solute species are determined through cup mixing between adjacent grid points.

With the updated geometry, it becomes possible to determine the droplet's temperature. This calculation involves considering the heat capacity of the droplet and the amount of energy transferred to the droplet. Subsequent sections will delve into these topics.

Geometry

The geometry of the droplet, comprising surface and volume, changes as water evaporates during each time step. The amount of volume reduction in the droplet can be directly linked to the evaporated water mass. Additionally, evaporation leads to solute accumulation at the interface due to the inability of solutes to escape the droplet; they are trapped by the moving interface. Figure 5.21 illustrates how evaporating mass affects solute and water volumes.

The following equations describe the volumes depicted in Figure 5.9. First, equation A.21 calculates the total affected volume (V_{w+s}), using the evaporated mass (m_{vap}) and the water volume fraction (X_N).

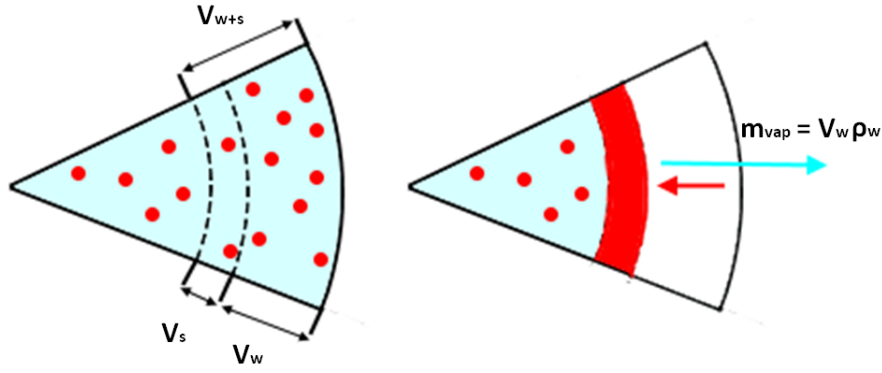


Figure 5.21: Evaporation of water at the interface of the droplet, causing the interface to move and capture solid species.

$$V_{w+s} = \frac{m_{vap}}{\rho_w X_N} \quad (\text{A.21})$$

Equations A.22 and A.23 calculate the evaporated water volume (V_w) and the volume of solute accumulated with the moving interface (V_s).

$$V_w = \frac{m_{vap}}{\rho_w} \quad (\text{A.22})$$

$$V_s = V_{w_s} - V_w \quad (\text{A.23})$$

Given the evaporated water volume, we determine the droplet volume in the current time step V_t .

$$V_t = V_{t-1} \quad (\text{A.24})$$

Finally, the geometric properties of the droplet can be derived from the it's volume using equations A.25 and A.26.

$$R_t = \left(\frac{3V_t}{4\pi}\right)^{1/3} \quad (\text{A.25})$$

$$A_t = 4\pi R_t^2 \quad (\text{A.26})$$

Since the drop now has a smaller radius than the previous time step, the grid points in the spatial domain will also change their radial position. The distance between grid points is found by dividing the radius of the drop by the number of grid points (N) as shown in equation A.27.

$$dr_t = \frac{R_t}{N} \quad (\text{A.27})$$

The grid points possess several properties, including position, volume, and volume fraction. The position is discretized, with (i) representing the radial position. While the discretized position remains constant, the distance between the points changes. The volume of grid points changes as follows:

$$V_i = \begin{cases} \frac{4}{3}\pi\left(\frac{dr}{2}\right)^3, & \text{if } i = 0 \\ \frac{4}{3}\pi\left(r_N^3 - \left(r_N - \frac{dr}{2}\right)^3\right), & \text{if } i = N \\ \frac{4}{3}\pi\left(\left(r_i + \frac{dr}{2}\right)^3 - \left(r_i - \frac{dr}{2}\right)^3\right) & \text{otherwise} \end{cases} \quad (\text{A.28})$$

The volume associated with the central grid point (V_0) equals that of a sphere with a radius of $\frac{dr}{2}$. The volume corresponding to the interface grid point (V_N) is calculated between R and $R - \frac{dr}{2}$. All other grid points between the center and the interface (V_i) are evaluated between $r_i - \frac{dr}{2}$ and $r_i + \frac{dr}{2}$. With the volume of the grid points determined, the final property of the grid points—the volume fraction of solute species—can be determined, as discussed in the next section.

Cup-mixing

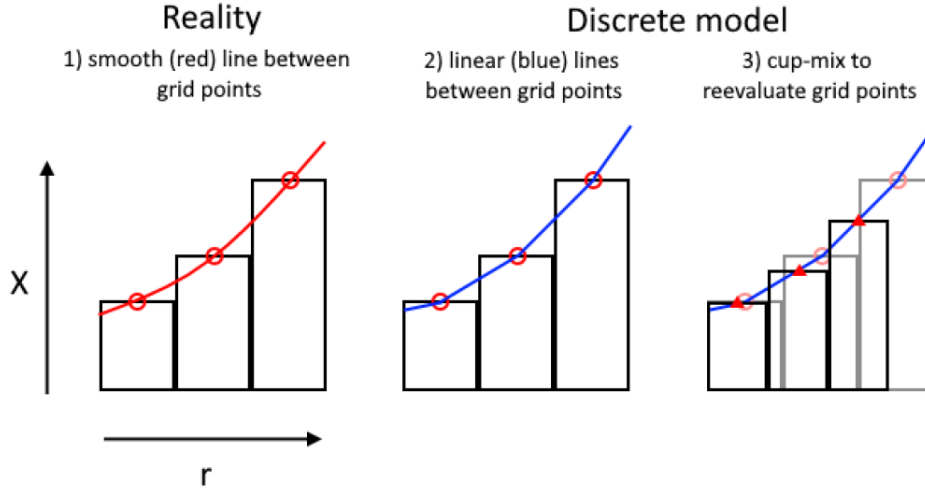


Figure 5.22: Cup-mixing explained. 1) The droplet has a concentration gradient. 2) The concentration gradient is approximated with straight lines connecting the discrete grid points. 3) When these grid points move, the concentration is evaluated by moving along the gradient.

Shrinking of the droplet affects the positions and volumes of the grid points. These grid points contain information about the volume fraction of species within the spatial domain. The principle of cup-mixing is illustrated in Figure 5.22. In reality, a smooth concentration gradient of species exists across the droplet, represented by the red line in the figure. However, due to the model's discrete spatial positions, this gradient is approximated by connecting adjacent grid points with straight blue lines. When grid points change position, the corresponding concentration can be calculated by following the concentration gradient between two previous grid points. This process is referred to as 'cup-mixing' because it resembles the mixing of volumes and associated concentrations to derive a new concentration.

Cup-mixing also has implications for the grid point at the interface when the droplet shrinks. Specifically, the volume of grid points at the interface is mixed with the solute volume (V_s) collected by the moving interface. This assumption holds under certain conditions. Within a time step, solids are collected by the moving interface while also being dispersed by diffusion. As long as diffusion within the volume associated with the interface occurs on a smaller timescale than the movement of the interface, it can be assumed that the volume is well-mixed because diffusion dominates. This condition is expressed in equation A.29, where the right-hand side represents the velocity of the interface. This underscores the importance of a suitably small grid to accurately describe transport phenomena at the droplet interface and achieve convergence in numerical simulations. Details on the suitability of the grid steps are presented in equation 5.6.7.

$$\frac{2D}{\Delta r} \gg \frac{R_t - R_{t-1}}{dt} \quad (\text{A.29})$$

Using the cup mixing method, the water volume fraction associated with each grid point is calculated as follows:

$$X_{i,t} = \begin{cases} X_{i,t-1}, & \text{if } i = 0 \\ X_{N,t}, & \text{if } i = N \\ \frac{(V_{i,t} - \Delta V_{i,t})X_{i,t-1} + \Delta V_{i,t}X_{i-1,t-1}}{V_{i,t}}, & \text{otherwise} \end{cases} \quad (\text{A.30})$$

The term V_i represents the volume shifted inward at each grid point and accounts for the overlap between the volume of a new grid point and that of an adjacent old grid point. The concentration in the center ($X_{0,t}$) is not affected in this simulation step because the volume shrinks inward without overlapping with volumes of other grid points. The volume fraction at the interface ($X_{N,t}$) is determined by mixing with the neighboring grid point and the solute volume (V_s), as expressed in equation (A.31).

$$X_{i,t} = \begin{cases} \frac{(V_{N,t} - V_{s,t})X_{N-1,t-1}}{V_{N,t}}, & \text{if } (V_{N,t} - \Delta V_{N,t} - V_{s,t}) < 0 \\ \frac{(V_{N,t} - \Delta V_{N,t} - V_{s,t})X_{N,t-1} + \Delta V_{N,t}X_{N-1,t-1}}{V_{N,t}}, & \text{otherwise} \end{cases} \quad (\text{A.31})$$

Temperature of the droplet

The temperature of the droplet changes due to the evaporation of water at the interface, which extracts energy from the droplet, and heat transfer from the surrounding air, which supplies energy to the droplet. The balance between evaporation and heat transfer results in a change in the droplet's energy and, consequently, a change in its temperature. To determine the change in the droplet's temperature, it is required to calculate the heat capacity of the droplet.

In summary, to determine the droplet's temperature change, the energy balance between evaporating water and heat transfer from the air is resolved, as shown in equation A.32. Before calculating the temperature, it is necessary to determine the droplet's heat capacity. This heat capacity depends on the species mixture and is calculated as the sum of each species' heat capacities weighted by their mass fractions, considering the concentration gradient within the droplet. Finally, the temperature change is calculated by dividing the energy difference by the droplet's heat capacity, as given in equation A.34. The next step involves determining the droplet temperature by resolving the energy balance between evaporating water and heat transfer from the surrounding air, as depicted in equation A.32.

$$\Delta E = E + vap - m_{vap}H_{vap} \quad (\text{A.32})$$

To find the droplet's temperature, the droplet's heat capacity is determined. This heat capacity depends on the species mixture and can be calculated as the sum of each species's heat capacities, weighted by the mass fraction of that species. Since there exists a concentration gradient of species within the droplet, the capacity at each grid point must be evaluated and summed to obtain the total heat capacity. Each grid point is weighted by the corresponding volume V_i , as shown in equation A.33:

$$CP = \sum_i (X_{mw,i}C_{pw} + X_{ms,i}C_{ps})V_i \quad (\text{A.33})$$

The final step to determine the change in droplet temperature is to divide the energy difference by the droplet's heat capacity, as given in equation A.34.

$$\Delta T = \frac{\Delta E}{CP} \quad (\text{A.34})$$

5.6.6. Diffuse

In the Diffuse phase, the density, viscosity, and diffusion coefficient are determined. First, we present the discretized diffusion scheme used to calculate the Fickian diffusion within the droplet.

Diffusion Scheme

The diffusion scheme calculates concentration changes over both spatial and temporal domains. These changes result from concentration gradients induced by water evaporation at the interface. The rate of species diffusion is determined by the diffusion coefficient, which can vary with temperature and concentration. This variability is particularly crucial in capturing drying phenomena near the droplet interface, where high concentrations are prevalent. As a result, the diffusion scheme must account for concentration-dependent diffusion coefficients. Versypt and Braatz (2014) conducted a comprehensive analysis of different diffusion schemes, including those accommodating concentration-dependent diffusion coefficients. The outcomes of their study guided the selection of the most suitable scheme for this model. This section proceeds to discuss the derivation and optimization of the discretized scheme.

Within this section, two notations are employed for the spatial domain. The first notation is found in the partial differential equations, which utilize the radial coordinate r and its location on the interface denoted as R . The second notation for the spatial domain is utilized within the discretized scheme, where the index i describes the position, with $i = 0, 1, 2, \dots, N$, where 0 represents the center and N denotes the final index position representing the interface.

The starting point for a diffusion scheme is the species balance. In this study, Fickian diffusion in spherical coordinates is employed to model diffusion within a droplet. Due to the droplet's symmetry, only radial diffusion is considered. The species balance equation is shown in equation A.35. The subsequent step involves expanding this partial differential equation (PDE), resulting in equation A.36.

$$\frac{dc}{dt} = \frac{1}{r^2} \frac{d}{dr} \left(r^2 D \frac{dc}{dr} \right) \quad (\text{A.35})$$

$$\frac{dc}{dt} = \frac{2D}{r} \frac{dc}{dr} + \frac{d}{dr} \left(D \frac{dc}{dr} \right) \quad (\text{A.36})$$

The extended PDE is solved alongside two boundary conditions to derive the final discretized scheme describing diffusion in the center, body, and interface of the droplet. At the center of the droplet, a point of symmetry exists, while at the interface, a no-flux condition prevails. These two boundary conditions are valid throughout the entire time domain.

$$\frac{dc(0, t)}{dr} = 0 \quad (\text{A.37})$$

$$\frac{dc(R, t)}{dr} = 0 \quad (\text{A.38})$$

Discretization at the Center

The discretization process commences with the extended PDE in equation A.36. Ford Versypt suggests that instead of modifying the scheme at the center of the droplet, the PDE can be simplified by taking the limit as the radius approaches zero:

$$\frac{dc(0, t)}{dt} = \lim_{r \rightarrow 0} \left(\frac{2D}{r} \frac{dc}{dr} + \frac{d}{dr} \left(D \frac{dc}{dr} \right) \right) = 3D \frac{d^2c}{dr^2} \quad (\text{A.39})$$

The central finite difference approximation is then applied to equation A.39, where A_i represents the discrete diffusion at position i :

$$\frac{3D}{\Delta r^2} \delta_r (\delta_r c(r_0, t)) = \frac{3D}{\Delta r^2} \delta_r \left(c(r_0 + \frac{\Delta r}{2}, t) - c(r_0 - \frac{\Delta r}{2}, t) \right) \approx \frac{3A_0}{\Delta r} (C_1 - 2C_0 + C_{-1}) \quad (\text{A.40})$$

This equation must satisfy the boundary condition at the center, as shown in equation A.41:

$$\frac{dc(r_0, t)}{dr} = \frac{\delta_2 c(r_0, t)}{2\Delta r} \approx \frac{C_1 - C_{-1}}{2\Delta r} = 0 \quad (\text{A.41})$$

From this boundary condition, it follows that C_1 must be equal to C_{-1} . Combined with equation A.40, this leads to the final scheme at $r = 0$ as shown in equation A.42:

$$\frac{dC_0}{dt} = \frac{6A_0(C_1 - C_0)}{\Delta r^2} \quad (\text{A.42})$$

Discretization at the Interface

The discretization at the interface is analogous to that at the center. First, the PDE in equation A.36 is simplified. The radial position on the interface is much larger than the step size ($R \gg \Delta r$). Consequently, the first term on the right becomes negligible compared to the second term, resulting in equation A.43:

$$\frac{dc(R, t)}{dt} = \lim_{r \rightarrow R} \left(\frac{2D}{r} \frac{dc}{dr} + \frac{d}{dr} \left(D \frac{dc}{dr} \right) \right) = D \frac{d^2c}{dr^2} \quad (\text{A.43})$$

Similar to the discretization at the center, the central finite difference approximation is applied to equation A.43:

$$\frac{D}{\Delta r^2} \delta_r (\delta_r c(R, t)) = \frac{D}{\Delta r^2} \delta_r \left(c(r_N + \frac{\Delta r}{2}, t) - c(r_N - \frac{\Delta r}{2}, t) \right) \approx \frac{A_N}{\Delta r^2} (C_{N+1} - 2C_N + C_{N-1}) \quad (\text{A.44})$$

The boundary condition must also be satisfied here:

$$\frac{dc(R, t)}{dr} = \frac{\delta_2 c(R, t)}{2\Delta r} \approx \frac{C_{N+1} - C_{N-1}}{2\Delta r} = 0 \quad (\text{A.45})$$

Hence, $C_{N+1}(t) = C_{N-1}(t)$. Combining this with equation A.44 results in the final scheme at $r = R$ as shown in equation A.46:

$$\frac{dC_N}{dt} = \frac{2A_N(C_{N-1} - C_N)}{\Delta r^2} \quad (\text{A.46})$$

Discretization of the bulk region also originates from equation A.36. The central finite difference approximation is applied, leading to the final scheme describing diffusion for all points between $0 < r < R$ (Versypt & Braatz, 2014):

$$\frac{dC_i}{dt} = \frac{A_i}{2i\Delta r^2} ((i+2)C_{i+1} - (i-2)C_{i-1}) + \frac{A_{i+1}}{2\Delta r^2} (C_{i+1} - C_i) + \frac{A_{i-1}}{2\Delta r^2} (C_{i-1} - C_i) \quad (\text{A.47})$$

Complete Scheme

The following equation combines the center, bulk, and interface schemes. An adjustment has been made to express the equation in terms of volume fraction X , rather than concentration C . The gradient is the driving force for diffusion, and it is irrelevant whether the gradient is composed of moles, mass fractions, or volume fractions. The advantage of using this volume fraction equation is that it accounts for variations in density within the droplet, which may not be constant or homogeneous. Utilizing effective diffusion coefficients for the species mixture and assuming an ideal liquid mixture, the volume diffusion of one species is equal to the opposite volume flux of the other species. This approach implies that volume transfer only needs to be calculated for one of the two species.

$$\frac{dX_i}{dt} = \begin{cases} \frac{6A_0(X_1 - X_0)}{\Delta r^2}, & \text{if } i = 0 \\ \frac{2A_n(X_{N-1} - X_N)}{\Delta r^2}, & \text{if } i = N \\ \frac{A_i}{2\Delta r^2}((i+2)X_{i+1} - 2i(X_i) + (i-2)X_{i-1}) + \frac{A_{i+1}}{2\Delta r^2}(X_{i+1}) + X_i + \frac{A_{i-1}}{2\Delta r^2}(X_{i-1}) + X_i & \text{otherwise} \end{cases} \quad (\text{A.48})$$

Density calculation

The density of the solution depends on the concentration of the solute. Diffusion causes the concentration to change and, consequently, alters the density. In the case of a non-ideal mixture, the correlation between concentration and volume is non-linear. The volume of grid points would change during diffusion, resulting in an irregular spacing between points. Alternatively, the position of grid points could be adjusted while diffusion occurs. To model the change in density without modifying the fundamentals of the diffusion scheme and the spatial grid, we assume the mixture to be ideal. An implication of this assumption is the presence of a linear correlation between the volume fraction and density, as shown in equation A.49, where X_s represents the solute volume fraction.

$$\rho_{mix} = X_s(\rho_s - \rho_w) + \rho_w \quad (\text{A.49})$$

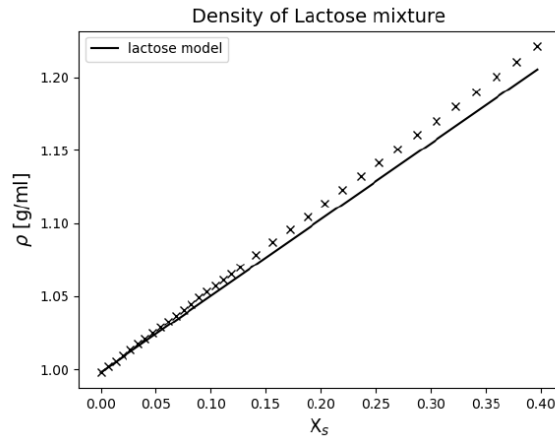


Figure 5.23: Density of lactose mixture, comparison between correlation and data (McDonald & Turcotte, 1948).

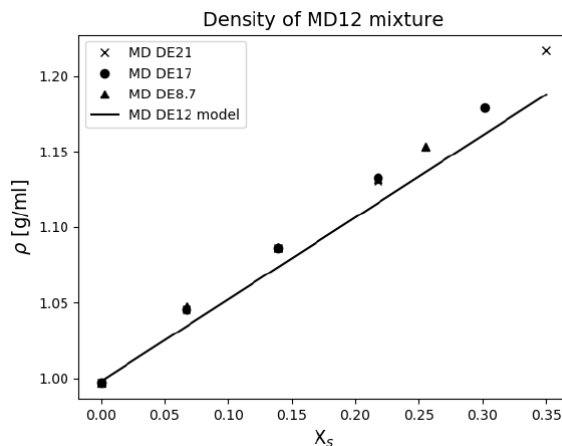


Figure 5.24: Density of MD12 mixture, comparison between correlation and data (Neri et al., 2011).

The correlation was assessed for lactose and maltodextrin. In the work of McDonald and Turcotte (1948), data for lactose at ambient conditions were collected. This data is compared with the correlation

in Figure 5.23. The R^2 of 0.9842 shows that it is a decent fit. The correlation becomes less accurate when the volume fractions of water and solute are comparable. Neri et al. (2011) collected data for maltodextrins that were compared to the correlation in Figure 5.24. The correlation used was for MD12, while the available data was for MD8.7, MD17, and MD21 under ambient conditions. The figure shows that the density of the mixture is independent of the chain length of maltodextrin. Therefore, it is still meaningful to compare this data with a correlation for MD12. With an R^2 of 0.9525, it shows a decent fit between data and correlation. As with the lactose density, the difference between maltodextrin and data is also greatest when the volume fraction of solute is similar to the volume fraction of water and more appropriate at low concentrations.

Viscosity calculation

The viscosity is necessary for calculating the diffusion coefficient within the droplet. The viscosity of the mixture varies with changes in solute concentration, density, and temperature. There are several models in the literature that describe viscosity, and these models perform well either at low concentrations or high concentrations.

This section first delves into viscosity within both regimes and subsequently assesses the correlation function between the low and high viscous models, as suggested by Both et al. (2019).

In the low concentration regime, we employ the Spurlin-Martin-Tennents (SMT) model (1946). The SMT model is shown in equation A.50. Where k_H is the Huggings parameter, $\mu_{w,T}$ is the viscosity of water, η is the intrinsic viscosity, ρ_{mix} the density of the mixture and X_{mw} the water mass fraction.

$$\mu_{SMT} = (([\eta](1 - X_{mw})\rho_{mix})e^{k_H[\eta](1 - X_{mw})\rho_{mix}} + 1)\mu_{w,T} \quad (\text{A.50})$$

To calculate viscosity using the SMT model, the k_H must be determined. In this context, it serves as a fitting parameter for each solute species. The viscosity of water is described by a third-order polynomial correlation, as shown in equation (A.51).

$$\mu_{w,T} = (-0.000002216134T^3 + 0.002313106525T^2 - 0.809475788245T + 95.354362060802) \cdot 10^3 \quad (\text{A.51})$$

The correlation is compared with tabulated data in Figure 5.24. With an R^2 of 0.9995, it can be concluded that the correlation fits the data exceptionally well. The intrinsic viscosity is the final parameter necessary to calculate the viscosity via the SMT model. We determine the intrinsic viscosity using the Mark Houwink relationship, shown in equation A.52, where M_w is the molecular weight of the solute. The parameters K and α are also fitting parameters dependent on the solute species.

$$[\eta] = KM_w^\alpha \quad (\text{A.52})$$

In the high solute regime, the William-Landl-Ferry (1955) model is used to describe the viscosity, as shown in equation A.53. Here, $C1 = 17.4$ and $C2 = 51.6$ are universal parameters, g is the universal viscosity at the glass transition of 10×10^{12} Pa s and T_g is the glass transition temperature of the solution.

$$\log \frac{\mu_{wlf}}{\mu_g} = \frac{-C1(T - T_g)}{C2(T - T_g)} \quad (\text{A.53})$$

The T_g of the mixture depends on the T_g of the solute and the water, as well as their concentration. The Gordon Taylor equation is used to predict T_g (Gordon & Taylor, 1952), as shown in equation A.54. The parameter κ depends on the ratio of the change in heat capacity at T_g , as found in equation A.55.

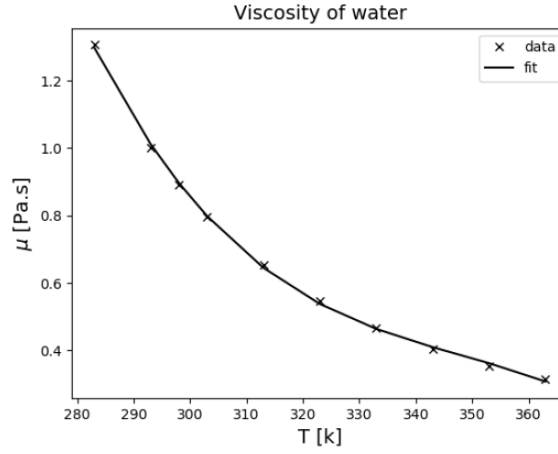


Figure 5.25: The correlation for the viscosity of water is compared to data (Engineering Toolbox, 2004b).

Table 5.5: Fitting parameters required in the viscosity model for MD12.

species	K_h	K	α	P_0	P_1	R^2 $T = (293 \text{ K})$
MD12	5.30	2.47×10^{-3}	0.267	0.7	0.043	0.9951

$$T_g = \frac{X_{ms}T_{g1} + \kappa(1 - X_{ms})T_{g2}}{X_{ms} + \kappa(1 - X_{ms})} \quad (\text{A.54})$$

$$\kappa = \frac{\Delta C_{p2}}{\Delta C_{p1}} \quad (\text{A.55})$$

Concentration is determined for both the low and high concentration regimes. Therefore, we employ a correlation function proposed by Both et al. (Both et al., 2019) to combine the SMT and WLF models. The correlation function can be found in equation A.56. The parameter P_0 is a fitting parameter between 0 and 1, determining the concentration at which the transition between models occurs. The parameter P_1 is another fitting parameter affecting the smoothness of the transition between the two models.

$$\mu = \left(1 - \frac{1}{1 + e^{\frac{X_{ms} - P_0}{P_1}}}\right) \mu_{SMT} + \frac{1}{1 + e^{\frac{X_{ms} - P_0}{P_1}}} \mu_{wlf} \quad (\text{A.56})$$

We calculate the fitting parameters used in the viscosity models for MD12 and lactose. Table 5.5 provides an overview of all the fitting parameters discussed in this section. The table also includes the correlation of the model with literature data, which was determined on a logarithmic basis.

Using the fitting parameters from Table 5.5 with equation A.56, the results are obtained and shown in Figure 5.26 and Figure 5.27. The literature data for MD12 was obtained from Dokic et al. (1998) and Both et al. (2019), which is also shown in Figure 5.26. The WLF and SMT models are plotted along with the data and the correlation function for MD12. The figure shows that the SMT model is only valid in the dilute regime, with the WLF model becoming more accurate in a high concentration regime. The correlation function also allows for the calculation of viscosity at different temperatures. The figure shows the viscosity of MD12 at $T = 323 \text{ K}$ as the yellow line. Although MD12 data for this temperature is missing, small temperature differences are incorporated by the correlation function. The lactose dataset can be used to evaluate how well the temperature is described. From this, it can be concluded that small temperature differences are well captured with the correlation function.

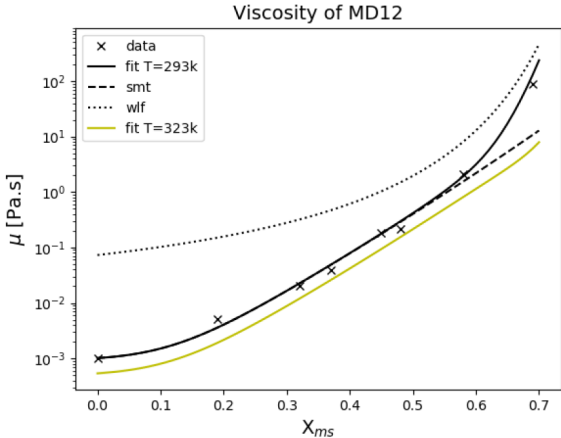


Figure 5.26: The correlation function of MD12 compared with data from Dokic et al. (1998) and Both et al. (2019). The SMT and WLF models are included.

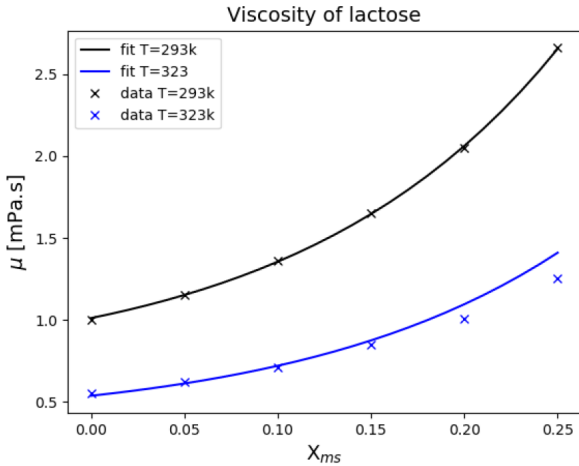


Figure 5.27: Data from Morison and Mackay (2001) compared with the correlation function of lactose for different temperatures.

Diffusion coefficient calculation

With the known density of the mixture and a model describing viscosity under varying conditions of temperature, density, and concentration, it becomes feasible to ascertain the diffusion coefficient employed in the discrete diffusion scheme. Several models are available for the diffusion coefficient, with Malafronte et al. (2015) having evaluated effective diffusion using these models and concluding that the theory of free volume (FV) offers the most accurate representation. Consequently, the FV model was selected to describe effective diffusion within this study. The FV theory posits that free volume plays a significant role in influencing the diffusion coefficient. The volume is divided into molecules and free space, and the free volume undergoes fluctuations, resulting in the formation of holes through which particles can pass. Perdana et al. (2014) determined the parameters for the FV model across a wide range of carbohydrate-water systems, including MD6 and lactose. This research served as the foundation for the diffusion model employed in this thesis. Perdana's findings suggested that the diffusion coefficients for different carbohydrates exhibit analogies. Consequently, the parameters for the studied carbohydrate systems were found to be the same as those for a sucrose-water system. This insight proves highly useful, simplifying the modeling of various species using these parameters. The diffusion model involves a mixture of two species, utilizing their volume fractions and self-diffusivities to calculate the mutual diffusion coefficient. The correlation used to describe the mixture is the generalized Darken relationship (Darken, 1948; Krishna & Van Baten, 2005), as shown in equation A.57. Where Q is the thermodynamic factor found in equation A.58, X is the volume fraction of water, and χ is the Flory-Huggins interaction parameter.

$$D = ((1 - X)D_{self,w} + (XD_{self,s}))Q \quad (\text{A.57})$$

$$Q = 1 - 2\chi X(1 - X) \quad (\text{A.58})$$

To compute the effective diffusion, one must determine both the self-diffusion coefficient of water and the solute. The self-diffusion of water can be derived from the work of Vrentas and Duda (1977), which applied the theory of free volume as shown in equation A.59. Where K_1 and K_2 are free volume parameters, D_0 the pre-exponential diffusion factor, ζ the polymer-solvent ratio, V^* the specific critical free volume and ψ the overlap factor of free volume.

$$D_{self,w} = D_0 \exp\left(-\frac{E_{mol}}{RT} - \frac{X\rho_w V_w^* + (1 - X)\rho_s \zeta V_s^*}{X\rho_w \frac{K_{1,w}}{\psi} (K_{2,w} - T_{g,w} + T) + (1 - X)\rho_s \frac{K_{1,s}}{\psi} (K_{2,s} - T_{g,s} + T)}\right) \quad (\text{A.59})$$

The self-diffusion of the solute species is described using the Stokes-Einstein relationship, as shown in Equation A.60, where r_h represents the hydrodynamic radius.

$$D_{self,s} = \frac{K_b T}{6\pi\mu r_h} \quad (\text{A.60})$$

Effective diffusion can be calculated using both self-diffusion coefficients. The parameters employed in the VF model for sucrose and water are provided in Table 5.6. The parameters for sucrose are also applicable to other hydrocarbons.

The parameters are utilized to compute the diffusion coefficient using the VF model. Figure 5.28 displays the modeled diffusion coefficient of lactose compared to data from Perdana. Two sets of data for lactose at 70 °C are presented. The model correlates with these data sets at 0.7089 and 0.8076, respectively. Although there is a noticeable difference between the measurements, the model generally fits well. Figure 5.29 illustrates the diffusion coefficient of MD12 at various temperatures. As depicted, diffusion increases at higher temperatures, and the glass transition occurs at higher concentrations as expected. Perdana compared the model with data for MD DE6, revealing that the correlation is strong at a temperature of 50 °C, but decreases at higher and lower temperatures. The VF model's advantage lies in its ability to account for temperature variations across a relatively wide range, contributing to a more accurate simulation.

Table 5.6: Parameters used in the VF model. Data was obtained from different works (Schultz & Solomon, 1961; Van Der Smán & Meinders, 2013; Vrentas & Duda, 1977)

parameter	water	sucrose
ρ kg m ⁻¹	1	1.54
T_g K	134	333
V^* L kg ⁻¹	0.91	0.59
D_0 m ² s ⁻¹	148×10^{-7}	-
E J mol ⁻¹	2.34×10^3	-
ξ	-	0.8
ζ	-	0.79
r_h m	-	0.5×10^{-9}
$\frac{K_1}{\psi}$ L kg ⁻¹ K	1.945×10^{-3}	0.366×10^{-3}
K_2 K	-19.73	69.21

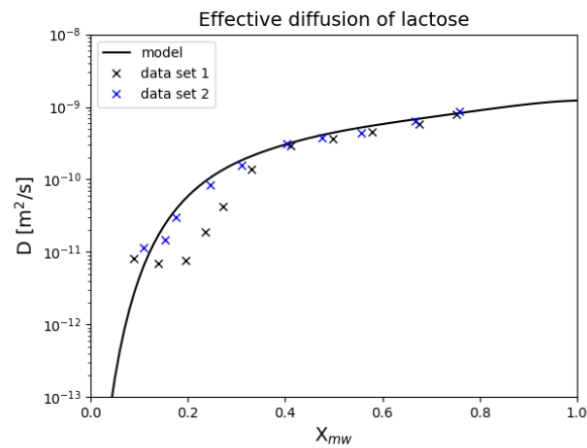


Figure 5.28: Diffusion coefficient of Lactose compared to data (Perdana et al., 2014). The data is given in duplicate.

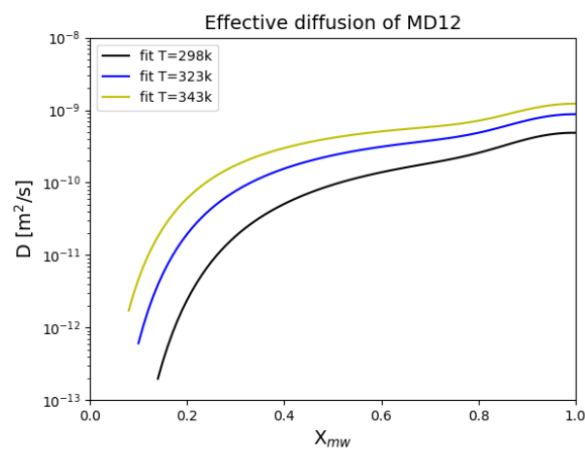


Figure 5.29: Diffusion coefficient of maltodextrins at different temperatures.

5.6.7. Validation

In this final section, we will discuss two methods employed to validate the model's outcomes. The first validation method relies on the conservation of mass theorem, which asserts that the dissolved mass within the droplet cannot vanish or escape from it. In numerical simulations, there is a risk of mass disappearing or emerging due to numerical diffusion. Consequently, a validation procedure becomes essential. The second validation method involves comparing the droplet's surface area with an analytical solution based on the d2-law. Additionally, an analysis of step-size for time steps is also presented in this section.

Conservation of mass

The conservation of mass theorem is grounded in the principle that dissolved species are constrained within the droplet, necessitating the constant preservation of the total solute mass. This theorem is instrumental in validating the model and detecting potential instances of numerical diffusion during simulation. For instance, in methods like the cup-mix approach, the movement of points and the re-evaluation of concentration may result in slight alterations in the total solute mass, which can accumulate into significant mass loss. Conversely, it can also signal problems within the diffusion scheme. The application of this theorem during evaluation ensures that the model remains free from numerical complications.

In the initialization phase before simulation commencement, the total dissolved mass is initially determined by summing the volume fraction of each grid point weighted by the volume of that grid point, as represented in equation A.61 where $t = 0$.

$$m_{tot} = \rho_s \sum_i ((1 - X_{i,t}) V_{i,t}) \quad (\text{A.61})$$

This process is repeated at each time step and compared to the total dissolved mass. This can be found in equation A.62, where $t = 0, 1, 2, \dots$ and \tilde{m} is the normalized mass.

$$\tilde{m}_t = \frac{\rho_s \sum_i ((1 - X_{i,t}) V_{i,t})}{m_{tot}} \quad (\text{A.62})$$

d2-law

The d2-law serves as an analytical solution applicable to the initial drying phase of drying droplets. Law (1982) developed this law while investigating the first drying regime. He observed a constant evaporation flux in this regime, leading to a linear reduction in the droplet's surface area. This insight is valuable for validating the drying speed by comparing the observed surface area with the predictions of the d2-law. However, it's important to note that the d2-law has its limitations. It assumes the diffusion-restricted regime and can only validate drying droplet simulations in the absence of convective airflow. During simulations, the d2-law can be employed to assess drying rates and equilibrium temperatures, providing valuable insights into the model's performance.

Step-size

The step size in both the spatial and temporal domains plays a crucial role in determining the convergence of the simulation.

Figures 5.30 and 5.31 illustrate the impact of the number of radial grid divisions and the time step size on convergence. These effects are demonstrated through a case study involving lactose droplets with the following parameters: droplet radius ($R = 100 \mu\text{m}$), mass fraction ($X_{ms} = 0.3$), humidity ($H = 0\%$), velocity ($u = 0.3 \text{ m s}^{-1}$), and temperature ($T = 333 \text{ K}$). The benchmark for assessing convergence is the time it takes for the droplet to initiate the glass transition.

In Figure 5.30, it is evident that as the number of radial divisions increases, the time required for the interface to reach the glass transition converges towards a consistent solution. However, beyond a certain

point, increasing the number of radial divisions has a diminishing effect on improving the solution while significantly increasing computational time.

Figure 5.31 reveals that smaller time steps initially exert a substantial influence on the simulation. When the time step exceeds $20\ \mu\text{s}$, the simulation cannot be completed due to the possibility of a sharp increase in mass transfer during diffusion, leading to concentration runaway. Nevertheless, if mass transfer remains minimal, further reduction of the time step does not significantly enhance simulation convergence. Thus, it is essential to determine optimal settings for both the time and spatial domains in each case study, ensuring convergence to a unique solution while minimizing computational time.

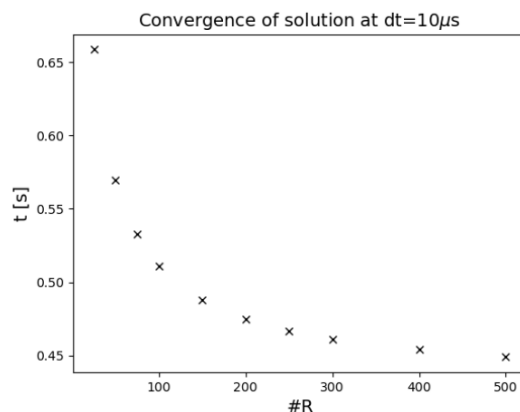


Figure 5.30: Effect of the number of divisions of the spatial domain on the convergence of the simulation.

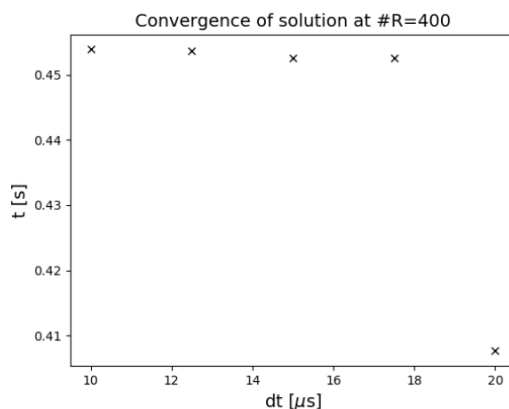


Figure 5.31: Effect of the time step size on the convergence of the simulation.

Bibliography

- Abramovi, H., & Klofutar, C. (2002). Water adsorption isotherms of some maltodextrin samples. *Acta Chim. Slov*, 49, 835–844.
- Adhikari, B., Howes, T., Bhandari, B. R., & Truong, V. (2001). Stickiness in foods: A review of mechanisms and test methods. *International Journal of Food Properties*, 4(1), 1–33. <https://doi.org/10.1081/jfp-100002186>
- Adhikari, B., Howes, T., Bhandari, B. R., & Truong, V. (2003). In situ characterization of stickiness of sugar-rich foods using a linear actuator driven stickiness testing device. *Journal of Food Engineering*, 58(1), 11–22. [https://doi.org/10.1016/s0260-8774\(02\)00328-x](https://doi.org/10.1016/s0260-8774(02)00328-x)
- Adhikari, B., Howes, T., Shrestha, A. K., & Bhandari, B. R. (2007). Development of stickiness of whey protein isolate and lactose droplets during convective drying. *Chemical Engineering and Processing: Process Intensification*, 46(5), 420–428. <https://doi.org/10.1016/j.cep.2006.07.014>

- Adhikari, B., Howes, T., Lecomte, D., & Bhandari, B. R. (2005). A glass transition temperature approach for the prediction of the surface stickiness of a drying droplet during spray drying. *Powder Technology*, *149*(2-3), 168–179. <https://doi.org/10.1016/j.powtec.2004.11.007>
- Basu, S., Shivhare, U. S., & Mujumdar, A. S. (2006). Models for sorption isotherms for foods: A review. *Drying technology*, *24*(8), 917–930. <https://doi.org/10.1080/07373930600775979>
- Bolz, R. E. (1970). *Handbook of tables for applied engineering science*. Chemical Rubber Company. <https://doi.org/10.1201/9781315214092>
- Both, E. M., Siemons, I., Boom, R. M., & Schutyser, M. A. I. (2019). The role of viscosity in morphology development during single droplet drying. *Food Hydrocolloids*, *94*, 510–518. <https://doi.org/10.1016/j.foodhyd.2019.03.023>
- Darken, L. S. (1948). Diffusion, mobility and their interrelation through free energy in binary metallic systems. *Trans. Aime*, *175*, 184–201.
- DBBST. (2023). Saturated vapor pressure. <http://ddbonline.ddbst.de/AntoineCalculation/%20AntoineCalculationCGI.exe?component=Water%EF%BF%BD>
- Deegan, R. D., Bakajin, O., Dupont, T. F., Huber, G., Nagel, S. R., & Witten, T. A. (1997). Capillary flow as the cause of ring stains from dried liquid drops. *Nature*, *389*(6653), 827–829. <https://doi.org/10.1038/39827>
- Di Giacomo, G., Scimia, F., & Taglieri, L. (2017). Cost-effective disposal of milk whey ii: Recovery and purification of lactose and pure water from the diafiltration permeate stream. *Desalination and Water Treatment*, *1*, 4. <https://doi.org/10.5004/dwt.2017.20377>
- Dokic, P., Jakovljevic, J., & Dokic-Baucal, L. (1998). Molecular characteristics of maltodextrins and rheological behaviour of diluted and concentrated solutions. *Colloids and Surfaces A: Physicochemical and Engineering Aspects*, *141*(3), 435–440. [https://doi.org/10.1016/s0927-7757\(97\)00118-0](https://doi.org/10.1016/s0927-7757(97)00118-0)
- Edwards, A. M. J., Atkinson, P. S., Cheung, C. S., Liang, H., Fairhurst, D. J., & Ouali, F. F. (2018). Density-driven flows in evaporating binary liquid droplets. *Physical Review Letters*, *121*(18), 184501. <https://doi.org/10.1103/physrevlett.121.184501>
- Elesini, U. S., Leskovek, M., Bernik, S., umiga, B., & Urbas, R. (2016). Influence of co-current spray drying conditions on agglomeration of melamine-formaldehyde microcapsules. *Drying Technology*, *34*(12), 1510–1520. <https://doi.org/10.1080/07373937.2015.1131713>
- Engineering Toolbox. (2003). *Air - dynamic and kinematic viscosity*. https://www.engineeringtoolbox.com/air-absolute-kinematic-viscosity-d_601.html
- Engineering Toolbox. (2004a). *Air - specific heat at constant pressure and varying temperature*. https://www.engineeringtoolbox.com/air-specific-heat-capacity-d_705.html
- Engineering Toolbox. (2004b). *Water - dynamic and kinematic viscosity*. https://www.engineeringtoolbox.com/water-dynamic-kinematic-viscosity-d_596.html
- Engineering Toolbox. (2009). *Air - thermal conductivity*. https://www.engineeringtoolbox.com/water-dynamic-kinematic-viscosity-d_596.html
- Finotello, G., Padding, J. T., Deen, N. G., Jongsma, A., Innings, F., & Kuipers, J. A. M. (2017). Effect of viscosity on droplet-droplet collisional interaction. *Physics of Fluids*, *29*(6), 067102. <https://doi.org/10.1063/1.4984081>
- Gordon, M., & Taylor, J. S. (1952). Ideal copolymers and the second-order transitions of synthetic rubbers. i. non-crystalline copolymers. *Journal of Applied Chemistry*, *2*(9), 493–500. <https://doi.org/10.1002/jctb.5010020901>
- Jakubczyk, D., Kolwas, M., Derkachov, G., Kolwas, K., & Zientara, M. (2012). Evaporation of microdroplets: The "radius-square-law" revisited. *Acta Physica Polonica-Series A General Physics*, *122*(4), 709. <https://doi.org/10.12693/aphyspola.122.709>
- Krishna, R., & Van Baten, J. M. (2005). The darken relation for multicomponent diffusion in liquid mixtures of linear alkanes: An investigation using molecular dynamics (md) simulations. *Industrial & engineering chemistry research*, *44*(17), 6939–6947. <https://doi.org/10.1021/ie050146c>
- Krishnan, K. G., & Loth, E. (2015). Effects of gas and droplet characteristics on drop-drop collision outcome regimes. *International Journal of Multiphase Flow*, *77*, 171–186. <https://doi.org/10.1016/j.ijmultiphaseflow.2015.08.003>
- Kudra, T. (2003). Sticky region in dryingdefinition and identification. *Drying Technology*, *21*(8), 1457–1469. <https://doi.org/10.1081/DRT-120024678>

- Law, C. K. (1982). Recent advances in droplet vaporization and combustion. *Progress in energy and combustion science*, 8(3), 171–201. [https://doi.org/10.1016/0360-1285\(82\)90011-9](https://doi.org/10.1016/0360-1285(82)90011-9)
- Lin, S. X. Q., & Chen, X. D. (2006). A model for drying of an aqueous lactose droplet using the reaction engineering approach. *Drying technology*, 24(11), 1329–1334. <https://doi.org/10.1080/07373930600951091>
- Maidannyk, V. A., & Roos, Y. H. (2017). Water sorption, glass transition and strength of lactose–whey protein systems. *Food Hydrocolloids*, 70, 76–87. <https://doi.org/10.1016/j.foodhyd.2017.03.025>
- Malafrente, L., Ahrné, L., Kaunisto, E., Innings, F., & Rasmuson, A. (2015). Estimation of the effective diffusion coefficient of water in skim milk during single-drop drying. *Journal of food engineering*, 147, 111–119. <https://doi.org/10.1016/j.jfoodeng.2014.09.032>
- McDonald, E. J., & Turcotte, A. L. (1948). Density and refractive indices of lactose solutions. *Journal of research of the National Bureau of Standards*, 41(63), e68. <https://doi.org/10.1093/jaoac/31.3.687>
- Meerdink, G. (1993). *Drying of liquid food droplets: Enzyme inactivation and multicomponent diffusion*. Wageningen University; Research. <https://doi.org/10.1080/07373939408960007>
- Mills, A. F. (1992). *Heat transfer*. CRC Press.
- Morison, K. R., & Mackay, F. M. (2001). Viscosity of lactose and whey protein solutions. *International Journal of Food Properties*, 4(3), 441–454.
- Murti, R. A., Paterson, A. T. H. J., Pearce, D., & Bronlund, J. E. (2010). The influence of particle velocity on the stickiness of milk powder. *International Dairy Journal*, 20(2), 121–127. <https://doi.org/10.1016/j.idairyj.2009.08.005>
- Neri, L., Pittia, P., Bertolo, G., Torreggiani, D., & Sacchetti, G. (2011). Influence of water activity and system mobility on peroxidase activity in maltodextrin solutions. *Food biophysics*, 6, 281–287. <https://doi.org/10.1007/s11483-011-9218-z>
- NIST. (2023). *Saturation (pressure)*. <https://www.nist.gov/system/files/documents/srd/%20NISTIR5078-Tab2.pdf>
- Palzer, S. (2005). The effect of glass transition on the desired and undesired agglomeration of amorphous food powders. *Chemical Engineering Science*, 60(14), 3959–3968. <https://doi.org/10.1016/j.ces.2005.02.015>
- Perdana, J., van der Sman, R. G. M., Fox, M. B., Boom, R. M., & Schutyser, M. A. I. (2014). Measuring and modelling of diffusivities in carbohydrate-rich matrices during thin film drying. *Journal of Food Engineering*, 122, 38–47. <https://doi.org/10.1016/j.jfoodeng.2013.08.033>
- Petersen, T. (2015). *Model stickiness in spray drying* (Ph.D. Thesis). Technical University of Denmark. Technical University of Denmark.
- Presili, L. (2020). *Predicting stickiness of drying droplets through numerical simulation* (Master's thesis). Delft University of Technology.
- Ranz, W. E., & Marshall, W. R. (1952). Evaporation from drops: li. chem. *Engng. Prog*, 48(173-180), 19.
- Sadek, C., Schuck, P., Fallourd, Y., Pradeau, N., Le Floch-Fouéré, C., & Jeantet, R. (2015). Drying of a single droplet to investigate processstructurefunction relationships: a review. *Dairy Science and Technology*, 95(6), 771–794.
- Schultz, S. G., & Solomon, A. K. (1961). Determination of the effective hydrodynamic radii of small molecules by viscometry. *The Journal of general physiology*, 44(6), 1189–1199. <https://doi.org/10.1085/jgp.44.6.1189>
- Sewalt, E. J. G., Winkenius, S., van Steijn, V., van Ommen, J. R., & Meesters, G. M. H. (2023). The influence of drying on the collision outcome of partially-dried droplets and particles using maltodextrin systems. *Not published*.
- Sewalt, E. J. G., Zhang, F., van Steijn, V., van Ommen, J. R., & Meesters, G. M. H. (2020). Static and dynamic stickiness tests to measure particle stickiness. *KONA Powder and Particle Journal*, 2021017. <https://doi.org/10.14356/kona.2021017>
- Siemons, I., Politiek, R. G. A., Boom, R. M., van der Sman, R. G. M., & Schutyser, M. A. I. (2020). Dextrose equivalence of maltodextrins determines particle morphology development during single sessile droplet drying. *Food Research International*, 131, 108988. <https://doi.org/10.1016/j.foodres.2020.108988>

- Spurlin, H. M., Martin, A. F., & Tennent, H. G. (1946). Characterization of cellulose derivatives by solution properties: Plasticizers as solvents. *Journal of Polymer Science*, 1(2), 63–74. <https://doi.org/10.1002/pol.1946.120010201>
- Van Der Sman, R. G. M., & Meinders, M. B. J. (2013). Moisture diffusivity in food materials. *Food chemistry*, 138(2-3), 1265–1274. <https://doi.org/10.1016/j.foodchem.2012.10.062>
- van der Hoeven, M. (2008, August 1). *Particle-droplet collisions in spray drying* (Ph.D. Thesis). School of Engineering, The University of Queensland.
- Vehring, R., Foss, W. R., & Lechuga-Ballesteros, D. (2007). Particle formation in spray drying. *Journal of Aerosol Science*, 38(7), 728–746. <https://doi.org/10.1016/j.jaerosci.2007.04.005>
- Verdurmen, R. E. M., Menn, P., Ritzert, J., Blei, S., Nhumaio, G. C. S., Sonne Sørensen, T., Gunging, M., Straatsma, J., Verschueren, M., Sibeijn, M., et al. (2004). Simulation of agglomeration in spray drying installations: The edecad project. *Drying technology*, 22(6), 1403–1461. <https://doi.org/10.1081/drt-120038735>
- Verheijen, R. (2021). *Predictive scale-up of a spray drying process using gproms* (Master's thesis). Delft University of Technology.
- Versypt, A. N. F., & Braatz, R. D. (2014). Analysis of finite difference discretization schemes for diffusion in spheres with variable diffusivity. *Computers & chemical engineering*, 71, 241–252. <https://doi.org/10.1016/j.compchemeng.2014.05.022>
- Vrentas, J. S., & Duda, J. L. (1977). Diffusion in polymersolvent systems. i. reexamination of the free-volume theory. *Journal of Polymer Science: Polymer Physics Edition*, 15(3), 403–416. <https://doi.org/10.1002/pol.1977.180150302>
- Walmsley, T. G., Walmsley, M. R. W., Atkins, M. J., Neale, J. R., & Sellers, C. M. (2014). An experimentally validated criterion for skim milk powder deposition on stainless steel surfaces. *Journal of food engineering*, 127, 111–119. <https://doi.org/10.1016/j.jfoodeng.2013.11.025>
- Williams, M. L., Landel, R. F., & Ferry, J. D. (1955). The temperature dependence of relaxation mechanisms in amorphous polymers and other glass-forming liquids. *Journal of the American Chemical Society*, 77(14), 3701–3707. <https://doi.org/10.1021/ja01619a008>
- Winkeniuss, S. (2021). *The influence of partial drying on the collision outcome of a droplet-particle collision* (MSc. Thesis). Delft University of Technology.

6

Conclusions and Outlook

6.1. Conclusion

This thesis sought to provide insight into the mechanisms of the collision behavior of partially-dried droplets in spray drying, with a focus on the food processing sector. Maltodextrin, a common excipient, provided a suitable material for this study due to its well-known properties, which were determined by our colleagues in the Food Process Engineering group in Wageningen. The aim of this thesis was to develop relations for sticking probabilities through experimental methods that could be implemented in macro-scale computational fluid dynamics (CFD) models, which are the current state of the art when it comes to simulating spray drying processes.

In Chapter 1, the challenges for the experimental assessment of collisions of rapidly drying droplets in spray drying were described. These key challenges included the chaotic nature of the turbulent airflow in the spray dryer, the high impact velocities and the multitude of the collisions between partially dried droplets, the small volume of the droplets, and the resulting extremely short drying times, and the non-homogeneous and rapidly changing droplet properties. This thesis addressed some of these challenges by developing experimental setups that allow well controlled droplet collisions in order to better understand the collision behavior of partially-dried maltodextrin droplets.

In Chapter 2, the fundamental question of what stickiness is and how it is measured was explored. It was generally concluded that stickiness is a surface-related phenomenon, primarily governed by immobile liquid bridging. The glass transition temperature was deemed a crucial parameter for any assessment of stickiness, as stickiness was found to occur at temperatures slightly above the glass transition temperature, though the exact temperature deviation was highly condition-dependent. It was noted that the contact dynamics could influence stickiness, with the contact time being a straightforward parameter to describe this. However, the influence of particle shape, contact area, material properties, and impact velocity all complicated this matter. In conclusion, the key findings of this chapter were that there is a lack of experimental methods to measure the stickiness of drying liquids, that droplet surface properties are instrumental to predicting stickiness and collision outcome, and that the dynamics of a collision are a non-negligible influence on the collision outcome for the conditions that collisions occur in during spray drying.

In Chapter 3, the problem of experimentally assessing the intra-droplet concentration gradient of an evaporating droplet was addressed (Schutyser et al., 2019). Optical coherence tomography was used to quantify the local mobility of TiO_2 agglomerates in an evaporating droplet. Using the known properties of maltodextrin, the local mobility was able to be used to calculate the local viscosity both spatially over the height of the droplet and temporally at a frequency of 1 Hz. This novel application of Optical coherence tomography illustrated that it was possible to measure intra-droplet concentration gradients at order-of-magnitude accuracy, which, due to the several order-of-magnitude increase of viscosity during drying, was sufficient to qualitatively show the formation of a concentrated skin layer. While promising for the validation of models predicting, the temporal resolution of this first demonstration did not approach the timescales of

evaporation that were found in spray drying, since, instead of minutes, the drying in spray drying occurs on second to sub-second timescales.

In Chapter 4, the locking point as a characteristic point in the drying process of a solute-containing droplet was assessed, since, experimental methods to determine the surface conditions of a drying droplet proved challenging. A particle ejector collision setup was developed that showed coalescence, sticking and bouncing collisions occurring in order of increasing drying time under mild conditions. However, it remained difficult to reasonably relate this locking point to the transitions between coalescence, sticking and bouncing collisions. Comparing the collision behavior with the theoretical rate of accumulation assuming steady-state evaporation allowed for the mapping of collision outcomes. The Péclet number, representing the ratio between surface concentration due to shrinking and homogenization of the concentration due to diffusion, determined for the conditions at $t = 0$, was used to achieve a good separation between the three collision outcomes coalescence, sticking and bouncing. This strongly suggested that the droplet's surface viscosity as a result of the drying conditions was indicative of the collision outcome.

In Chapter 5, a comparison between mild and industrial-like drying conditions was made. A collision setup with small and falling drying droplets was developed and used together with the particle ejector from Chapter 4 to test the collision behavior under both mild and industrial drying conditions. The hypothesis that was tested was whether the transition to the glassy state at the droplet surface, when numerically predicted, is a good indicator of the timing of the transitions between the three collision outcomes. If true, this would further support the common idea that stickiness is a surface phenomenon. The numerically predicted surface glassy state transition proved to be a good indicator for the collisions under mild drying conditions. However, the surface glassy state transition proved to be less useful for the industrial drying conditions. The droplets drying at industrial timescales began to bounce much later compared to the droplets drying at milder conditions. The work presented in this chapter strongly suggests that the intra-droplet concentration gradient should not be disregarded when predicting collision behavior, especially for industrial-like drying conditions. The dynamic conditions of the droplet lead to the conclusion that the surface conditions alone are insufficient when establishing a predictive relation for collision outcome.

6.2. Outlook

The challenge now is to elucidate how the intra-droplet concentration gradient affects the collision outcome and to develop a way to incorporate this gradient into predictive relations. The remainder of this chapter provides several recommendations for the continuation of the research presented in this thesis. Section 6.2.1, in line with the proposed scope of the consortium to which this project belongs, proposes the use of droplet collision simulations to expand upon the experimental collision outcomes. Section 6.2.2 and Section 6.2.3 provide recommendations for improving and validating the predictive approach using Péclet presented in this work. One of the goals of this work was to bring experimental evaporation conditions closer to the conditions observed in spray drying, which was done with the falling droplet column presented in Chapter 5. Section 6.2.4 and Section 6.2.5 provide two recommendations that could bring controlled collision experiments with partially dried droplets closer to the conditions that droplets experience in the spray drying process.

6.2.1. Fundamental analysis of the intra-droplet concentration gradient

Historically, experimental analysis of drying droplet behavior has been subjected to major challenges due to the complexity introduced by both evaporation and collision properties. Through careful development of collision setups and experiments, this thesis has been able to reveal much about how droplet properties, drying conditions and collision properties affect the outcome of collisions of partially-dried droplets. It also showed how a predictive approach using initial droplet conditions and an assumption of steady-state evaporation could reach good separation of collision outcomes for the mild drying conditions.

Besides continuing with building a broader dataset of collision outcomes for different drying rates, solutes, droplet sizes and collision conditions, we encourage the use of numerical methods to enrich the understanding provided by the here-presented experimental results. At the Process & Energy department at the Delft University of Technology, our colleagues are developing collision simulations using smoothed-particle

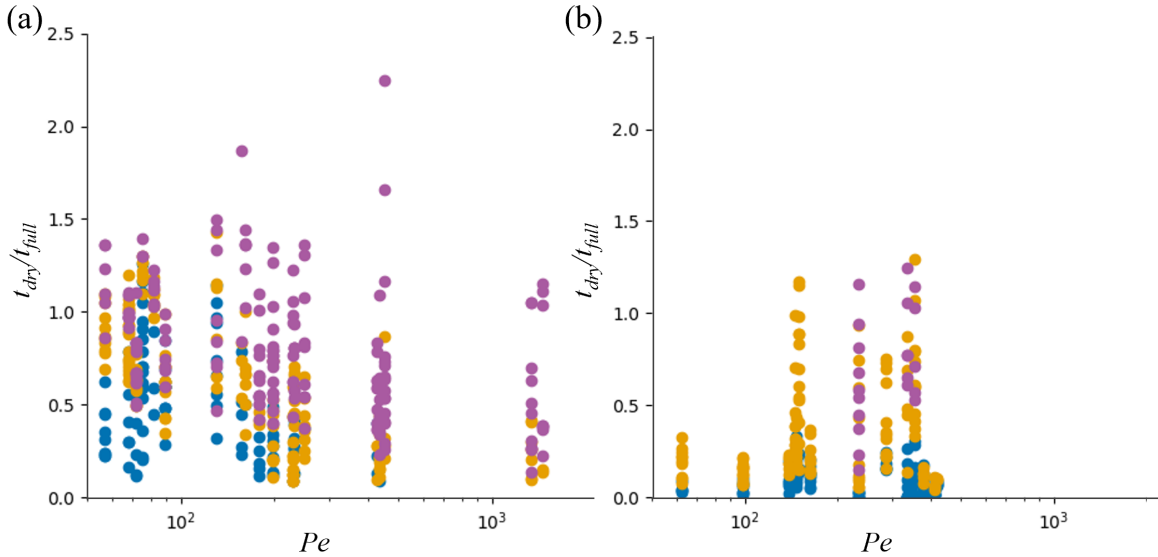


Figure 6.1: Collision outcomes in relation to the Péclet number and drying time normalize with t_{full} . a) Particle Ejector collisions, b) Falling Droplet Column collisions. Blue is coalescence, yellow is sticking and purple is bouncing.

hydrodynamics. This simulation has potential to precisely collide droplets with each other while also accounting for the visco-elastic properties of different maltodextrins. Such a numerical simulation could be essential enriching our understanding through isolation of specific variables that could serve challenging in experimental setups. These numerical methods do require input from experimental methods since they cannot determine all initial conditions first principles. The collision experiments as well as techniques that measure the intra-droplet concentration gradient, such as the optical coherency tomography presented in Chapter 3, are also crucial for their validation.

The analysis presented in Chapter 4 and Chapter 5 has revealed that the intra-droplet concentration gradient plays an integral role in the outcome of a collision with a partially-dried droplet. To further understand the impact of the intra-droplet concentration gradient on the collision outcome, simulating collisions between two droplets while varying the intra-droplet concentration gradient per collision could provide valuable insights in how the steepness of the intra-droplet concentration gradient affects the collision outcome. This can be done by maintaining a constant concentration at the center and surface of the droplet while imposing the steepness of the gradient. We hypothesize based on the work in Chapter 5 that a steeper gradient would make coalescence more likely over stickiness and stickiness more likely over bouncing.

6.2.2. Exploring the universality of an alternative mapping approach to include collision dynamics

An estimation of the Péclet number was found to be useful for the particle ejector, however when applied to the falling droplet column the range of Péclet numbers for which evaporation times greater than t_{full} were reached was much more narrow, as shown in Figure 6.1. Hence, it was challenging to determine whether the separation that was found for the particle ejector, where coalescence occurred predominantly at low Pe and low t_{dry}/t_{full} , also applied to the falling droplet column. The occurrence of coalescence at high Pe and the occurrence of sticking at low Pe and low t_{dry}/t_{full} suggests that the collision outcomes cannot be separated based on the Péclet number alone.

An analysis of the particle ejector results showed that the impact velocity had minimal effect on the collision outcomes. An order of magnitude analysis showed that the influence of impact velocity is expected to be of similar magnitude for the falling droplet column collisions. Hence, it was found to be more interesting to explore the influence of the intra-droplet concentration gradient in Chapter 5. Here, we revisit the

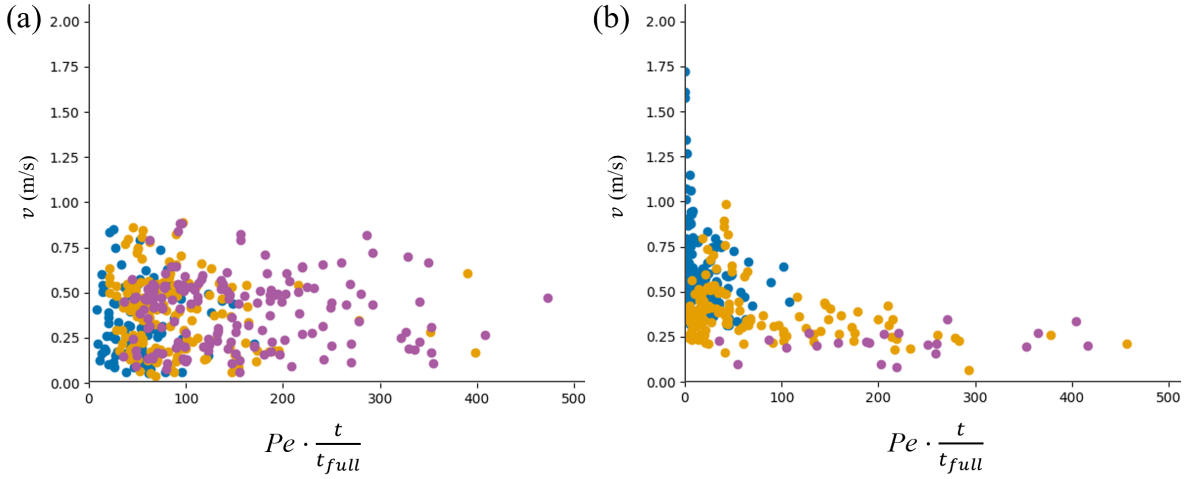


Figure 6.2: Collision outcomes in relation to the $Pe \cdot \frac{t}{t_{full}}$ number and the impact velocity. a) Particle Ejector collisions, b) Falling Droplet Column collisions. Blue is coalescence, yellow is sticking and purple is bouncing.

influence of the impact velocity and its importance. Instead of mapping the collision outcomes based on drying time and Pe , the axes are redefined to impact velocity v on the y-axis and the state of the droplet on the x-axis. The state of the droplet is proposed as $Pe \cdot \frac{t}{t_{full}}$, which, conceptually, is the normalized time in which a droplet dries at steady-state conditions based on the initial drying environment. The results of redefining the axes of the map is shown in Figure 6.2.

This figure shows that the impact velocity indeed has minimal effect on the collision outcomes for the particle ejector data. The collision outcome seems a consequence of the degree of drying. Although there is quite some overlap between the outcomes, the trend of coalescence, sticking to bouncing with increasing dryness is clear. The falling droplet column results in Figure 6.2b show a remarkable separation of collision outcomes. Coalescence occurs at high v and low $Pe \cdot \frac{t}{t_{full}}$, sticking occurs over the entire range of drying and bouncing occurs over a large range of drying, although at least at $Pe \cdot \frac{t}{t_{full}} > 50$. The most notable observation is that bouncing occurs solely at low values or v .

This alternative mapping approach shows promise for separating collision outcome regimes while also including the impact velocity. Further work exploring the universality of this approach would be interesting since the parameter space for v presented here is somewhat limited, especially at higher dryness, due to the falling velocity strongly decreasing with the loss of mass due to evaporation.

6.2.3. Exploring the limitations of the Péclet number

Outside of the impact velocity, there are two limitations of the Péclet approach that could result in inaccurate predictions when assuming the steady state evaporation, i.e. a constant rate of evaporation when considering the units $m^2 s^{-1}$, is a good representation model of the drying droplet. The first limitation is that the Péclet approach does not account for the initial phase of evaporation where the droplet evaporation has not yet reached steady state. The temperature of the droplet is still changing, meaning the steady state Péclet will not accurately capture this initial phase. A second limitation is that the Péclet approach does not account for changes as a result of transitioning from the constant rate drying regime to the falling rate drying regime or the morphology change regime thereafter. Evaporation rate decreases due to the transition from external limitation to internal diffusive limitation, which is not accounted for in the Péclet approach. A predictive strategy whereby collision maps are made using the Péclet number and impact velocity of the collision could look like a promising approach for resolving collision outcomes in CFD model. Further research is needed to determine the extent to which the predictive strategy described above is limited by the two constraints identified. This would allow for a clearer understanding of the boundaries within which accurate predictions can be made using this approach, or alternatively, provide a more accurate assessment of the level of inaccuracy associated with this method.

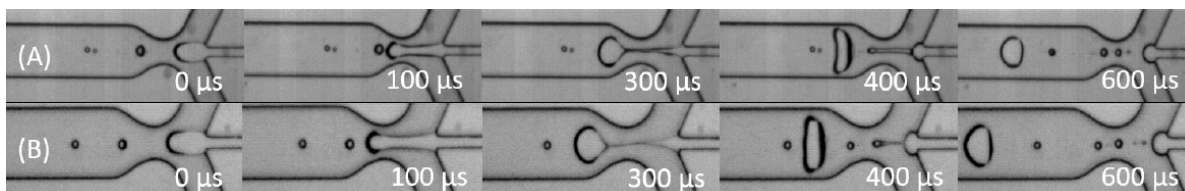


Figure 6.3: Images of the droplet formation at $We_{gas} \approx 4.814$ and $We_{liquid} \approx 7.33 \times 10^{-4}$. The devices are baked at 200 °C for 2 hours after bonding and hung up vertically. (A) PDMS-PDMS. (B) PDMS-Glass. The white numbers indicate the time in seconds. (Drewes, 2018)

6.2.4. Temperature and humidity ramping for mimicking spray drying

To simplify the experiment and focus solely on assessing stickiness, the temperature and humidity of the drying medium were kept constant. However, it should be noted that these constant conditions do not accurately reflect the dynamic conditions experienced by droplets in spray drying. During spray drying, droplets are subjected to varying temperature and humidity levels due to evaporative cooling and evaporation, respectively. This presents a challenge for any predictive approach that relies on a steady-state approximation of droplet drying. The predictive approach proposed in this thesis uses the initial environment conditions to determine a driving force for evaporation. These initial environmental conditions remain steady throughout the experiments while the intra-droplet conditions are dynamic. In spray drying, both environmental and intra-droplet conditions are dynamic. Since the drying conditions in the spray are substantially different from the ingoing air properties, it remains a question whether the steady-state estimation for collision outcome holds up and what temperature and humidity should be used. To determine the influence of the dynamic environmental conditions on droplet evaporation, an approach could be to use a sessile single droplet setup where the gas flow that is used to dry the droplet changes in both temperature and humidity during evaporation. In this way, the temperature and humidity can be ramped to better mimick the spray drying conditions. As shown in Chapter 4, a sessile single droplet drying setup can be combined with a particle ejector device to also test collision outcomes.

6.2.5. Miniaturizing collision experiments with microfluidic approaches

Microfluidics has revolutionized droplet generation techniques and miniaturization. The ability to control the flow of fluids in microchannels has led to the development of numerous droplet generation techniques such as flow-focusing, T-junction, and co-flowing (Anna et al., 2003). These techniques have been used to generate droplets of controlled size, composition, and morphology for a wide range of applications including drug delivery, biochemical analysis, and emulsion synthesis. Furthermore, microfluidic droplet generation has enabled liquid-in-gas droplet generation, which was previously difficult to achieve using conventional methods. Recently, the possibility of generating sub-millimeter droplets of various liquids in gas using a microfluidic device was demonstrated (Tirandazi & Hidrovo, 2017). Consequently, this technology is promising for allowing better similarity to spray drying conditions where the evaporation rates of droplets are in the sub-second range. We have built these liquid-in-gas devices using polydimethylsiloxane (PDMS) elastomer for the chip and were able to operate these devices in the dripping regime. Two examples with different materials are shown in Figure 6.3. The diameter of water droplets generated was $113.6 \pm 1.2 \mu\text{m}$ for PDMS-PDMS and $130.7 \pm 1.6 \mu\text{m}$ for PDMS-Glass devices. When maltodextrin was introduced into the liquid phase. The device suffered from both the material drying and sticking to the walls of the device, which disturbed the droplet generation, and drying of the liquid-phase nozzle resulting in it becoming blocked. We have identified two promising approaches in our preliminary work that could prevent the disruption of the device. A first approach is to disconnect the droplet from the channel walls after generation at the junction. The generated droplets are ejected out of the device, immediately after generation. While this prevent material sticking to the channel wall, it also decreases the control of the droplet trajectory. A second approach is fine-tuning the properties of the channel walls. Our work has shown that both increasing the hydrophobicity and decreasing the contact angle hysteresis of a PDMS surface decreases the sticking of aqueous solution to the surface. Introducing roughness on the PDMS surface showed to be particularly effective. The application of roughness in the PDMS chip, however,

resulted in leakage of the chip at the operating pressures required for liquid-in-gas droplet generation. This was caused by the roughness also reducing the binding strength between the two PDMS layers of the chip (Eschauzier, 2020). Unfortunately, due to limited lab access in 2020 and different priorities in the scope of this thesis, this work was not continued. Nonetheless, the preliminary work in this thesis suggests that microfluidic liquid-in-gas droplet generators are promising for generating micron-sized droplets and that they could be used in performing controlled collision experiments with drying times similar to spray drying.

Bibliography

- Anna, S. L., Bontoux, N., & Stone, H. A. (2003). Formation of dispersions using flow focusing in microchannels. *Applied physics letters*, *82*(3), 364–366.
- Drewes, G. (2018). *Liquid-in-gas microfluidics for the generation of monodisperse micro-droplets* (Bachelor's Thesis). Delft University of Technology.
- Eschauzier, V. L. (2020). *Drying of solute-containing micro-droplets using a lab-on-a-chip approach* (Master's thesis). Delft University of Technology.
- Schutyser, M. A. I., Both, E. M., Siemons, I., Vaessen, E. M. J., & Zhang, L. (2019). Gaining insight on spray drying behavior of foods via single droplet drying analyses. *Drying Technology*, *37*(5), 525–534.
- Tirandazi, P., & Hidrovo, C. H. (2017). Liquid-in-gas droplet microfluidics; experimental characterization of droplet morphology, generation frequency, and monodispersity in a flow-focusing microfluidic device. *Journal of Micromechanics and Microengineering*, *27*(7), 075020. <https://doi.org/10.1088/1361-6439/aa7595>

List of publications

Papers

Luo, Q., Sewalt, E., Borst, J. W., Westphal, A. H., Boom, R. M., & Janssen, A. E. M. (2019). Analysis and modeling of enhanced green fluorescent protein diffusivity in whey protein gels. *Food Research International*, *120*, 449–455. <https://doi.org/10.1016/j.foodres.2018.10.087>

Sewalt, E. J. G., Zhang, F., van Steijn, V., van Ommen, J. R., & Meesters, G. M. H. (2020). Static and dynamic stickiness tests to measure particle stickiness. *KONA Powder and Particle Journal*, 2021017. <https://doi.org/10.14356/kona.2021017>

Sewalt, E. J. G., Kalkman, J., van Ommen, J. R., Meesters, G. M. H., & van Steijn, V. (2022). Revealing how maltodextrin-containing droplets dry using optical coherence tomography. *Food Research International*, *157*, 111049. <https://doi.org/10.1016/j.foodres.2022.111049>

Curriculum Vitae

Erik Sewalt was born on July 19, 1993, in Doetinchem, the Netherlands. He completed his Gymnasium studies at the Almende College in Silvolde, the Netherlands, in 2011. Following this, Erik pursued a Bachelor's in Molecular Life Sciences at Wageningen University and Research, beginning in 2011, and transitioned to a Bachelor's in Food Technology, graduating in 2015. He continued his academic journey with a Master's in Food Technology at Wageningen University and Research, in Wageningen, The Netherlands, specializing in sustainable processing technology. His Master's thesis focused on analyzing and modeling protein diffusivity in protein gels, specifically exploring pepsin migration within protein-rich food matrices. During his Master's, Erik completed an internship at UC Davis Department of Biological & Agricultural Engineering in Davis, USA, developing in vitro methods for classifying protein-rich food products during simulated gastric digestion, culminating in his graduation in 2017.

In October 2017, Erik joined TU Delft's Department of Chemical Engineering as a PhD student in the Product and Process Engineering Group. His doctoral research centered on investigating the collision behavior of evaporating solute-containing droplets in spray drying conditions, with the goal of developing predictive approaches for collision outcomes during drying. His supervisors were Prof. dr. ir. J. Ruud van Ommen (promotor), Dr. ir. Volkert van Steijn (promotor), and Dr. ir. Gabrie M.H. Meesters (copromotor). Since October 2021, Erik has been employed as a grant consultant at Plus Projects in The Hague, The Netherlands.